



Ministério da
Ciência e Tecnologia



INPE-15684-TDI/1458

**ELECTRIC AND MAGNETIC FIELD SIGNATURES OF
GRAVITY WAVES AND 2-DAY PLANETARY WAVES
IN THE EQUATORIAL E-REGION**

Henrique Carlotto Aveiro

Dissertação de Mestrado do Curso de Pós-Graduação em Geofísica Espacial,
orientada pelos Drs. Clezio Marcos De Nardin e Mangalathayil Ali Abdu, aprovada
em 19 de fevereiro de 2009

Registro do documento original:

<<http://urlib.net/sid.inpe.br/mtc-m18@80/2008/12.16.11.31>>

INPE
São José dos Campos
2009

PUBLICADO POR:

Instituto Nacional de Pesquisas Espaciais - INPE

Gabinete do Diretor (GB)

Serviço de Informação e Documentação (SID)

Caixa Postal 515 - CEP 12.245-970

São José dos Campos - SP - Brasil

Tel.:(012) 3945-6911/6923

Fax: (012) 3945-6919

E-mail: pubtc@sid.inpe.br

CONSELHO DE EDITORAÇÃO:

Presidente:

Dr. Gerald Jean Francis Banon - Coordenação Observação da Terra (OBT)

Membros:

Dr^a Maria do Carmo de Andrade Nono - Conselho de Pós-Graduação

Dr. Haroldo Fraga de Campos Velho - Centro de Tecnologias Especiais (CTE)

Dr^a Inez Staciarini Batista - Coordenação Ciências Espaciais e Atmosféricas (CEA)

Marciana Leite Ribeiro - Serviço de Informação e Documentação (SID)

Dr. Ralf Gielow - Centro de Previsão de Tempo e Estudos Climáticos (CPT)

Dr. Wilson Yamaguti - Coordenação Engenharia e Tecnologia Espacial (ETE)

BIBLIOTECA DIGITAL:

Dr. Gerald Jean Francis Banon - Coordenação de Observação da Terra (OBT)

Marciana Leite Ribeiro - Serviço de Informação e Documentação (SID)

Jefferson Andrade Ancelmo - Serviço de Informação e Documentação (SID)

Simone A. Del-Ducca Barbedo - Serviço de Informação e Documentação (SID)

REVISÃO E NORMALIZAÇÃO DOCUMENTÁRIA:

Marciana Leite Ribeiro - Serviço de Informação e Documentação (SID)

Marilúcia Santos Melo Cid - Serviço de Informação e Documentação (SID)

Yolanda Ribeiro da Silva Souza - Serviço de Informação e Documentação (SID)

EDITORAÇÃO ELETRÔNICA:

Viveca Sant´Ana Lemos - Serviço de Informação e Documentação (SID)



Ministério da
Ciência e Tecnologia



INPE-15684-TDI/1458

**ELECTRIC AND MAGNETIC FIELD SIGNATURES OF
GRAVITY WAVES AND 2-DAY PLANETARY WAVES
IN THE EQUATORIAL E-REGION**

Henrique Carlotto Aveiro

Dissertação de Mestrado do Curso de Pós-Graduação em Geofísica Espacial,
orientada pelos Drs. Clezio Marcos De Nardin e Mangalathayil Ali Abdu, aprovada
em 19 de fevereiro de 2009

Registro do documento original:

<<http://urlib.net/sid.inpe.br/mtc-m18@80/2008/12.16.11.31>>

INPE
São José dos Campos
2009

Dados Internacionais de Catalogação na Publicação (CIP)

A32e Aveiro, Henrique Carlotto.
Electric and magnetic field signatures of gravity waves and 2-day planetary waves in the equatorial e-region / Henrique Carlotto Aveiro. – São José dos Campos : INPE, 2009.
141p. ; (INPE-15684-TDI/1458)

Dissertação (Mestrado em Geofísica Espacial) – Instituto Nacional de Pesquisas Espaciais, São José dos Campos, 2009.

Orientadores : Drs. Clezio Marcos De Nardin e Mangalathayil Ali Abdu .

1. Ionosfera. 2. Aeronomia. 3. Radar coerente. 4. Ondas atmosféricas. 5. Campos elétricos atmosféricos. I.Título.

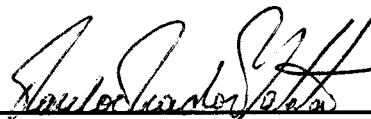
CDU 551.510.535

Copyright © 2009 do MCT/INPE. Nenhuma parte desta publicação pode ser reproduzida, armazenada em um sistema de recuperação, ou transmitida sob qualquer forma ou por qualquer meio, eletrônico, mecânico, fotográfico, reprográfico, de microfilmagem ou outros, sem a permissão escrita do INPE, com exceção de qualquer material fornecido especificamente com o propósito de ser entrado e executado num sistema computacional, para o uso exclusivo do leitor da obra.

Copyright © 2009 by MCT/INPE. No part of this publication may be reproduced, stored in a retrieval system, or transmitted in any form or by any means, electronic, mechanical, photocopying, recording, microfilming, or otherwise, without written permission from INPE, with the exception of any material supplied specifically for the purpose of being entered and executed on a computer system, for exclusive use of the reader of the work.

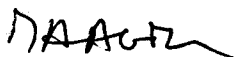
**Aprovado (a) pela Banca Examinadora
em cumprimento ao requisito exigido para
obtenção do Título de Mestre em
Geofísica Espacial**

Dr. Paulo Prado Batista



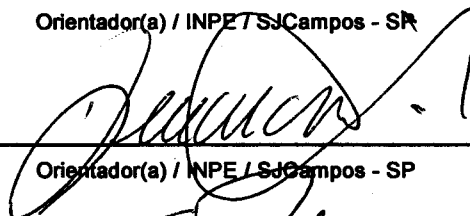
Presidente / INPE / SJCampos - SP

Dr. Mangalathayil Ali Abdu



Orientador(a) / INPE / SJCampos - SP

Dr. Clezio Marcos De Nardin



Orientador(a) / INPE / SJCampos - SP

Dr. Severino Luiz Guimarães Dutra



Membro da Banca / INPE / SJCampos - SP

Dr. Amauri Fragoso de Medeiros



Convidado(a) / UFCG / Campina Grande - PB

Aluno (a): Henrique Carlotto Aveiro

São José dos Campos, 19 de fevereiro de 2009

- 1 - Keep the discipline.*
- 2 - Don't enervate.*
- 3 - Don't sadden.*
- 4 - Don't have hostile feelings.*
- 5 - Be understanding.*
- 6 - Be calm.*
- 7 - Be peaceful.*
- 8 - Keep the ethics.*
- 9 - Make friendship with everyone.*
- 10 - Respect God and people.*
- 11 - Be modest.*
- 12 - Be right and honest.*
- 13 - Become aware that Aikido represents one of the God's way.*
- 14 - Become aware that Aikido practicing has as a principle the self-knowledge.*

AIKIDO SLOGANS

*To my parents
José Telmo Carvalho Aveiro and
Cludete Carlotta Aveiro*

ACKNOWLEDGEMENTS

I wish to thank my committee members – Clezio De Nardin, Mangalathayil Abdu, Amauri Medeiros, Paulo Prado Batista, and Severino Dutra – for their patience, enthusiasm, encouragement, and careful review of my work. Clezio in particular has been a great inspiration, and friend, for his continuous support and guidance throughout my undergraduate and graduate period. He has encouraged me to be active and to pursue diverse interests, yet has also pushed me to be independent, giving me a somewhat unique graduate experience. Moreover, I thank Prof. Abdu for being my second tutor and for giving me helpful advices concerning the ionospheric physics background of my work.

To another very important person in my life, Dr. Nelson Schuch, for all the psychological guidance he gave me when I was undergraduate student. If I have any quality related to emotional intelligence and leadership, he was the person that taught me. All my gratitude for his help and attention.

I owe a special thanks to certain colleagues and friends who have either been extremely helpful in my educational process or have given me something to do outside of work. These people include Ângela, Dani, Ênia, Fernanda, Laís, Laysa, Márcio, Paulo, and Pedro. A special thanks to Delx, Fábio, and Marlos, for the time I lived in their living room, and to Vânia and Marcelo for sharing a house and life in São José dos Campos with me. Best wishes to you all.

My great appreciation goes to the Onogoro Dojo for excellent camaraderie and many memorable experiences. The time I was practicing Aikido with them was one of the best in my life. This martial art helped me to keep a body and mental health during my graduate studies.

Also, I thank the financial support of this work through a Master's fellowship from Conselho Nacional de Desenvolvimento Científico e Tecnológico .

Last but not least, I would like to thank my parents, José Telmo Carvalho Aveiro and Cleudete Carlotto Aveiro, and my sister, Juliana Carlotto Aveiro, for being continual, albeit distant, supporters. Thanks a lot!

ABSTRACT

Equatorial electrojet (EEJ) observations using VHF radars show backscattered echoes from two types of electron density irregularities explained by the modified two-stream (Type I) and the gradient drift (Type II) instabilities. From the Type II irregularity velocities obtained by radar data we have inferred the vertical electric fields (E_z). The harmonic analysis of such fields shows the presence of gravity waves-induced electric fields in the EEJ. We calculated the ratio between GW-related electric fields and the total E_z . This factor is an indicator of the efficiency in the production of an additional electric field due to a gravity wave neutral wind. Also, we analyze the effects of the 2-day wave activity in the EEJ using one coherent radar and eight magnetometer stations located close to the dip equator. The wavelet analysis of the magnetometer data reveals a 2-day signature in the semidiurnal geomagnetic tide. The E-region zonal background ionospheric electric field derived from coherent radar measurements shows 2-day oscillations in agreement with such oscillations in the magnetometer data set. An anticorrelation between the tidal periodicities (diurnal, and semidiurnal) and the 2-day signature is also shown in the electric fields. The results are compared with simultaneous observations of 2-day planetary wave in meridional winds and ionosondes available in the literature. Our results are discussed based on the analysis of the magnetic activity.

ASSINATURAS NOS CAMPOS ELÉTRICOS E MAGNÉTICOS ÀS ONDAS DE GRAVIDADE E ONDAS PLANETÁRIAS DE 2-DIAS NA REGIÃO E EQUATORIAL

RESUMO

Observações do eletrojato equatorial (EEJ) utilizando radares VHF mostram ecos retro-espalhados em dois tipos de irregularidades de densidade eletrônica, explicadas pelas instabilidades de dois-feixes modificada (ecos Tipo I) e deriva de gradiente (ecos Tipo II). Das velocidades das irregularidades Tipo II obtidas de dados de radar, inferimos os campos elétricos verticais (E_z). A análise harmônica de tais campos mostra a presença de campos elétricos induzidos por ondas de gravidade (GW) no EEJ. Calculamos a razão entre os campos elétricos relacionados a GW e o campo elétrico vertical total. Este fator é um indicador da eficiência na produção de um campo elétrico causado por um vento neutro devido a uma onda de gravidade. Também, analisamos os efeitos da atividade da onda planetária de 2 dias no EEJ utilizando um radar coerente e oito magnetômetros instalados próximos ao equador magnético. A análise de *wavelets* dos dados de magnetômetros revela uma assinatura de 2 dias na maré semidiurna geomagnética. O campo elétrico ionosférico zonal da região E, derivado de medidas de radar coerente, mostra oscilações de 2 dias, em acordo com tais observações nos dados de magnetômetros. Uma anti-correlação entre as periodicidades de marés (diurna e semi-diurna) e a assinatura de dois dias é também mostrada nos campos elétricos. Os resultados são comparados com observações simultâneas de ondas planetárias de dois dias nos ventos meridionais e ionossondas disponíveis na literatura. Finalmente, nossos resultados são discutidos com base na análise da atividade magnética do período.

CONTENTS

Pág.

LIST OF FIGURES

LIST OF TABLES

LIST OF ABBREVIATIONS

LIST OF SYMBOLS

1 INTRODUCTION	29
1.1 The Ionosphere	29
1.1.1 D-region	29
1.1.2 E-region	29
1.1.3 F-region	31
1.2 Ionospheric Conductivity	31
1.3 Ionospheric E-region Dynamo	32
1.4 Equatorial Electrojet	35
1.5 Equatorial Electrojet Plasma Irregularities	36
1.5.1 Modified Two-Stream Instability and Type I echoes	36
1.5.2 Gradient-Drift Instability and Type II echoes	38
1.5.3 Neutral Winds and Phase Velocities of EEJ instabilities	39
2 GRAVITY WAVES AND PLANETARY WAVES	43
2.1 Gravity Waves	43
2.1.1 Electric Field Fluctuations in the EEJ due to Gravity Waves I - Observations	43
2.1.2 Electric Field Fluctuations in the EEJ due to Gravity Waves II - Theoretical Studies	45
2.2 Planetary Waves	47
2.2.1 Signatures of Planetary Waves in the Low-Latitude Ionosphere	49
3 INSTRUMENTATION AND DATA	57
3.1 50 MHz Coherent Backscatter Radar - RESCO	57
3.1.1 System Description	57

3.1.1.1	Antenna Array	57
3.1.1.2	Transmitter System	58
3.1.1.3	Receiver System	60
3.1.1.4	Signal Control and Data Storage System	61
3.1.2	Radar Data Processing	61
3.1.2.1	Example of RESCO Data Processing	64
3.2	Geomagnetic Components and Magnetometer	65
3.2.1	Measuring Ionospheric Current Signatures at Ground	66
3.3	Magnetic Activity Indices	68
3.3.1	Kp Index	69
3.3.2	Dst Index	69
3.3.3	Auroral Indices	70
3.4	Spectral Analysis Techniques	71
3.4.1	Continuous Wavelet Transform and the Morlet Wavelet-Mother	71
3.4.2	Lomb-Scargle Periodogram	73
4	CLIMATOLOGY OF GRAVITY WAVES-INDUCED ELECTRIC FIELDS	75
4.1	Experimental Description	75
4.2	Efficiency of GW-Induced Electric Fields	77
4.3	Period Trends	80
4.4	Observed Horizontal Phase Velocities	85
4.5	Discussions	85
4.5.1	Data Reliability	85
4.5.2	Comparison with Airglow Measurements	87
4.5.3	Overall Features and Implications	88
4.6	Conclusions	89
5	SIGNATURES OF 2-DAY WAVE IN THE E-REGION ELECTRIC FIELDS AND THEIR RELATIONSHIP TO WINDS AND IONOSPHERIC CURRENTS	91
5.1	Two-Day Wave in the E-Region Electric Fields	91
5.1.1	Radar Experimental Description	91
5.1.2	Results	92
5.2	Two-Day Signature in the EEJ currents	92
5.2.1	Magnetometer Data	92

5.2.2	Results	95
5.3	Previous Reports of 2-Day Waves Observations in January-February 2003	97
5.4	Discussions	100
5.5	Conclusions	103
6	CONCLUSIONS AND FUTURE WORKS	105
	REFERENCES	107
A	APPENDIX A - PRINCIPLES OF COHERENT BACKSCATTER RADARS	115
A.1	Radar Parameters	115
A.1.1	Radar Frequency	115
A.1.2	Pulse Width and Height Resolution	115
A.1.3	Pulse Repetition Frequency and Range	116
A.2	Coherent Detection and Doppler Effect	117
B	APPENDIX B - CODES FOR WAVELET ANALISYS OF MAGNETOMETER DATA (FOR WDC FOR GEOMAGNETISM - KYOTO DATA)	121
C	APPENDIX C - CODES FOR WAVELET ANALYSIS OF MAGNETIC INDICES	131

LIST OF FIGURES

	<u>Pág.</u>
1.1 Definition of the ionospheric layers based on the vertical distribution of electron density.	30
1.2 Altitude profiles of the direct conductivity, σ_0 , and the Hall and Pedersen conductivities, respectively, σ_2 and σ_1 . Red curves denote daytime values. Black curves denote nighttime values.	33
1.3 Coordinate system related to the conductivity tensor showing the electric and geomagnetic fields, and the inclination I	34
1.4 Scheme of ionospheric currents and electric fields based on the Ionospheric Dynamo Theory.	35
1.5 Examples of Type I (top) and Type II (bottom) irregularities spectra obtained by coherent radars.	37
1.6 Simplified representation of the gradient drift instability mechanism in the diurnal equatorial electrojet.	39
2.1 Time variations of Type II irregularity velocities of the backscatter radar signals on (a) a magnetically quiet day, (b) and (c) on moderately disturbed days and (d) on a magnetic storm day.	44
2.2 Variation of the average vertical electric field between 8 and 9 hours LT inferred from RESCO radar data during equinoctial period using 30° east beam (blue circles) and 30° west beam (red circles).	45
2.3 Eastward current density modulated by gravity waves (solid line) and without their action (dashed line). The left curve corresponds to $\lambda_z=20$ km and the right one to $\lambda_z=10$ km.	46
2.4 Efficiency factor R versus λ_z for $\lambda_h=50$ km. The solid line represents the case where vertical scale height H_z is null and dashed line to $H_z=-k_z$, where k_z is the vertical wavenumber.	48
2.5 Efficiency factor R versus λ_h . The solid line group represents the case where vertical scale height H_z is null and dashed line to $H_z=-k_z$. The four curves in each group are for the cases of $\lambda_z=5, 10, 15,$ and 20 km (from bottom to top in the diagram).	49
2.6 Geopotential and wind structure of an equatorial Kelvin wave (upper panel) and mixed Rossby-gravity wave (lower panel).	51

2.7	Power Spectral Density as a function of period for ΔH for the interval January 1 to March 26 (upper panel), and August 15 to November 8 (bottom panel), in 1979.	53
2.8	Wavelet analysis of (top) ionospheric foF2, (middle) h'F observed at Fortaleza, and (bottom) mesospheric zonal wind at 90 km observed at Cariri during the period from January 1 to April 30, 2005.	54
2.9	Schematic illustrating possible mechanisms for inducing planetary wave oscillations in the mesosphere/lower thermosphere (MLT) and dynamo regions.	55
3.1	RESCO antenna array in the São Luís Space Observatory.	58
3.2	East-west section of the RESCO antenna radiation pattern (32 strings of half wavelength dipoles) for the three operational modes: 30° west (upper panel), zenith (middle panel), and 30° east angle (bottom panel).	59
3.3	Schematic diagram representing the eight transmitters with the power splitters and the phase-shifters of the RESCO radar system.	60
3.4	Schematic diagram representing the duplexers, phase-shifters and power combiners of the RESCO radar system.	61
3.5	In-phase and quadrature components, and the respective power spectral density. The data set corresponds to 102.60 km height at 16h01 LT in February 15, 2002 obtained by the RESCO radar westward beam.	63
3.6	Simulated power spectrum (black) and the fitted Gaussian curves (blue).	64
3.7	Components of the geomagnetic field measurements for a sample Northern Hemisphere total field vector \mathbf{F} inclined into the Earth. An explanation of the letters and symbols is given in the text.	66
3.8	Flowchart of the program that calculates the Space-Scale Energy Density using the Morlet Wavelet-Mother from magnetometer data.	68
3.9	Kp index for October 2003.	69
3.10	Dst index for May 2005.	70
3.11	Auroral indices for October 2003.	72
4.1	Height median of the vertical electric field, filtered field, filtered wave amplitude, and efficiency factor for February 6, 2001.	79
4.2	Statistics of occurrences of E_z amplitude as function of time for (upper panel) solstice D months, (middle panel) equinoctial E months, and (lower panel) solstice J months. The continuous line represents the average vertical electric field for each 30-min interval and the vertical line is the standard deviation of E_z	81

4.3	Statistics of occurrences of the $E_{z(GW)}$ Amplitude as function of time for (upper panel) solstice D months, (middle panel) equinoctial E months, and (lower panel) solstice J months. The continuous line represents the average disturbed electric field for each 30-min interval and the vertical line is the standard deviation of $E_{z(GW)}$	82
4.4	Statistics of occurrences of the R_{GW} as function of time for (upper panel) solstice D months, (middle panel) equinoctial E months, and (lower panel) solstice J months. The continuous line represents the average factor for each 30-min interval and the vertical line is the standard deviation of R_{GW}	83
4.5	Histogram of the observed period binned in 2-minute intervals for (a) D, (b) E, and (c) J seasons.	84
4.6	Histogram of the observed horizontal wind velocity binned in 10 m/s intervals for (upper panel) D, (middle panel) E, and (lower panel) J seasons.	86
5.1	Lomb-Scargle periodogram calculated to the zonal electric field for (a) 20-24 January, (b) 27-31 January, (c) 17-21 February, and (d) 24-28 February, in 2003. The horizontal (dash dot) line indicates the level of 99% of confidence ($=9.90 \text{ mV}^2/\text{m}^2$).	93
5.2	Magnetometer stations locations.	94
5.3	H-component variation with respect to the midnight base level (dH) for HUA station during Jan-Feb 2003.	95
5.4	Space-scale energy density in log-scale of dH in January-February 2003 for the eight magnetic stations (from top to bottom): ASC, SLZ, HUA, TIR, PND, BNG, GUA, and AAE.	96
5.5	Space-scale energy density in log-scale of the amplitude of the diurnal tide (0.90-1.15 days) in January-February 2003 for the eight magnetic stations (from top to bottom): ASC, SLZ, HUA, TIR, PND, BNG, GUA, and AAE.	98
5.6	Space-scale energy density in log-scale of the amplitude of the semidiurnal tide (0.40-0.60 days) in January-February 2003 for the eight magnetic stations (from top to bottom): ASC, SLZ, HUA, TIR, PND, BNG, GUA, and AAE.	99
5.7	Dst and AE indices for January-February 2003.	102
5.8	Space-scale energy density of the Dst and AE indices for January-February 2003.	102

A.1	Sketch describing the radar backscatter from field-aligned plasma density irregularities (for a monostatic system), k_i and k_s denote the incident and scattered radar wave-vector, $\delta = 90 \pm \alpha$, where α is the aspect angle. λ_{irr} is the scale size of the irregularities.	116
A.2	Train of transmitted and received pulses.	117
A.3	Illustrating range ambiguity.	118
A.4	Coherent detector.	119
B.1	Flowchart of the program that calculates the Space-Scale Energy Density using the Morlet Wavelet-Mother from magnetometer data.	121
C.1	Flowchart of the program that calculates the Space-Scale Energy Density using the Morlet Wavelet-Mother from Magnetic Indices.	131

LIST OF TABLES

	<u>Pág.</u>
2.1 Planetary scale equatorial waves and its main characteristics	50
4.1 Gravity wave characteristics from airglow image data compared to the current results	88
5.1 Magnetic Latitude of the Magnetometer Stations and their Geographic Coordinates	94

LIST OF ABBREVIATIONS

COI	–	Cone of Influence
CWT	–	Continuous Wavelet Transform
EEJ	–	Equatorial Electrojet
FFT	–	Fast Fourier Transform
GW	–	Gravity Wave
IGRF	–	International Geomagnetic Reference Field Model
IPP	–	Inter Pulse Period
IRI	–	International Reference Ionosphere Model
NP	–	Number of Pulses
PW	–	Pulse Width
Sq	–	Solar Quiet current system
TD	–	Time Delay between Transmission and Acquisition

LIST OF SYMBOLS

\mathbf{E}_p	– polarization electric field
\mathbf{B}	– Earth's magnetic field
X	– geographic northward component of \mathbf{B}
Y	– geographic eastward component of \mathbf{B}
H	– horizontal component of \mathbf{B}
Z	– downward component of \mathbf{B}
D	– magnetic declination
I	– magnetic inclination
λ	– magnetic latitude
$\mathbf{V}_{e,i,n}$	– electron, ion, and neutral velocity
C_s	– ion-acoustic speed
$\underline{\sigma}$	– conductivity tensor
$\sigma_{0,1,2,3}$	– longitudinal, Pedersen, Hall, and Cowling conductivity
\mathbf{J}	– current density
$\nu_{e,i}$	– electron and ion collision frequency
$\Omega_{e,i}$	– electron and ion gyrofrequency
ψ	– anisotropic factor
$T_{e,i,n}$	– electron, ion, and neutral temperature
λ_{irr}	– plasma irregularity scale
λ_{Radar}	– radar wavelength

1 INTRODUCTION

The dissertation entitled **ELECTRIC AND MAGNETIC FIELD SIGNATURES OF GRAVITY WAVES AND 2-DAY PLANETARY WAVES IN THE EQUATORIAL E-REGION** is presented to the Space Geophysics program of National Institute for Space Research, INPE/MCT, in partial fulfillment of the requirements for the Master degree.

In this introductory part we provide a background for the studies performed in this thesis, and connect them to other research activities in the field of neutral atmosphere-ionosphere coupling. A brief review of ionospheric coupling processes due to gravity and planetary waves is given in Chapter 2. In Chapter 3 we present the methods, as well as magnetic indices and spectral analysis techniques. The data analysis and results are presented and discussed in Chapter 4. Chapter 5 presents conclusions and outlook. In Appendix A we present a review of ionospheric coherent backscatter radar, and in Appendix B and C we show some of the program codes applied in the present studies.

1.1 The Ionosphere

The ionosphere is a weakly ionized portion of the atmosphere, located between approximately 60 and 1500 km height. It is mainly generated by the interaction of either short wavelength solar radiation, or by precipitating energetic particles, with the neutral atoms and molecules. Based on the substructure of the ionosphere, it is usual divide it into a number of characteristic layers ([BRASSEUR; SOLOMON, 2005](#)). They are basically the D, E, and F regions ([Figure 1.1](#)).

1.1.1 D-region

The D-region is lower layer of the ionosphere, located between about 60 km and 90-95 km. Its ionization is mainly from photoionization of NO by Lyman- α radiation. Also, high energy cosmic rays contribute to the O₂ and N₂ ionization below 70 km.

1.1.2 E-region

The E-region is the portion of the Earth's ionosphere located between about 90-95 km and 130 km height. During the night the layer electron density decreases significantly, reaching values of the order of 5×10^9 electrons/m³, while over the day

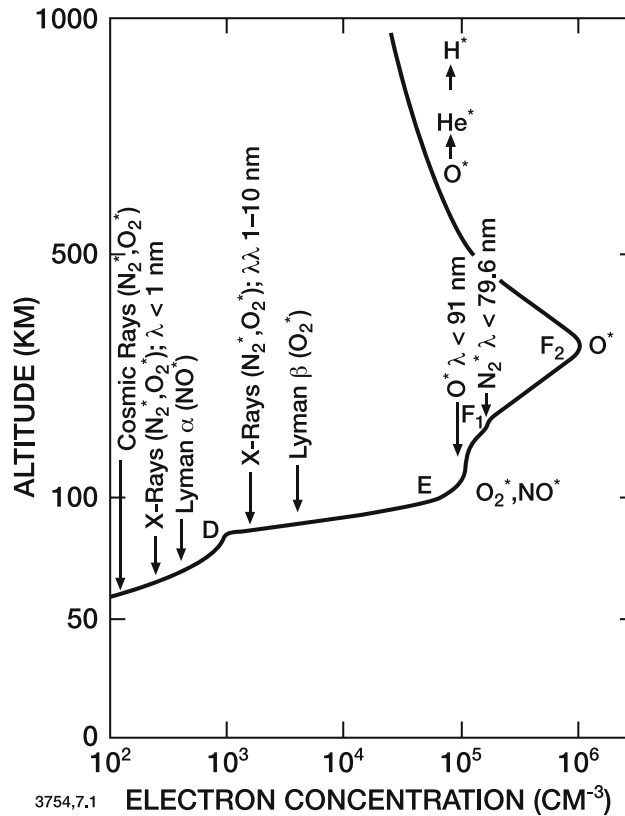


FIGURE 1.1 - Definition of the ionospheric layers based on the vertical distribution of electron density.

SOURCE: [Brasseur e Solomon \(2005\)](#)

it reaches 10^{11} electrons/ m^3 . The diurnal variation of the E-region is characterized by a behavior like the diurnal response of an α -Chapman layer to the solar ionization. On the average, its critical frequency, foE, varies with the zenithal angle χ in the form $\cos^{1/4}\chi$, which corresponds to electron density peak, NmE, variation in the form $\cos^{1/2}\chi$ ([HARGREAVES, 1992](#)).

This layer is formed by the ionization of neutral particles by solar ionizing radiation with absorption cross section of lower than $5 \times 10^{-18} \text{ cm}^2$. Solar radiation with λ in the range of 31-100 Å and $\lambda > 800 \text{ Å}$ are the most important sources of ionization. The solar lines of Lyman- β ($\lambda = 1025 \text{ Å}$) and the C(III) ($\lambda = 977 \text{ Å}$) have special importance for the O_2 ionization. The Lyman-continuum ($\lambda < 910 \text{ Å}$) also contributes trough the O ionization ([BANKS; KOCKARTS, 1973](#)). The main primary ions produced are N_2^+ , O_2^+ e O^+ , but subsequent reactions leads to NO^+ and O_2^+

ions to be the more abundant. The E-region is also characterized by the presence of metallic ions as Mg^+ , Fe^+ , Ca^+ and, Si^+ , credited to the disintegration of meteoric bodies in the terrestrial atmosphere.

1.1.3 F-region

The F-region begins above 130 km and is sometimes subdivided into two layers, F_1 and F_2 (BRASSEUR; SOLOMON, 2005). The main source of F-region ionization is the interaction of the extreme ultraviolet radiation with atomic oxygen and molecular nitrogen. The F_1 layer is composed primarily of O^+ and the maximum electron density in this layer occurs near approximately 170 km (KIVELSON; RUSSEL, 1995). However, the F_2 layer attains the ionospheric electron density maximum, even during nighttime. Above the F_2 layer, the electron density decreases. Helium He^+ and the hydrogen H^+ ions dominate, and the effect of the magnetic field on these charged particles becomes more important (BRASSEUR; SOLOMON, 2005).

1.2 Ionospheric Conductivity

The terrestrial ionosphere is permeated by magnetic and electric fields, which result in anisotropic properties of the plasma. Usually, the ionospheric conductivity is presented in a 3-directions format: along the magnetic field vector (\mathbf{B} direction); along the electric field vector component perpendicular to the magnetic field (\mathbf{E}_\perp); and simultaneously perpendicular to both ($\mathbf{B} \times \mathbf{E}$ direction).

The conductivity along the magnetic field, also known by direct or longitudinal conductivity is given by:

$$\sigma_0 = n \cdot e^2 \cdot \left(\frac{1}{m_e \cdot \nu_e} + \frac{1}{m_i \cdot \nu_i} \right). \quad (1.1)$$

The Pedersen or transversal conductivity is referred to the component in the \mathbf{E}_\perp direction, as given by:

$$\sigma_1 = n \cdot e^2 \cdot \left(\frac{\nu_e}{m_e \cdot (\nu_e^2 + \Omega_e^2)} + \frac{\nu_i}{m_i \cdot (\nu_i^2 + \Omega_i^2)} \right). \quad (1.2)$$

The Hall conductivity is referred to the conductivity in the $\mathbf{B} \times \mathbf{E}$ direction:

$$\sigma_2 = n \cdot e^2 \cdot \left(\frac{\Omega_e}{m_e \cdot (\nu_e^2 + \Omega_e^2)} - \frac{\Omega_i}{m_i \cdot (\nu_i^2 + \Omega_i^2)} \right). \quad (1.3)$$

In the [Equation 1.1](#), [Equation 1.2](#), and [Equation 1.3](#), m_e is the electron mass, m_i is the average ion mass, $\Omega_{e,i}$ are the gyrofrequencies, $\nu_{e,i}$ are the collision frequencies, e is the electron charge, and n is the plasma density. The subscript e and i indicates the electron and ion terms, respectively.

The altitude distributions of the direct, Pedersen and Hall conductivities are shown in [Figure 1.2](#). It can be seen that the Pedersen conductivity has two peaks defining the daytime E- and F-regions. The Hall conductivity is comparable to the Pedersen conductivity in the lower E-region but falls rapidly with increasing altitude to be negligible compared to the Pedersen conductivity above about 200 km. The direct conductivity is much greater than the Pedersen and Hall conductivities at any altitude so that it is referred within a separated scale on the top of the graph and we treat the magnetic field lines as approximately electric equipotentials. Another interesting feature in [Figure 1.2](#) is that at night the E-region conductivity becomes very low compared to the F-region conductivity ([HEELIS, 2004](#)).

Unifying the three conductivities, taking into account the geometry of the terrestrial magnetic and electric field, the electrical conductivity in the tensor form is given by ([DENARDINI, 2003](#)):

$$\underline{\sigma} = \begin{pmatrix} \sigma_0 \cdot \cos^2 I + \sigma_1 \cdot \sin^2 I & \sigma_2 \cdot \sin I & -(\sigma_0 - \sigma_1) \cdot \sin I \cdot \cos I \\ -\sigma_2 \cdot \sin I & \sigma_1 & -\sigma_2 \cdot \cos I \\ -(\sigma_0 - \sigma_1) \cdot \sin I \cdot \cos I & \sigma_2 \cdot \cos I & \sigma_1 \cdot \cos^2 I + \sigma_0 \cdot \sin^2 I \end{pmatrix} \quad (1.4)$$

where I is the inclination angle of \mathbf{B} in relation to the terrestrial surface. The coordinate system related to [Equation 1.4](#) is shown in [Figure 1.3](#).

1.3 Ionospheric E-region Dynamo

The ionosphere is characterized by the presence of neutral wind motions driven by tidal oscillations that propagate from below and by in situ heating. Tidal oscillations driven by absorption of solar radiation dominate the neutral atmosphere motions in the E-region ([HEELIS, 2004](#)). The dynamo action can be described in terms of

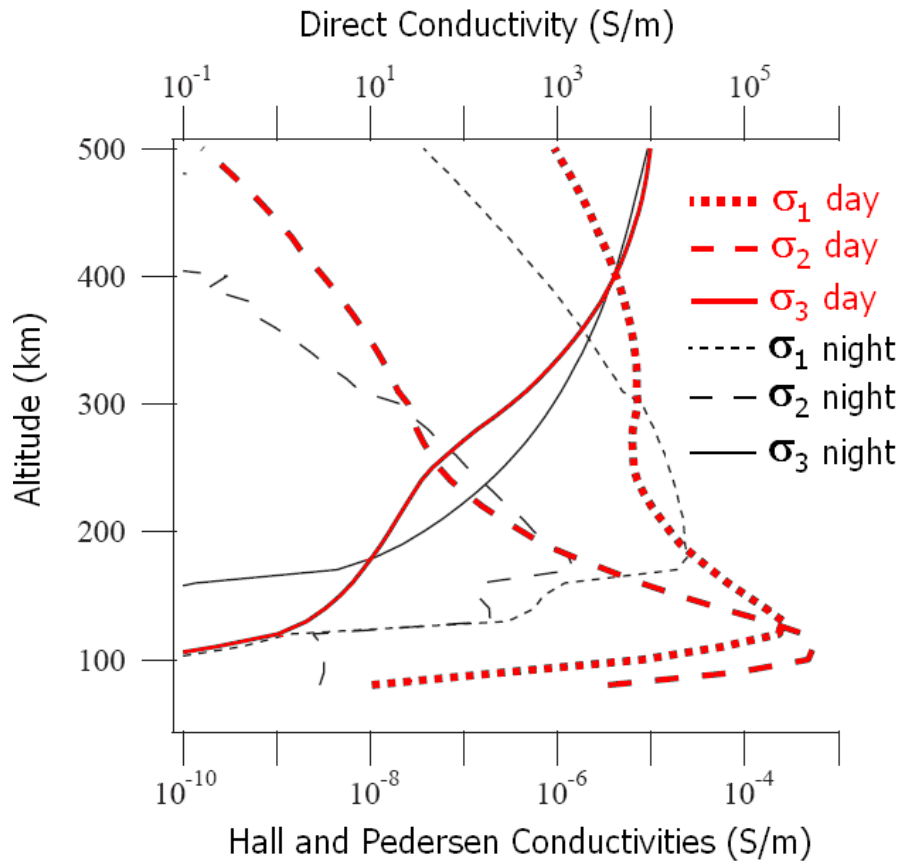


FIGURE 1.2 - Altitude profiles of the direct conductivity, σ_0 , and the Hall and Pedersen conductivities, respectively, σ_2 and σ_1 . Red curves denote daytime values. Black curves denote nighttime values.

SOURCE: Adapted from [Heelis \(2004\)](#)

either 'induced electric fields' or 'wind-driven currents' ([RISHBETH, 1997](#)). Both 'voltage' and 'current' descriptions could in principle be applied to both E- and F-layer dynamo, but the 'voltage description' is more useful for the E-layer and 'current description' for the F-layer ([RISHBETH, 1997](#)). The voltage generator is described as follow:

- the wind \mathbf{U} induces an electric field $\mathbf{E}_i = \mathbf{U} \times \mathbf{B}$;
- the induced electric field drives a current $\mathbf{J} = \underline{\sigma} \cdot (\mathbf{U} \times \mathbf{B})$;
- in general this current is not divergence-free everywhere. Electric charge accumulates wherever $\text{div}(\underline{\sigma} \cdot (\mathbf{U} \times \mathbf{B})) \neq 0$; and

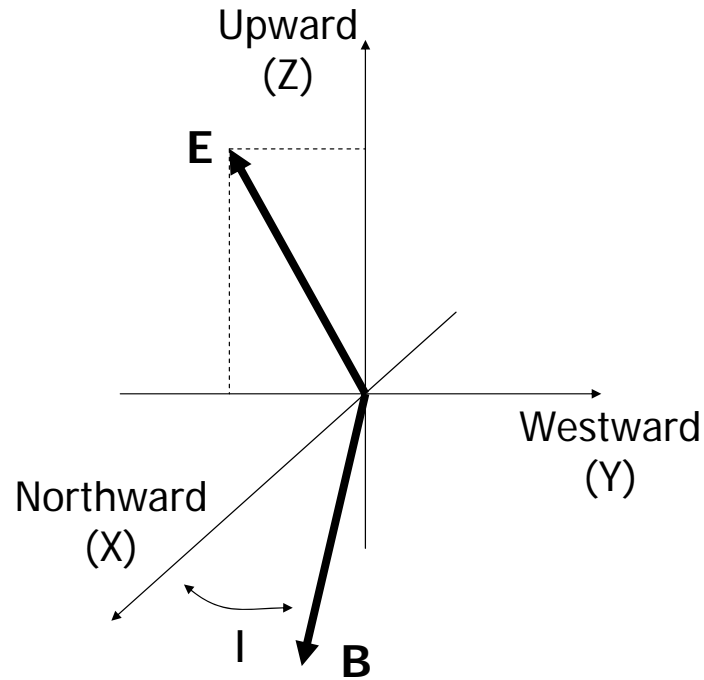


FIGURE 1.3 - Coordinate system related to the conductivity tensor showing the electric and geomagnetic fields, and the inclination I .

- by Poisson's Law the charge produces a polarization field \mathbf{E}_p which continuously adjusts itself to make the total current divergence-free so that $\text{div}(\underline{\sigma} \cdot (\mathbf{U} \times \mathbf{B} + \mathbf{E}_p)) \neq 0$ everywhere.

Thus, at any point in the ionosphere, \mathbf{E}_i represent the electromotive field (e.m.f.) induced locally by the wind, whereas the polarization electric field \mathbf{E}_p may be considered as the sum of the e.m.f.'s produced at remote points, which builds up to satisfy the requirement of current continuity in the dynamo circuit. The resulting ionospheric current system is known as Solar Quiet current system (Sq). [Figure 1.4](#) schematize the E-region Ionospheric Dynamo and the resulting Sq current system, based on the characteristics presented above.

In the E-layer, the induced (\mathbf{E}_i) and polarization (\mathbf{E}_p) fields are generally comparable in magnitude. Even during the night, when the electron density is smaller than that during daytime, the magnitude of the longitudinal conductivity (across the magnetic field lines) is enough to allow currents to flow to maintain the polarization field.

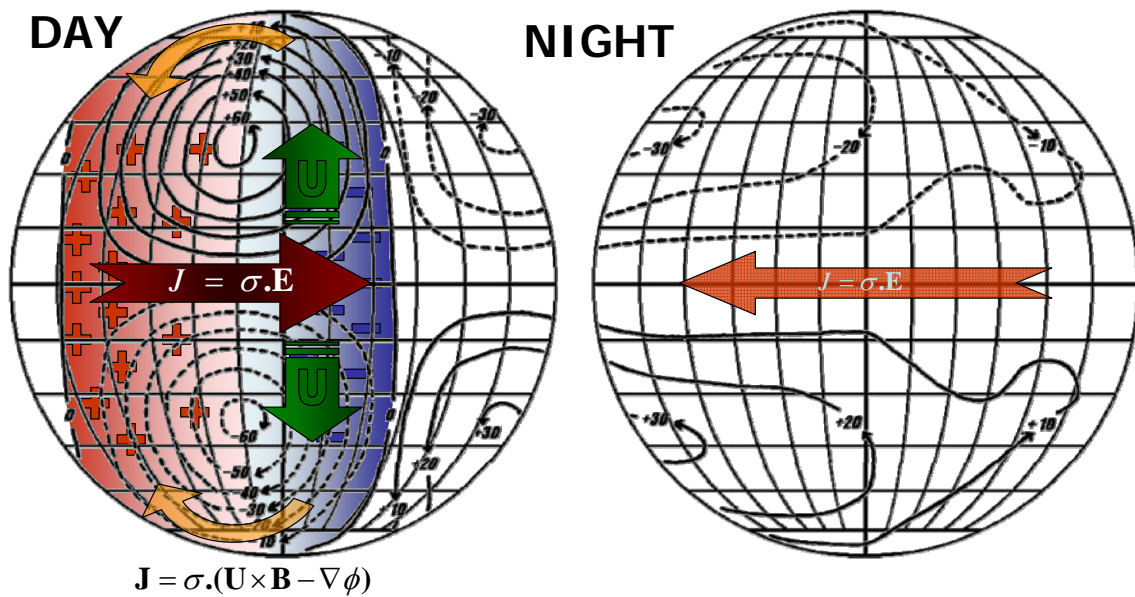


FIGURE 1.4 - Scheme of ionospheric currents and electric fields based on the Ionospheric Dynamo Theory.

SOURCE: Adapted from [Denardini \(2003\)](#)

1.4 Equatorial Electrojet

At the magnetic dip equator the inclination is null, then the conductivity tensor ($\underline{\sigma}$) can be simplified to:

$$\underline{\sigma} = \begin{pmatrix} \sigma_0 & 0 & 0 \\ 0 & \sigma_1 & -\sigma_2 \\ 0 & \sigma_2 & \sigma_1 \end{pmatrix} \quad (1.5)$$

Considering only the plane perpendicular to the magnetic field at the equator, we obtain the following equations from the relation $\mathbf{J} = \underline{\sigma} \cdot \mathbf{E}$, :

$$\begin{aligned} J_y &= \sigma_1 \cdot E_y - \sigma_2 \cdot E_z \\ J_z &= \sigma_2 \cdot E_y + \sigma_1 \cdot E_z \end{aligned} \quad (1.6)$$

where the z-axis points in the vertical direction and y-axis is eastward. In this case, since the conductivity is drastically reduced below and above the conductivity peak (around 105 km), as show in [Figure 1.2](#), the vertical current can be considered as inhibited ($J_z = 0$). Then, the solution of [Equation 1.6](#) is given by:

$$J_y = \left(\sigma_1 + \frac{\sigma_2^2}{\sigma_1} \right) E_y \Rightarrow J_y = \sigma_3 \cdot E_y, \quad (1.7)$$

where σ_3 is the Cowling conductivity, which points perpendicular to the Earth's magnetic field, and presents a maximum amplitude in the heights between 90 and 120 km. So, the sum of these effects generates an eastward electron current flowing in the dayside hemisphere and a westward in the nightside hemisphere at about 105 km of altitude in the equatorial E region. It covers a latitudinal range of $\pm 3^\circ$ around the dip equator and is named equatorial electrojet (EEJ) ([FORBES, 1981](#)).

1.5 Equatorial Electrojet Plasma Irregularities

Studies of the equatorial ionosphere using VHF radars have shown echoes backscattered from plasma irregularities in the EEJ. Spectral studies of such echoes (through Fourier Transform) showed two distinct spectral signatures for the observed irregularities. They were labeled Type I and Type II, but they are also known for their theory of development as modified two-stream ([FARLEY, 1963](#); [BUNEMAN, 1963](#)) and gradient drift ([ROGISTER; D'ANGELO, 1970](#)) instabilities, respectively. [Figure 1.5](#) presents examples of EEJ irregularities spectra obtained by coherent radars.

1.5.1 Modified Two-Stream Instability and Type I echoes

Irregularities related to the modified two-stream instability, or Farley-Buneman instability, are known as Type I echoes. They are characterized by a narrow spectrum with high amplitude that dominates the upper portion of the electrojet. In magnetically quiet days, these type of echoes are expected to be observed between 10 and 13 hours LT ([FORBES, 1981](#)). In magnetically disturbed days, there may occur an increase in the production of this irregularity type due to energy release from the magnetic disturbance ([DENARDINI, 2003](#)). These Type I echoes are only observed when the difference between the electron velocity V_e and the ion velocity V_i ($|V_e - V_i|$) is higher than the ion-acoustic speed C_s ([BROCHET et al., 1978](#)). So that, the threshold condition to the observation of Type I irregularity can be written as:

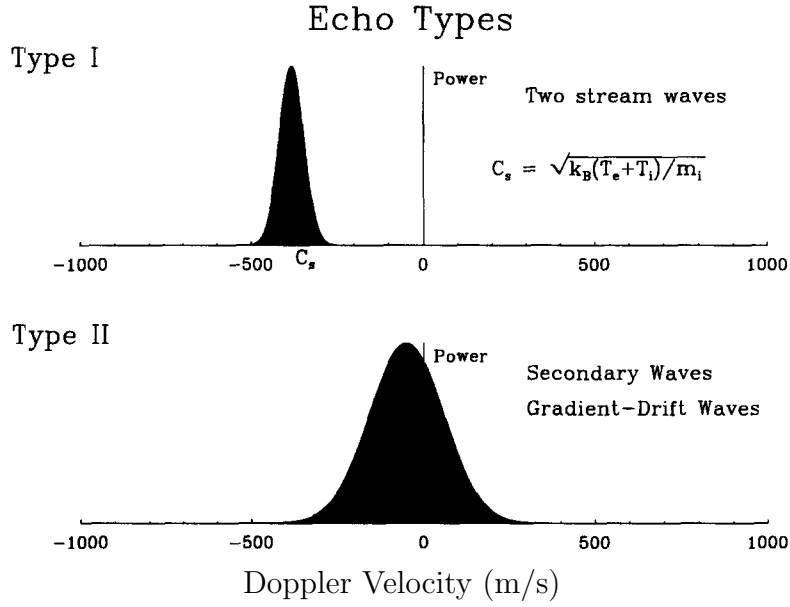


FIGURE 1.5 - Examples of Type I (top) and Type II (bottom) irregularities spectra obtained by coherent radars.

SOURCE: [Schlegel \(1996\)](#)

$$\mathbf{k}/k \cdot (V_e - V_i) = C_s(1 + \psi), \quad (1.8)$$

where \mathbf{k} is the irregularity wavenumber and ψ is discussed ahead. The ion-acoustic velocity C_s (the speed of sound in the plasma), around 400 m/s, is given by ([HARGREAVES, 1992](#)):

$$C_s = \left[\frac{K(T_e - T_i)}{m_i} \right]^{1/2}, \quad (1.9)$$

where T_e and T_i are the electron and ion temperatures, respectively, K is the Boltzmann constant, and m_i is the ion mass average. ψ is the anisotropic factor, given by:

$$\psi = \frac{\nu_e \cdot \nu_i}{\Omega_e \cdot \Omega_i} \cdot \left(\sin^2 \alpha + \frac{\Omega_e^2}{\nu_e^2} \cdot \cos^2 \alpha \right), \quad (1.10)$$

where α is the angle between the wave and the magnetic field, $\nu_{e,i}$ and $\Omega_{e,i}$ are

the collision frequencies and the gyrofrequencies. The subscript e and i indicate the electron and ion terms, respectively. The ion-acoustic speed threshold depends on ψ , which depends on α . In the case of propagation normal to the magnetic field in the E-region, ψ is approximately 0.3, but rapidly increases as it moves away from 90° since Ω_e is around 100 times higher than ν_e (HARGREAVES, 1992). This is the reason why electrostatic waves generated by this mechanism commonly propagates normal to the magnetic field and why the difference between their velocities is close to the ion-acoustic speed.

1.5.2 Gradient-Drift Instability and Type II echoes

Irregularities related to the Gradient-Drift instability are known as Type II echoes and are characterized by a broader spectrum in relation to the Type I irregularities but with smaller amplitude. These echoes are observed with very small values of eastward drift velocity during daytime (COHEN; BOWLES, 1967; BALSLEY, 1969), and are commonly observed during nighttime. Also, when the daytime electric field crosses zero, the echoes may momentarily disappear, after reappearing in different altitudes (FEJER; KELLEY, 1980). During magnetic quiet days, the Type II irregularities are found predominantly in the lower portion of the electrojet and they can be observed from sunrise to sunset (DENARDINI, 1999). During magnetically disturbed periods the height range where these echoes dominates seems to rise up with respect to the quiet day height (ABDU et al., 2003).

This type of instability occurs in non-homogeneous plasma when polarization electric fields, \mathbf{E}_p , has a strong enough component in the direction parallel to the gradient of density.

The upward electric field \mathbf{E}_p produces a westward $\mathbf{E}_p \times \mathbf{B}$ force, and hence a westward plasma drift. Due to the larger collision with neutrals, the ion drift is smaller than the Hall drift of the electrons. As a result, perturbation electric fields δE develops inside the density perturbation, as shown in Figure 1.6, wherein the δE is shown directed eastward and westward in the rarefied and denser regions of the density perturbation, respectively. Thus, the eastward (westward) δE causes the upward (downward) drift of the rarefied (denser) plasma, contributing to enhance the amplitude of the density perturbation, leaving to the instability process. Therefore, the amplitude of the density perturbations rise up in relation to the background density. The same effect occurs at night when the electron density gradient and the vertical

polarization field are pointing downward. Diffusion and recombination effects oppose the wave growth and set a threshold to the instability occurrence.

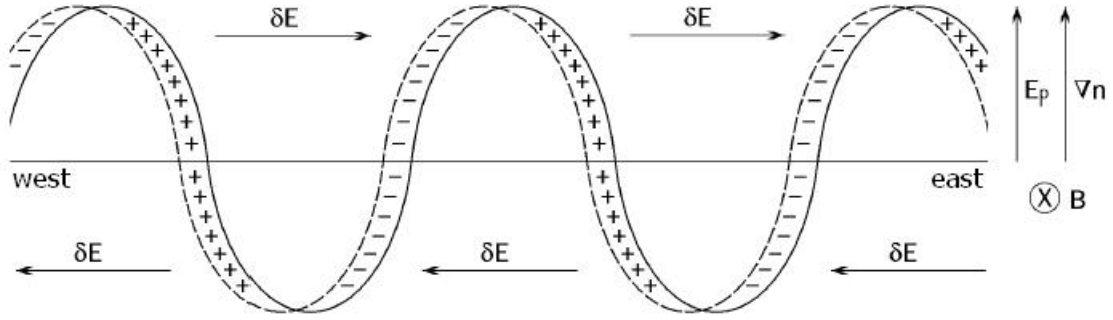


FIGURE 1.6 - Simplified representation of the gradient drift instability mechanism in the diurnal equatorial electrojet.

SOURCE: [Fejer e Kelley \(1980\)](#)

1.5.3 Neutral Winds and Phase Velocities of EEJ instabilities

The phase velocity (velocity which the plasma instability spreads) of both EEJ irregularities are not directly modified by the presence of neutral winds ([SATO, 1975](#)). They are related to the electron phase velocity V_e and ion velocity V_i as per ([ROGISTER; D'ANGELO, 1970](#)):

$$V_p = \hat{\mathbf{k}} \cdot (\mathbf{V}_e + \psi \mathbf{V}_i) / (1 + \psi), \quad (1.11)$$

where $\hat{\mathbf{k}}$ is the orthonormal irregularity wavenumber ($= \mathbf{k} / |\mathbf{k}|$).

The electron movement is mainly controlled by electromagnetic fields. Independently of the wind, it is given by ([BROCHET et al., 1978](#)):

$$\mathbf{V}_e = \frac{\mathbf{E} \times \mathbf{B}}{|\mathbf{B}|^2}, \quad (1.12)$$

where \mathbf{B} is the Earth's magnetic field and B denotes its module. At the E-region, the ion movement is controlled by ion-neutral collisions, such that

$$\mathbf{V}_i = \mathbf{V}_n, \quad (1.13)$$

where \mathbf{V}_n is the neutral wind velocity.

Richmond (1973) showed that the vertical polarization electric field E_z is given by:

$$E_z = \frac{\int \sigma_2 ds}{\int \sigma_1 ds} \cdot E_y - B_0 \cdot \frac{\int \sigma_1 V_{ny} ds}{\int \sigma_1 ds}, \quad (1.14)$$

where the integrals are calculated along the magnetic field lines (ds). V_{ny} is the neutral wind velocity in the east-west direction and E_y is the electric field in the same direction.

Using Equation 1.12 and Equation 1.14, the electron velocity in the east-west direction is (BROCHET et al., 1978) given by:

$$V_{ey} = -\frac{E_z}{B_0} = -\frac{E_y \int \sigma_2 ds}{B_0 \int \sigma_1 ds} + \frac{\int \sigma_1 V_{ny} ds}{\int \sigma_1 ds}. \quad (1.15)$$

The first term on the right-hand side represents the contribution in the absence of winds ($(V_{e0})_y$) generated by the Dynamo. The second term is V_{ny} averaged along the magnetic field line ($\langle V_{ny} \rangle$). So that,

$$V_{ey} = (V_{e0})_y + \langle V_{ny} \rangle. \quad (1.16)$$

For a horizontal east-west wind velocity \mathbf{V}_n and symmetrical EEJ, the other components of \mathbf{V}_e are all independent of the wind, and

$$\mathbf{V}_e = \mathbf{V}_{e0} + \langle \mathbf{V}_n \rangle. \quad (1.17)$$

In Equation 1.17, \mathbf{V}_{e0} is the electron velocity without any wind effect in the primary electric field E_y .

The conclusions related to ions (corresponding to Equation 1.13) are given by:

$$\mathbf{V}_i = \mathbf{V}_{i0} + \mathbf{V}_n, \quad (1.18)$$

where \mathbf{V}_n is the current value of the neutral wind velocity in the point of interest.

The phase velocity of Type I irregularities is close to the velocity of the marginally

unstable wave, which is obtained by substitution of Equation 1.8 in Equation 1.11:

$$V_{pI} = \hat{\mathbf{k}} \cdot (\mathbf{V}_e + \psi \mathbf{V}_i) / (1 + \psi) = C_s + \hat{\mathbf{k}} \cdot \mathbf{V}_i \quad (1.19)$$

Equation 1.19 shows that effect of the winds in Type I irregularities velocity is a variation in the form of $\Delta V_{pI} = \hat{\mathbf{k}} \cdot \mathbf{V}_i$.

The previous analysis presented to Type I can be done to Type II velocities too. In this case, Equation 1.11, Equation 1.12, and Equation 1.13 will lead to

$$V_{pII} = (V_{pII})_0 + \hat{\mathbf{k}} \cdot \mathbf{V}_n + \hat{\mathbf{k}} \cdot \frac{\langle \mathbf{V}_n \rangle - \mathbf{V}_n}{1 + \psi}, \quad (1.20)$$

where $(V_{pII})_0$ is the phase velocity which would be observed in the absence of winds.

If $\mathbf{V}_n = \langle \mathbf{V}_n \rangle$, electrons and ions are drifting with the same velocity \mathbf{V}_n , so that both Type I and Type II irregularities present the same variation in the phase velocities $\hat{\mathbf{k}} \cdot \mathbf{V}_n$ (BROCHET et al., 1978). This condition is fulfilled when the wind is constant in height and latitude, i.e., along the magnetic field lines. Same conclusion can be achieved if the curvature of the magnetic field lines are neglected and if the wind depends only on the altitude, which corresponds to the results of Sato (1975).

2 GRAVITY WAVES AND PLANETARY WAVES

In the present section we introduce some previous studies that relate planetary waves and gravity waves effects with variability observed in the ionosphere. It is not intended to present a full review covering all the features, but the results that are related to this thesis.

2.1 Gravity Waves

Gravity waves are oscillation with relatively short horizontal wavelengths (typically 10-1000 km) that arise in stably stratified fluid when air bulk are vertically shifted. These waves can be produced by air flux over the mountains (orographic sources) or by non-orographic sources, such as storms, frontal systems and instabilities. The propagation of such waves through the atmosphere depends on the vertical distribution of winds and temperature, which varies with the season and the static stability (BRASSEUR; SOLOMON, 2005).

Atmospheric gravity waves have been a topic of very strong research activity in the recent years since they affect the atmospheric structure, circulation and variability. The main influence of such type of wave is seen in the middle atmosphere, between around 10 and 100 km of altitude, due to atmospheric density decreasing and wave amplitude increasing with height (FRITTS; ALEXANDER, 2003).

2.1.1 Electric Field Fluctuations in the EEJ due to Gravity Waves I - Observations

Gravity wave represents a source of dynamical fluctuations in the electrojet region (FORBES, 1981). Reddy e Devasia (1976) reported short-period (20-30 min) fluctuations in the electron drifts ($\delta V_D \sim 25-50$ m/s) from their VHF radar measurements at Thumba. They also have found a close correlation between these fluctuations and the horizontal magnetic variations at nearby Trivandrum. Anandarao et al. (1978) inferred vertical winds of the order of 10-20 m/s with a vertical wavelength of 50 km from analysis of a barium cloud release over Thumba, which they interpret as being of gravity wave origin. Still, Reddy (1981) analyzed the variations of the EEJ Type II irregularity velocities during different magnetic activity levels (Figure 2.1). In quiet days ($A_p < 10$), the electric field have shown a relatively smooth increase and decrease during the diurnal hours. During the period of very low activity ($A_p = 8$, in 3 March 1978), the presence of small but persistent fluctuations were observed.

Since the electric fields are mainly controlled by the dynamo action during the day, such type of fluctuations are believed to be related to the interaction between the ionosphere and the gravity waves. During disturbed periods, it can be seen that variations related to the magnetic events are more significant than the normal diurnal variation. Gravity wave oscillation of ~ 20 -min period in the 50 MHz in the range-time-intensity (RTI) radar maps over São Luís, Brazil, were reported by [Abdu et al. \(2002\)](#). Also, this study was the first report of GW's signatures in Type I echoes.

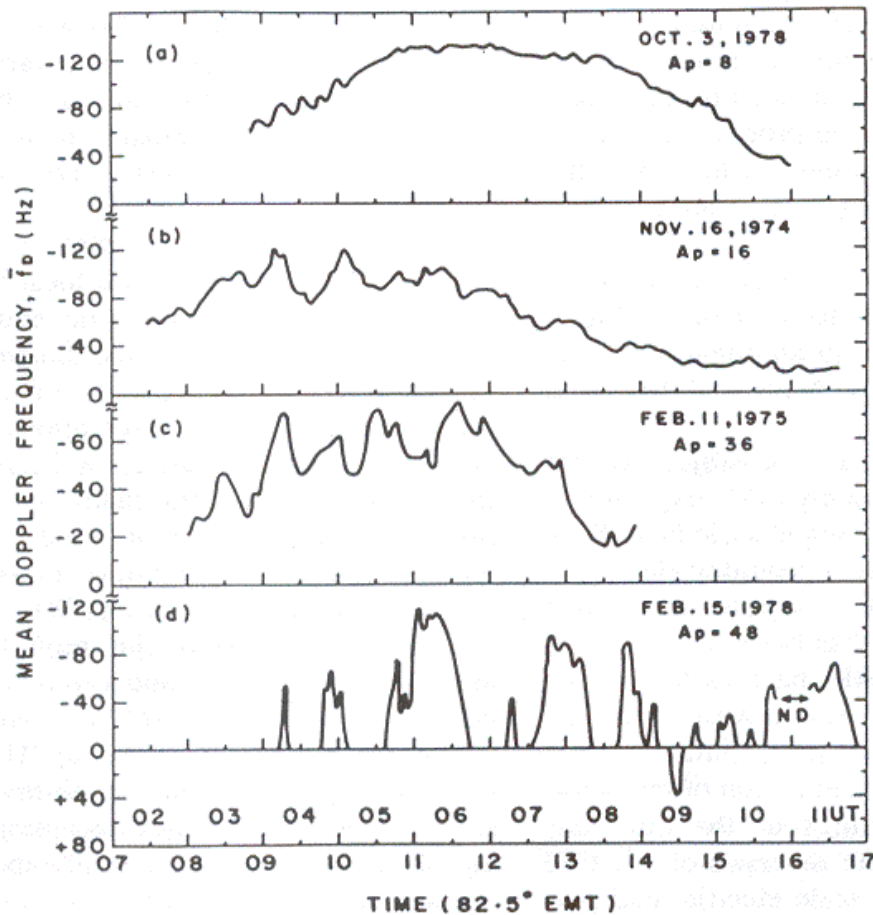


FIGURE 2.1 - Time variations of Type II irregularity velocities of the backscatter radar signals on (a) a magnetically quiet day, (b) and (c) on moderately disturbed days and (d) on a magnetic storm day.

SOURCE: [Reddy \(1981\)](#)

Oscillations with short time scales similar to those observed by [Reddy \(1981\)](#) and [Abdu et al. \(2002\)](#) were also observed by [Denardini \(2003\)](#) in the vertical electric

field early in the morning (between 8 and 9 hours LT) during quiet days, as shown in Figure 2.2. Denardini (2003) did not analyze the causes of such variations, but he claimed to be the result of the generation of electric fields by gravity waves. He based this assumption in the fact that during geomagnetic quiet days the neutral winds are the main drivers of the ionospheric electric fields. Thus, the short-period oscillations in vertical electric fields should be attributed to gravity waves (Denardini, private communication, 2008).

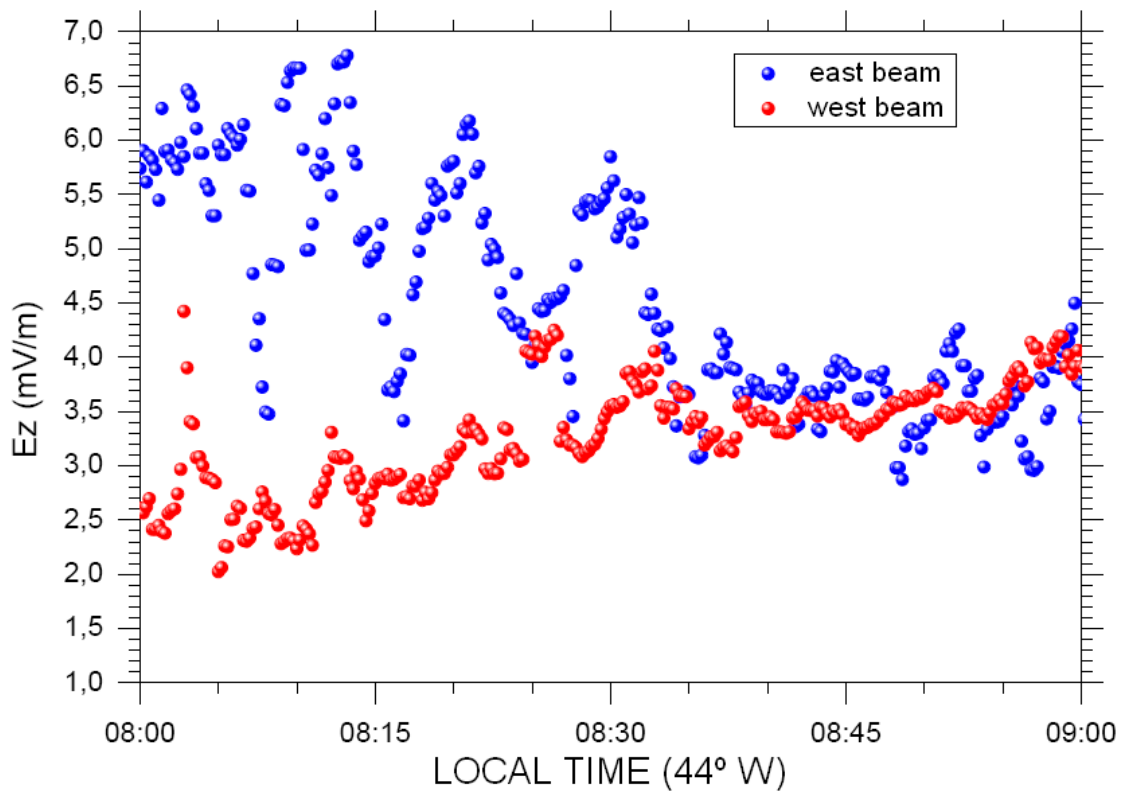


FIGURE 2.2 - Variation of the average vertical electric field between 8 and 9 hours LT inferred from RESCO radar data during equinoctial period using 30° east beam (blue circles) and 30° west beam (red circles).

SOURCE: Denardini (2003)

2.1.2 Electric Field Fluctuations in the EEJ due to Gravity Waves II - Theoretical Studies

Anandarao (1976) analyzed the effects of gravity wave winds and wind shears on equatorial electrojet. Figure 2.3 shows the vertical profiles of the EEJ current density

with gravity wave winds action (solid line) and without the wind action (dashed line) using two different vertical wavelength: $\lambda_z=20$ km (left panel) and $\lambda_z=10$ km (right panel). The figure shows that the effect of gravity waves in the EEJ is significantly in the height region of 110-150 km, where the background vertical electric field rapidly decays. Below 110 km, however, since the background electric field is strong, the wind contribution is not so significant.

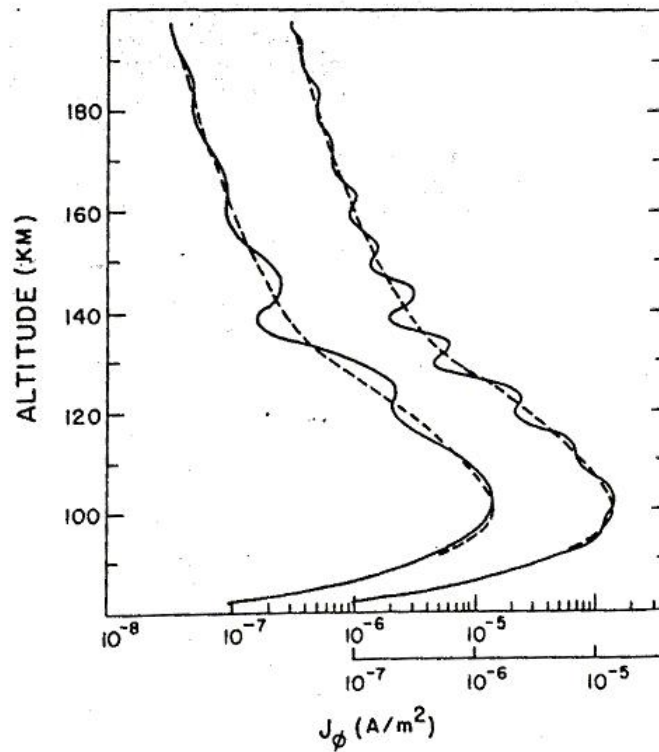


FIGURE 2.3 - Eastward current density modulated by gravity waves (solid line) and without their action (dashed line). The left curve corresponds to $\lambda_z=20$ km and the right one to $\lambda_z=10$ km.

SOURCE: [Anandarao \(1976\)](#)

[Reddy e Devasia \(1981\)](#) have theoretically analyzed the vertical structure of electric fields and currents generated by height-varying east-west winds in the EEJ region through the use of theoretical wind models and a variety of wind observations. Their results are summarized as follow:

- the vertical shear in zonal wind related to gravity waves may affect sig-

nificantly the height structure of current density and electric fields in the EEJ. However, such effect is very small in height-integrated current intensity inside $\pm 2^\circ$ of latitudinal range;

- the currents and electric fields generated by winds are characterized by strong gradients in height, latitude and by a reversion in its direction; and
- in the magnetic equator, the currents and electric fields generated by winds are frequently small (10-30%) when compared to the east-west currents and polarization fields generated by east-west global scale electric fields around midday.

The generation of electric fields by gravity wave winds in the equatorial ionosphere was investigated in a one-dimensional (vertical) sense by [Kato \(1973\)](#), which is later modified in a two-dimensional treatment by [Anandarao et al. \(1977\)](#). [Kato \(1973\)](#) first pointed out that the polarization field arised from the $\mathbf{U} \times \mathbf{B}$ electromagnetic field does not sufficiently develop to cancel the total electric field completely; that is, $\mathbf{E}' = \mathbf{E} + \mathbf{U} \times \mathbf{B} \neq 0$. [Kato \(1973\)](#) defines an efficiency factor:

$$R = E'_z / (\mathbf{U} \times \mathbf{B})_z \quad (2.1)$$

which defines how efficiently a neutral wind \mathbf{U} can produce \mathbf{E}' . In the equation, the subscript z identifies the vertical components. Calculating R to the equatorial case, $I=0$, and at 100 km of altitude, [Anandarao et al. \(1977\)](#) obtained an asymptotic value of $R \approx 0.7$ using vertical wavelength $\lambda_z=20$ km and horizontal wavelength $\lambda_h=50$ km. Kato's treatment assumes $\lambda_z \gg \lambda_h$ and $E_y \ll E_z$. A more general expression to the efficiency factor deduced by [Anandarao et al. \(1977\)](#) indicates that R for $\lambda_h=50$ km obtained by [Kato \(1973\)](#) is overestimated by a factor of 5 ([Figure 2.4](#)). However, for $\lambda_h \geq 300$ km, R values can be in the range from 0.3 ($\lambda_z \sim 10$ km) to 0.5 ($\lambda_z \sim 20$ km) ([Figure 2.5](#)).

2.2 Planetary Waves

Planetary scale equatorial waves play an important role in the tropical atmosphere dynamics. These waves are forced by large-scale unsteady convective clusters in the tropical troposphere and accompanying latent heat release. They propagate horizontally and vertically carrying momentum to the middle and upper atmosphere

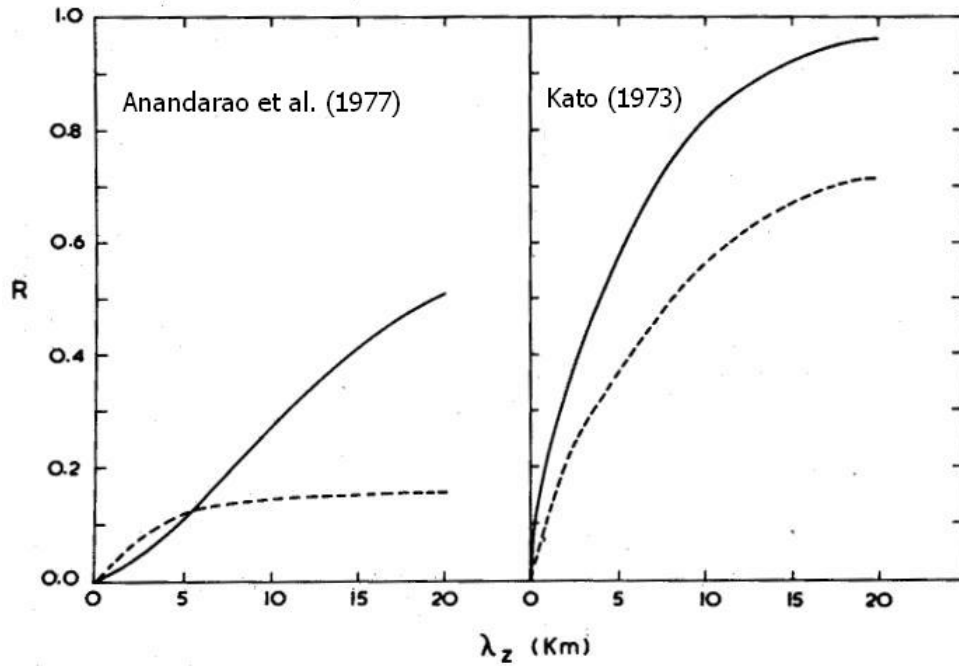


FIGURE 2.4 - Efficiency factor R versus λ_z for $\lambda_h=50$ km. The solid line represents the case where vertical scale height H_z is null and dashed line to $H_z=-k_z$, where k_z is the vertical wavenumber.

SOURCE: [Anandarao et al. \(1977\)](#)

([PANCHEVA et al., 2008](#)). A brief description of the main characteristics of such waves is given in [Table 2.1](#).

Kelvin waves are one of the more dominant equatorial waves. The change in sign of Coriolis parameter in the equator yields the existence of this equatorial wave type. Kelvin waves are a special type of gravity waves, modified by the Earth rotation ([ANDREWS et al., 1987](#)). Main characteristics of these is that they propagate eastward, are equatorially trapped (i.e., their geopotential perturbations, zonal velocity, and temperature varies in latitude as a Gaussian function centered at the equator), and are believed to be excited by tropical convection heating ([HOLTON, 2004](#)). In an ideal atmosphere, there are no meridional perturbations related to Kelvin waves ([PANCHEVA et al., 2008](#)).

Rossby waves are types of waves that propagate westward. The 5-day wave is the more important symmetrical meridional mode. Its latitudinal structure shows meridional winds and pressure maxima at middle latitudes, while the zonal wind maximum

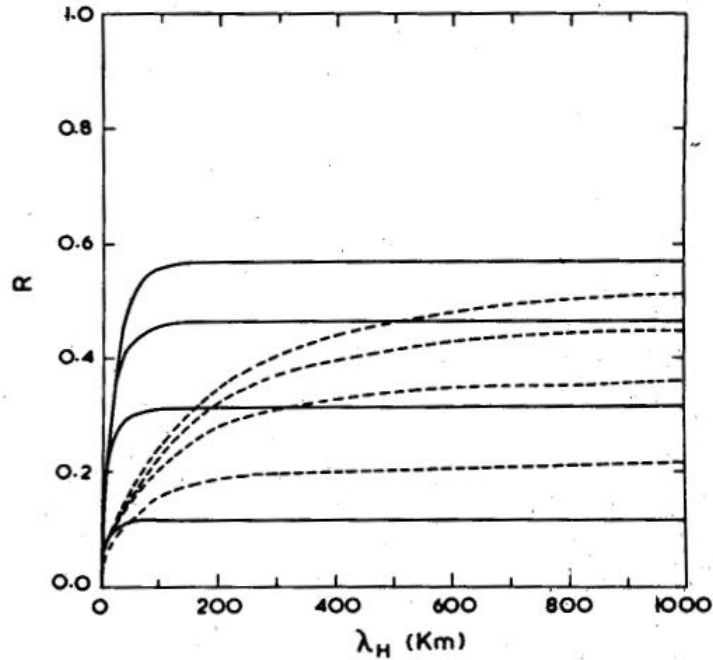


FIGURE 2.5 - Efficiency factor R versus λ_h . The solid line group represents the case where vertical scale height H_z is null and dashed line to $H_z = -k_z$. The four curves in each group are for the cases of $\lambda_z = 5, 10, 15,$ and 20 km (from bottom to top in the diagram).

SOURCE: [Anandarao et al. \(1977\)](#)

is observed over the equator ([PANCHEVA et al., 2008](#)). Mixed Rossby-gravity waves propagate westward, with vertical wavelengths of the order of 6-8 km. This wave is generally trapped laterally in the tropics, but propagate vertically and zonally, likely Kelvin waves. The horizontal structure (geopotential and winds) of the tropic trapped waves is shown in [Figure 2.6](#).

2.2.1 Signatures of Planetary Waves in the Low-Latitude Ionosphere

Manifestation of planetary wave effects in the ionosphere were first recognized by [Chen \(1992\)](#) in the Equatorial Anomaly. [Forbes e Leveroni \(1992\)](#) found a quasi 16-day oscillation in the the equatorial ionosphere likely connected with the upward penetration of a free Rossby mode. In view of the theoretical difficulty of forecasting the propagation of such waves to ionospheric heights ([HAGAN et al., 1993](#); [FORBES et al., 1995](#)), those results were related to the electrodynamical signature of the interaction between planetary waves and the ionospheric dynamo region (lower E-region).

TABLE 2.1 - Planetary scale equatorial waves and its main characteristics

Direction of Propagation	Type	Period* (days)	(s, n)	Additional Description
East	Slow Kelvin	15 (10-20)	(1,-)	Gravity
	Fast Kelvin	6 (6-10)	(1-2,-)	Gravity
	Ultra Fast Kelvin	3.5 (3-4)	(1-2,-)	Gravity
West	Rossby	2	(1,-2)	Rotational, first symmetric
	Rossby	4	(1,-3)	Rotational, first asymmetric
	Rossby	5	(1,-4)	Rotational, second symmetric
	Rossby	10	(2,-3)	Rotational, second asymmetric
	Rossby	16	(3,-3)	Assymmetric

(*) the number in the parenthesis indicates the observed period which includes the Doppler shift due to the background wind flux.

SOURCE: Based on [Forbes \(1995\)](#) and [Takahashi et al. \(2006\)](#)

[Parish et al. \(1994\)](#) identified 2-, 5-, 10- and 16-day periodicities in the EEJ current, which they attributed to planetary waves ([Figure 2.7](#)). Their analysis suggested also that nonlinear interactions between the planetary waves and the diurnal and semidiurnal tides could be another driving source of these oscillations.

[Gurubaran et al. \(2001\)](#) identified the signatures of the quasi-2-day variability in the equatorial electrojet using magnetometers and showed a reasonable correlation with the 2-day wave measured by the MF radar situated close to the geomagnetic stations. Their results show that there is a lag between the occurrences in the two events. The two-day periodicity in the EEJ currents revealed an inter-annual variability in the planetary wave activity. Still, the results show that the occurrence of such variability is more frequent during late solstice months, i.e., January, February, July, and August. Also, the sporadic occurrence of planetary waves, although not so strong as in late solstice months, are reported during April, May, September, and November.

[Abdu et al. \(2006\)](#) reported planetary wave oscillations of 3-5 day periodicities in

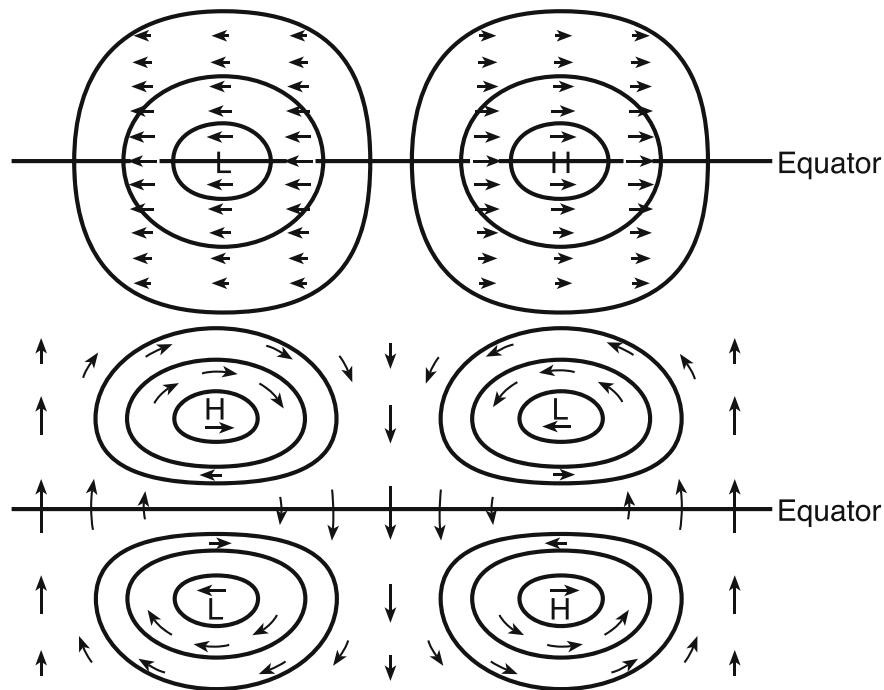


FIGURE 2.6 - Geopotential and wind structure of an equatorial Kelvin wave (upper panel) and mixed Rossby-gravity wave (lower panel).

SOURCE: [Brasseur e Solomon \(2005\)](#)

the equatorial F-layer evening pre-reversal electric field/vertical drift as measured by a ionosonde, that were correlated with mesospheric winds as measured by a meteor radar. These results were interpreted by them as due to the interaction with the dynamo region by upward propagating planetary waves.

Based on wind measurements at four sites located into different latitude and longitude [Takahashi et al. \(2007\)](#) identified an Ultra Fast Kelvin (UFK) wave for the interval March 1-16, 2005. Temperature data from TIMED/SABER satellite also showed an UFK wave propagating from 30 to 90 km height. During the same period, the F-layer virtual height ($h'F$) and the critical frequency ($foF2$) also showed 4-day oscillation ([Figure 2.8](#)). Their results suggest that UFK waves propagate from troposphere to ionosphere. The UFK wave could affect the rising of the F-layer after sunset through changes induced by the wave in the E-region and/or in the lower thermosphere neutral winds. Since this wave can propagate in the ionosphere due to its long vertical wavelength (>50 km) ([FORBES, 2000](#)), it can transport energy and momentum from troposphere.

We have some possible scenarios for explaining the detection of planetary wave signatures in the ionosphere ([FORBES, 1996](#)) (also illustrated in [Figure 2.9](#)):

- stratospheric/mesospheric planetary waves could modulate the accessibility of gravity waves to the upper portion of the atmosphere, involving mechanisms that could lead to secondary sources of excitation of planetary waves in the upper atmosphere; and
- modulation by planetary waves of the upward propagating tides that participate in the dynamo action to generate electric fields in the upper regions.

The last mechanism seems to be promising and easier to verify since the forcing by diurnal and semidiurnal tides that propagates to top is basically responsible by the phenomenology of the ionosphere in quiet periods, especially in equatorial latitudes ([ABDU et al., 2006](#)).

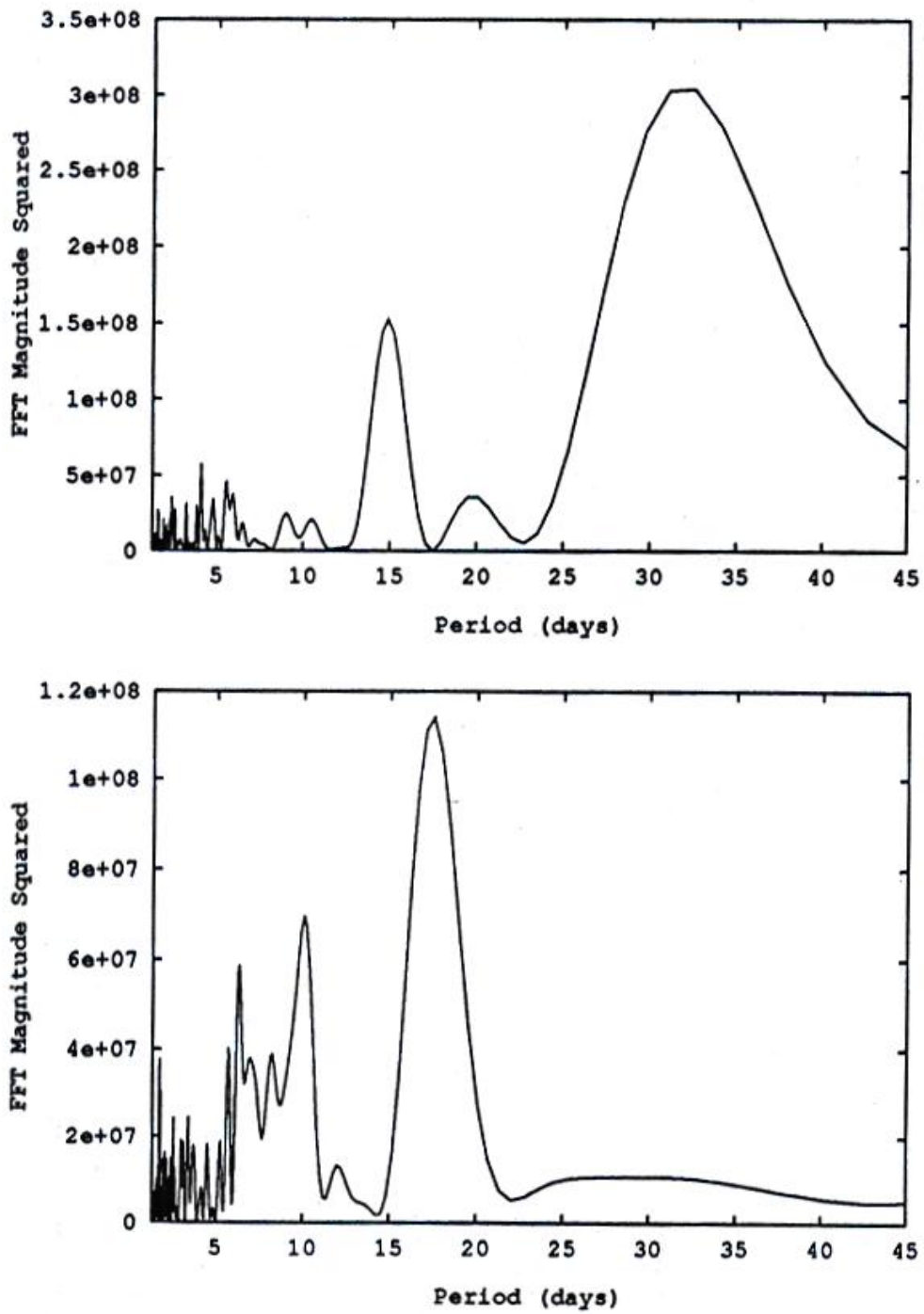


FIGURE 2.7 - Power Spectral Density as a function of period for ΔH for the interval January 1 to March 26 (upper panel), and August 15 to November 8 (bottom panel), in 1979.

SOURCE: [Parish et al. \(1994\)](#)

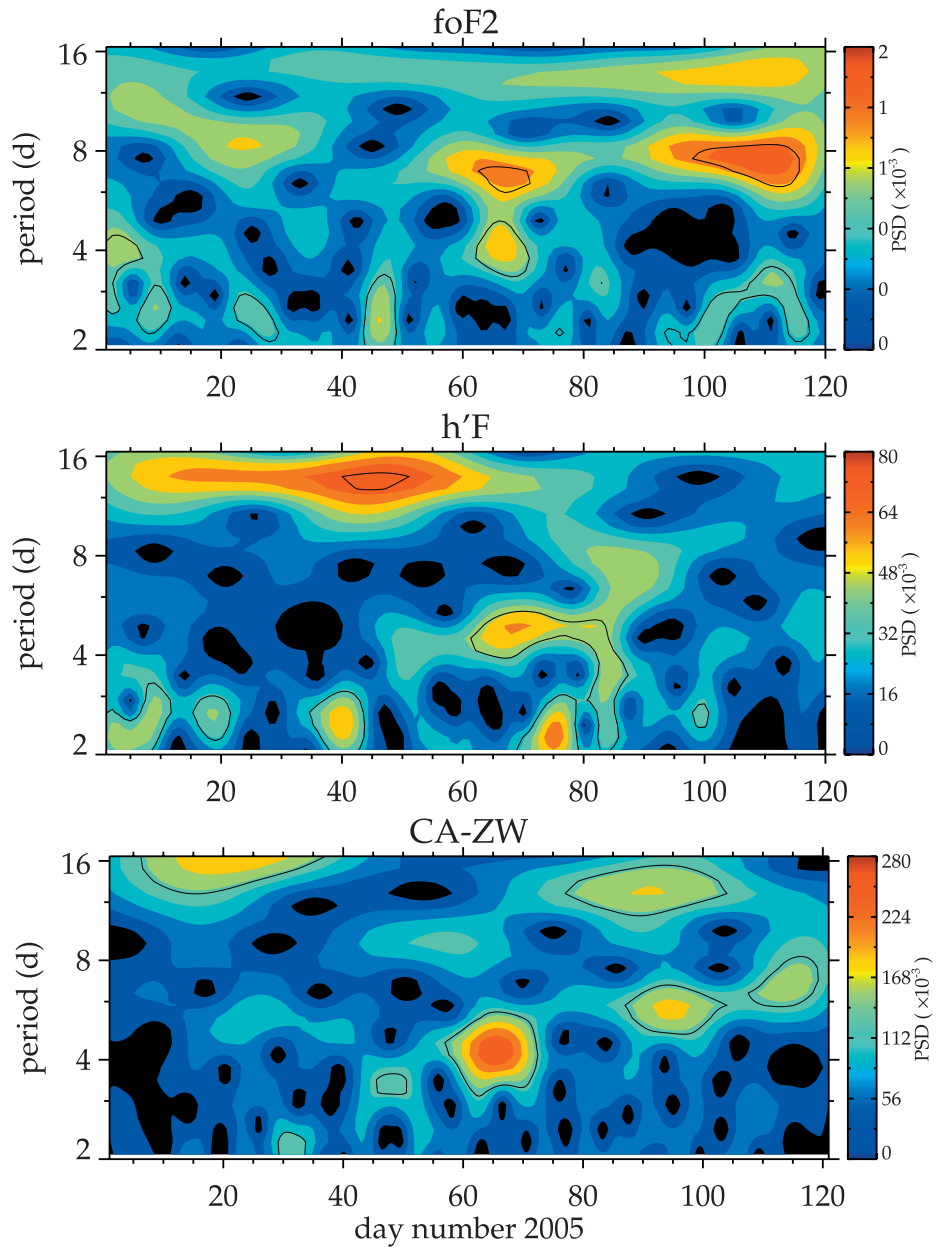


FIGURE 2.8 - Wavelet analysis of (top) ionospheric foF2, (middle) h'F observed at Fortaleza, and (bottom) mesospheric zonal wind at 90 km observed at Cariri during the period from January 1 to April 30, 2005.

SOURCE: [Takahashi et al. \(2007\)](#)

MECHANISMS FOR INDUCING PLANETARY-WAVE OSCILLATIONS IN THE MLT/DYNAMO REGIONS

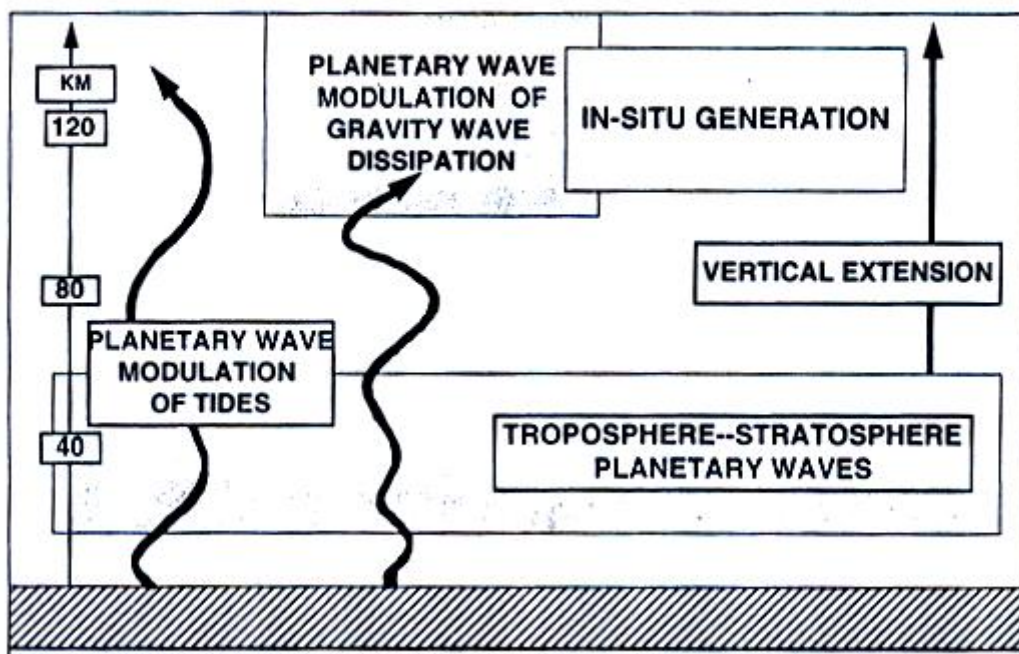


FIGURE 2.9 - Schematic illustrating possible mechanisms for inducing planetary wave oscillations in the mesosphere/lower thermosphere (MLT) and dynamo regions.

SOURCE: [Forbes \(1996\)](#)

3 INSTRUMENTATION AND DATA

The present study of electromagnetic signatures of gravity waves and 2-day planetary waves in the equatorial E-region has been developed based on coherent backscatter radar data, magnetometers data, and magnetic activity indices. In the following, it is described the main features of each one of them.

3.1 50 MHz Coherent Backscatter Radar - RESCO

In the Brazilian sector a 50 MHz coherent backscatter radar, also known by the acronym RESCO (in Portuguese, *Radar de ESpalhamento COerente*), has been operated since 1998 at São Luís, State of Maranhão (2.51° S, 44.27° W, mag. lat. -2.3°), near the dip equator. Observations of EEJ 3-m plasma irregularities are routinely carried out with the main purpose of studying the E-region dynamics through spectral analysis of the backscattered echoes from plasma instabilities and the other physical variables that can be achieved through them (ABDU et al., 2002; DENARDINI, 2003).

3.1.1 System Description

The RESCO radar system may be didactically divided into four parts: antenna array, transmitter, receiver, and signal control and data storage systems. A description of each part is given ahead. Some radar circuits are shared by both the transmitter and receiver systems, e.g., the oscillators, and they are described in the transmitter system only to avoid redundancy of information.

3.1.1.1 Antenna Array

The CoCo (coaxial-collinear) antenna array consists of 32 strings of 24 dipoles separated by a half wavelength, totalizing 768 dipoles (Figure 3.1). The array is configured so that the antenna beam can be steered electronically between the vertical and one oblique direction ($\pm 30^\circ$ zenith angle) or between the two oblique directions. Since the irregularities are preferably magnetic field aligned, the antenna strings are magnetic north-south aligned. The theoretical vertical beam width is $\sim 3.5^\circ$ in E-W and $\sim 6^\circ$ in N-S planes. The 32 strings consist of eight groups of four antennas each, being feed by eight transmitters. The total theoretical antenna gain is 32.5 dB. The east-west section of the RESCO antenna radiation pattern normalized to the peak is shown in Figure 3.2 for the three pointing directions. The upper panel

represents the westward beam tilted 30° from zenith angle. Middle panel gives the zenith beam representation. And the bottom panel gives the eastward beam tilted 30° from zenith.



FIGURE 3.1 - RESCO antenna array in the São Luís Space Observatory.

3.1.1.2 Transmitter System

The RESCO transmitter system is composed by a 30 MHz and a 80 MHz oscillator, two pulse formers, one mixer, one 80 MHz amplifier, one power splitter, eight phase-shifters, eight transmitters, and eight pre-amplifier duplexer modules. The transmitter peak power (sum of the eight transmitters power) is ~ 40 kW.

The output of each crystal oscillator (30 and 80 MHz) is connected to the pulse former and to the receiver. The two formers modulate the sinusoidal signals generated in the radar controller, each one having its own carrier. The 80 MHz and 30 MHz and outputs are mixed to result a composition of the sum (110 MHz) and the difference (50 MHz) of the input frequencies. In the 50 MHz intermediary frequency amplifier (IF), the carrier (50 MHz) is amplified, and the high frequency signal (110 MHz) is filtered. The IF output is then splitted in eight power balanced parts. Radar signal pulses act directly in the phase-shifters controlling the phase modification according to the scientific purposes of the radar soundings. The signal feeds the eight transmitters, where they are amplified and delivered to the antenna array through duplexer-pre-amplifier modules (also called T/R switches). These duplexers enable the use of the antenna array for transmission and reception. For a more complete explanation about the RESCO transmitter system, see [Janardhanan \(1983\)](#), or for

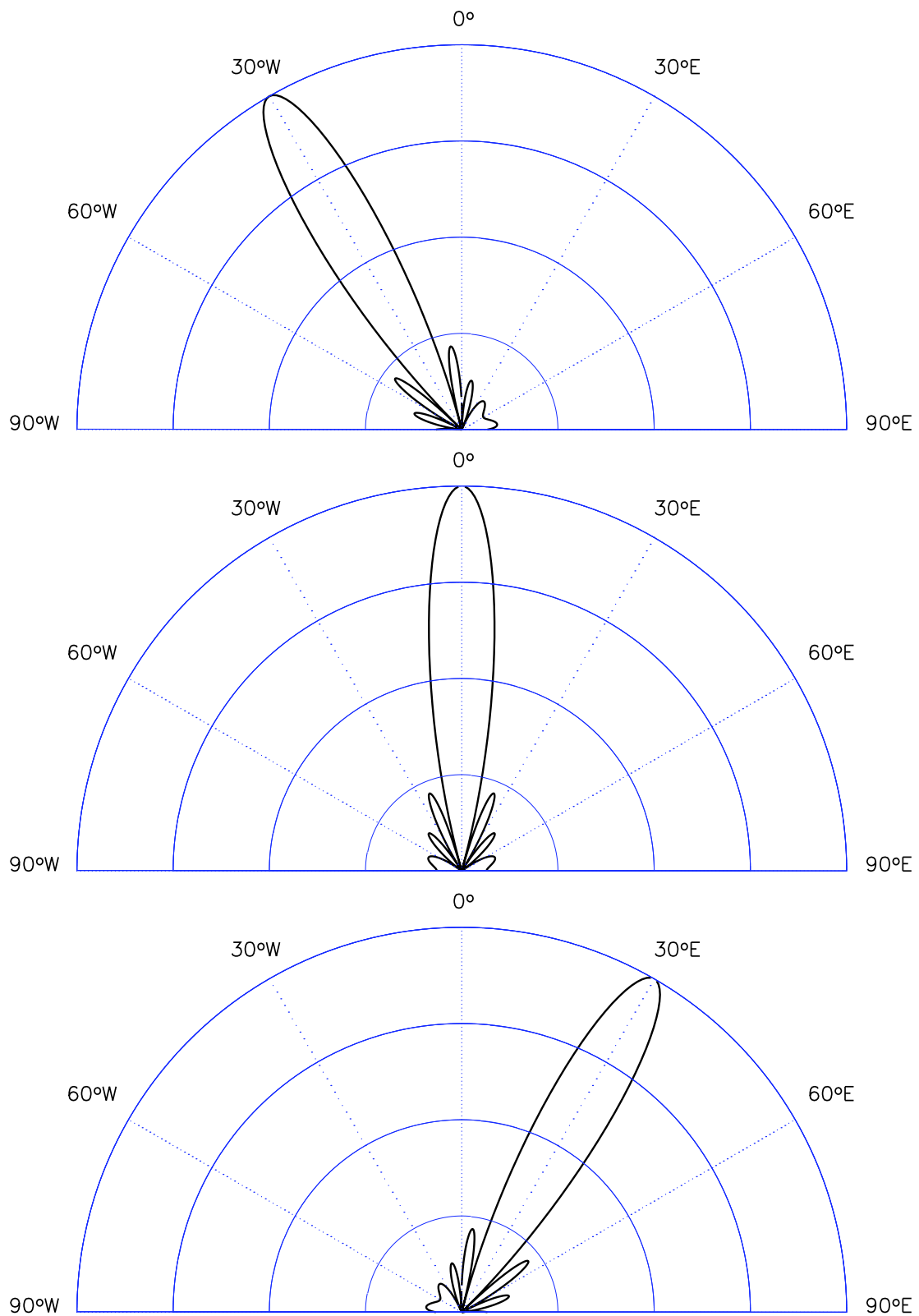


FIGURE 3.2 - East-west section of the RESCO antenna radiation pattern (32 strings of half wavelength dipoles) for the three operational modes: 30° west (upper panel), zenith (middle panel), and 30° east angle (bottom panel).

a comprehensive understanding of the system, see [Figure 3.3](#).

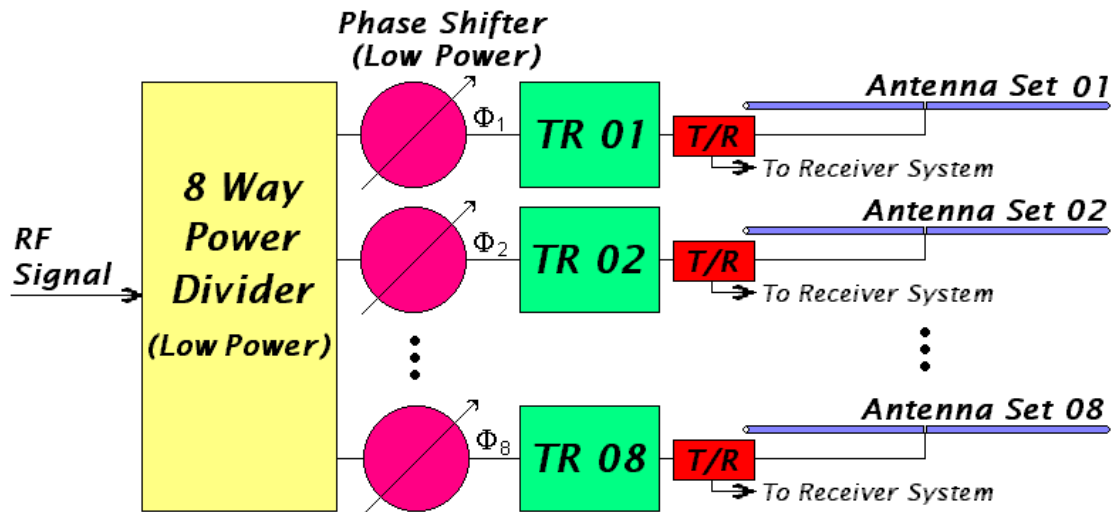


FIGURE 3.3 - Schematic diagram representing the eight transmitters with the power splitters and the phase-shifters of the RESCO radar system.

SOURCE: [Denardini \(1999\)](#)

3.1.1.3 Receiver System

The RESCO receiver system is composed basically by eight pre-amplifiers, eight phase-shifters, one power combiner and one phase detector circuit ([Figure 3.4](#)). When an echo is received by the antenna array, it is sent back to the radar through the eight duplexer pre-amplifier modules. Thereafter, the echo signal passes through the receiver circuit in the order we described above. Each of the eight parts of the echo signal is pre-amplified and the same phase-shift modifications imposed in the transmission are taken off. The echo signal are ready to be combined to one. The phase detectors amplify the signal, downconverting to 30 MHz, and divide into two equal parts. One of them is mixed with the pure 30 MHz oscillator signal, and the other one is mixed with the same signal electrically delayed in 90° . The resulting signals are an in-phase and quadrature signals, carrying informations about the plasma irregularities in the line-of-sight of the radar.

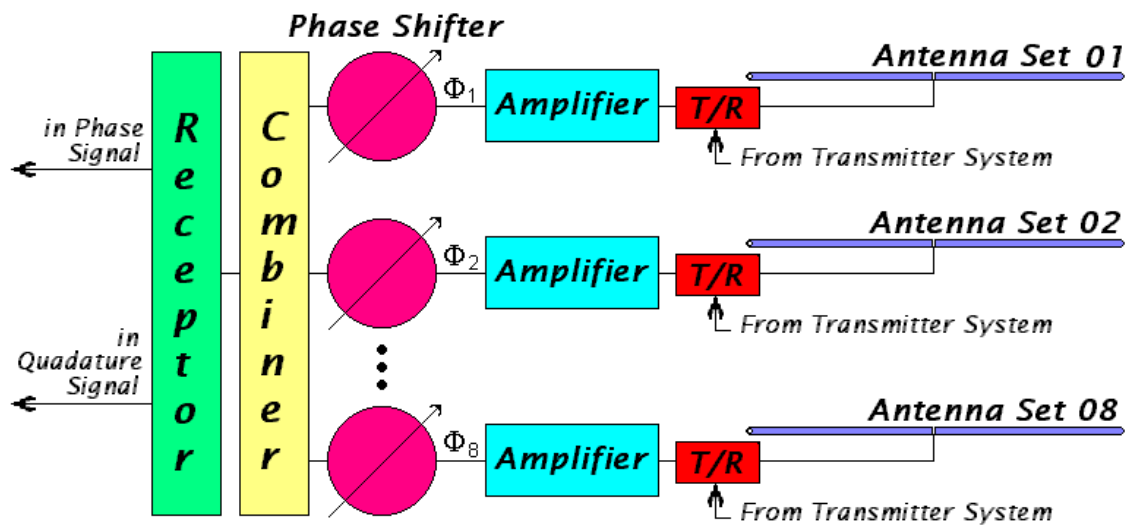


FIGURE 3.4 - Schematic diagram representing the duplexers, phase-shifters and power combiners of the RESCO radar system.

SOURCE: Denardini (1999)

3.1.1.4 Signal Control and Data Storage System

The RESCO signal control system is responsible for generating the pulse that controls the transmission, reception, and data acquisition, and the pulses that switches the antenna pointing direction. The variables controlled during the transmission are the pulse width (between 20 and 100 μ s), the interpulse period (from 1 to 20 ms), and the number of pulses per packet. The variables controlled during reception, are attenuation (in dB), time delay between transmission and reception (usually 600 ms), and number of range gate samples (usually 16).

The data storage unit is composed by an interface circuit and a computer dedicated to data storage. A 16-bit analog to digital converter board store the two channels (in-phase and quadrature signals) in a sequential binary file, where the signals are grouped in sets for each sampled range gate.

3.1.2 Radar Data Processing

The data processing consisted in an offline spectral analysis using Fast Fourier Transform (FFT) for each range gate. So, the spectral distribution of the Doppler frequencies contained in the returned signal can be obtained, as shown in Figure 3.5. The

Doppler spectrum of the echoes is composed by both Type I and Type II irregularities embedded in the plasma volume enlightened by the radar beam.

Assuming that the experimental spectra can be decomposed in many Gaussians as stated by [Cohen \(1973\)](#), a spectral decomposition technique can be applied. In the present case, it involves fitting the sum of two Gaussians to the spectrum, which is described by a S distribution in function of the frequency, given by

$$S(f) = \frac{P_I}{\sigma_I\sqrt{2\pi}} \exp\left[-\frac{(f - f_{dI})^2}{2\sigma_I^2}\right] + \frac{P_{II}}{\sigma_{II}\sqrt{2\pi}} \exp\left[-\frac{(f - f_{dII})^2}{2\sigma_{II}^2}\right] + P_N, \quad (3.1)$$

where P_N , $P_{I,II}$, $\sigma_{I,II}$, and $f_{d(I,II)}$ are, respectively, the power level of the noise, spectral power, spectral width, and Doppler frequency, and the subscript indicates the irregularity type: Type I (I) or Type II (II). The Maximum Likelihood Estimate (MLE) has been used for nonlinear fitting of the 7 parameters of each spectrum, $\mathbf{a} = \{f_{dI}, f_{dII}, \sigma_I, \sigma_{II}, P_I, P_{II}, P_N\}$. The fitting method is based on finding the parameters \mathbf{a} that maximize the probability function $P(y_1 \cdots y_n | \mathbf{a})$ of obtaining the data set $\mathbf{y} = \{y_1 \cdots y_n\}$ ([BARD, 1974](#); [PRESS et al., 1992](#)). In other words, it is a problem of finding the parameters \mathbf{a} that minimize the square sum of residual errors between the observational data set \mathbf{y} and the corresponding Gaussians $S(f)$ that describes the data set, considering the uncertainty σ_i related to each point y_i . [Equation 3.2](#), named objective function, describes mathematically the above statement.

$$\chi^2 \equiv \sum_{i=1}^N \frac{[y_i - S(f_i; P_I, f_{dI}, \sigma_{II}, P_{II}, f_{dII}, \sigma_{II}, P_N)]^2}{\sigma_i}, \quad (3.2)$$

where N is the number of frequencies in the power spectrum, y_i is the observed spectral amplitude for a given frequency and all the other parameters have been introduced before.

An example of simulated spectra with two Gaussians (similar to those obtained by RESCO radar data) and the fitted $S(f)$ is shown in [Figure 3.6](#). It can be seen that the parameter estimation returns a well fitted curve. It means that the data informations are retrieved with success.

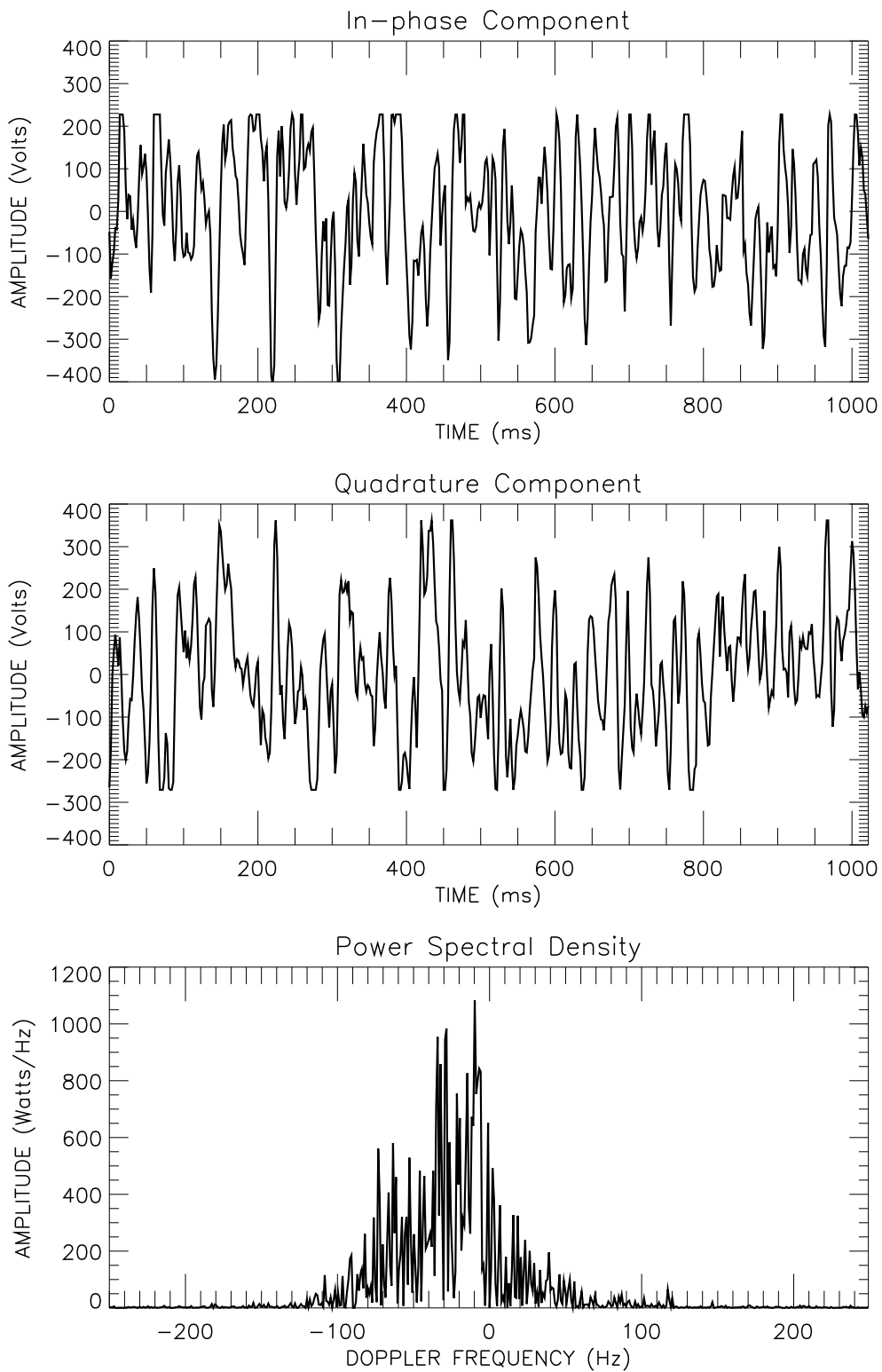


FIGURE 3.5 - In-phase and quadrature components, and the respective power spectral density. The data set corresponds to 102.60 km height at 16h01 LT in February 15, 2002 obtained by the RESCO radar westward beam.

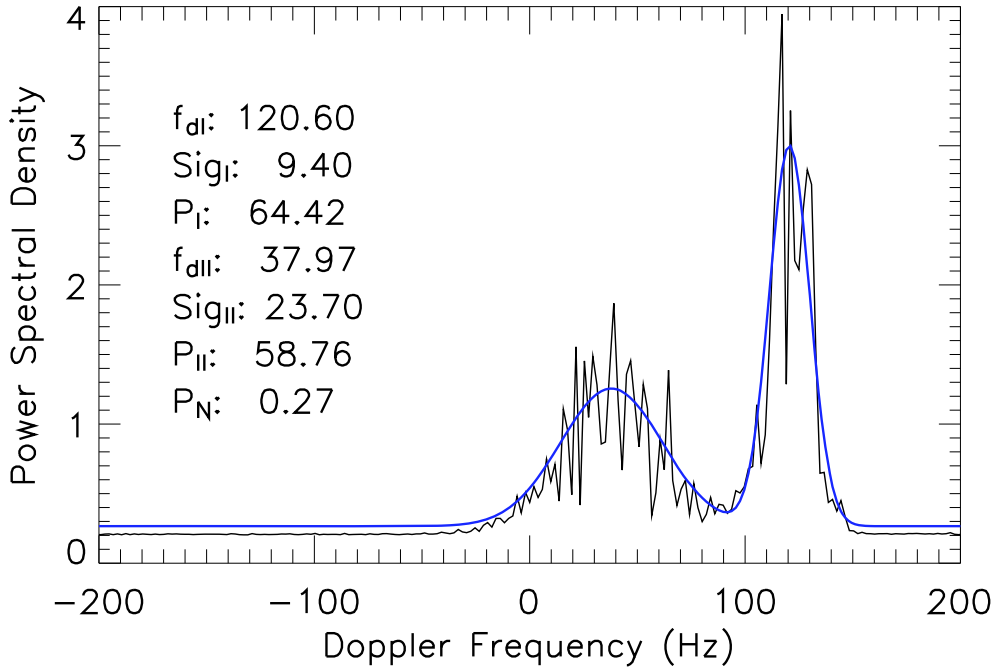


FIGURE 3.6 - Simulated power spectrum (black) and the fitted Gaussian curves (blue).

3.1.2.1 Example of RESCO Data Processing

Since the RESCO radar data was applied in this work, an example of data processing is given below. Applying an interpulse period (IPP) of transmission to 1 ms; a time delay (TD) between transmission and acquisition to 620 μs , which corresponds to the minimum height sampled to be 80.5 km; a pulse width (PW) of 20 μs , that corresponds to 2.6 km height resolution using the oblique radar beam. The radar data acquisition system samples the echoes so that the height coverage is between around 80 and 120 km, divided in 16 range gate samples. The echo signals (received from the EEJ irregularities) are grouped in sets corresponding to 256 pulses (NP) for each sampled range gate. The data processing consisted in an offline spectral analysis using Fast Fourier Transform (FFT) for each range gate of NP data points which resulted in the spectral distribution of the Doppler frequencies contained in the returned signal for each range gate. If the time resolution between each set of NP pulses is 12 s, the aliasing frequency for each spectrum will be 500 Hz with ~ 4 Hz (NP=256) of frequency resolution. As mentioned before, applying curve fitting to the spectrum it is possible to infer the irregularity parameters. If there are no irregularity present in the observed bulk, the radar does not receive any echo from the EEJ heights ($\sim 80\text{-}120$ km); so, there is as an absence of Gaussians in the radar

spectrum. Therefore, if the Type II echoes are present, it is possible to determine the evolution of its velocity in time and height (inside the observed bulk) for the whole day of the radar operation.

3.2 Geomagnetic Components and Magnetometer

The terrestrial magnetic field components are preferably measured in one of two ways XYZ or HDZ , respectively (CAMPBELL, 1997) (Figure 3.7):

- three orthogonal component field directions with positive values for geographic northward (X), eastward (Y), and vertical into the Earth (Z , negative values for the opposite directions); or
- the horizontal magnitude (H), the eastward angular deviation of the magnetic horizontal component from geographic northward (D), and the downward vertical component (Z).

From Figure 3.7, it can be seen that

$$H = \sqrt{X^2 + Y^2}, \text{ and } D = \arctan\left(\frac{Y}{X}\right), \quad (3.3)$$

or, equivalently

$$X = H \cos(D), \text{ and } Y = H \sin(D). \quad (3.4)$$

Also, there are other two magnetic parameters that are commonly mentioned in the text: the magnetic inclination, or dip angle (I), and the dip latitude (λ). They are given by

$$I = \arctan\left(\frac{Z}{H}\right), \text{ and } \lambda = \arctan\left(\frac{1}{2} \cdot \tan I\right). \quad (3.5)$$

Magnetometers are electronic devices that allow measurements of some the above mentioned parameters. These equipments can be found in the ground-based style (worldwide installed) or flight mode style (normally used in satellites or rockets). They also have different versions, having their own characteristics and applications, such as the optical Zeeman, the classical variometer, the fluxgate, the SQUID and the proton magnetometer.

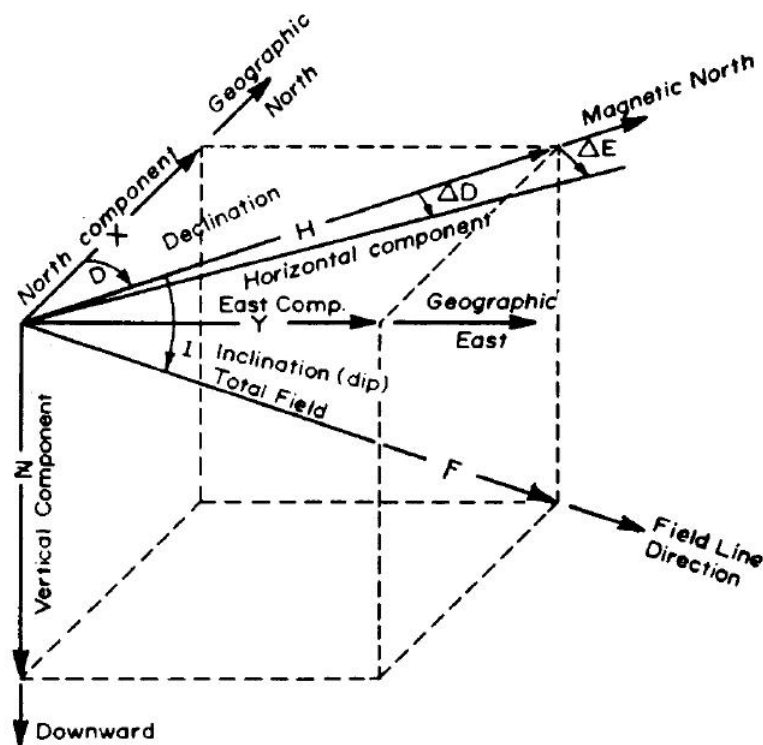


FIGURE 3.7 - Components of the geomagnetic field measurements for a sample Northern Hemisphere total field vector F inclined into the Earth. An explanation of the letters and symbols is given in the text.

SOURCE: [Campbell \(1997\)](#)

Since the fluxgate magnetometers use a well-known technology and are cheaper compared to the others, they are preferably used in many magnetic stations. This type of magnetometer is composed of a probe or sensor coupled to a processing electronics circuit. The probe sensor coil, whose core is of a soft ferromagnetic material, has in its simplest version two windings, an excitation coil and a pick-up coil. The processing electronics must supply an excitation current to the premagnetization coil and perform the pick-up's signal processing (see, for example, [Cruz e Trujillo \(1999\)](#)). The magnetic field intensity is obtained by the generation of harmonic distortions in the output field, measured by secondary loops over the nucleus ([CAMPBELL, 1997](#)).

3.2.1 Measuring Ionospheric Current Signatures at Ground

Measurements of the Earth's magnetic field components have been made over the years at the ground level. The daily variation of the H-component in relation to its midnight value ($dH = H - H_0$) at magnetic equatorial latitudes may be used as a

proxy of the equatorial electrojet currents. dH observed at a point on the ground is not only due to the overhead currents, but also due to the currents flowing over a latitudinal extent of a few degrees on either side of the overhead point (VIKRAMKUMAR et al., 1987). Also, the observed dH variations at ground levels consists: one due to currents in the EEJ itself (dH_{ext}), and other due to currents induced by the electrojet in the earth (dH_{int}). Since latitudinal distribution of the height-integrated current intensity in the EEJ (J) shows a maximum in magnetic equator and a sharp decay off-equator, and assuming a ribbon-like current flow, the ground level perturbations dH_{ext} is related to the EEJ current as per (VIKRAMKUMAR et al., 1987):

$$dH_{ext} = \frac{h_0\mu_0}{2\pi} \int_{-10}^{+10} \frac{J(\lambda)d\lambda}{h_0^2 + x^2(\lambda)}, \quad (3.6)$$

where h_0 is the mean electrojet height, x is the distance of the latitudinal element $d\lambda$ from the geomagnetic equator and μ_0 is the permittivity of free-space. J is integrated between $\pm 10^\circ$ geomagnetic latitude because the current contribution to J is almost negligible beyond this range (VIKRAMKUMAR et al., 1987).

Magnetometer data is provided by World Data Center for Geomagnetism - Kyoto in *HDZ* or *XYZ* format. It was developed an automatic procedure (program) in IDL Language to calculate the power spectra for the proxy equatorial electrojet current based on magnetic field variations. Figure 3.8 shows a flowchart of the program.

The program is basically divided into four blocks:

- Manual Input - the variable inputs are chosen: (a) the magnetometer station code (e.g., SLZ, that is the São Luís station), (b) the magnetic component to be analyzed (X, Y, H, D, Z), (c) the daily range (e.g., from January 15 to February 20, 2003), and the periodicity range (e.g., from 0.5- to 16.0-days);
- Load the magnetometer data, and the station informations (such as latitude, and longitude);
- Calculate the Time Zone of the magnetometer station, and remove the midnight component value from the time series for each day (e.g., $dH=H-H_0$, if H was the chosen component); and

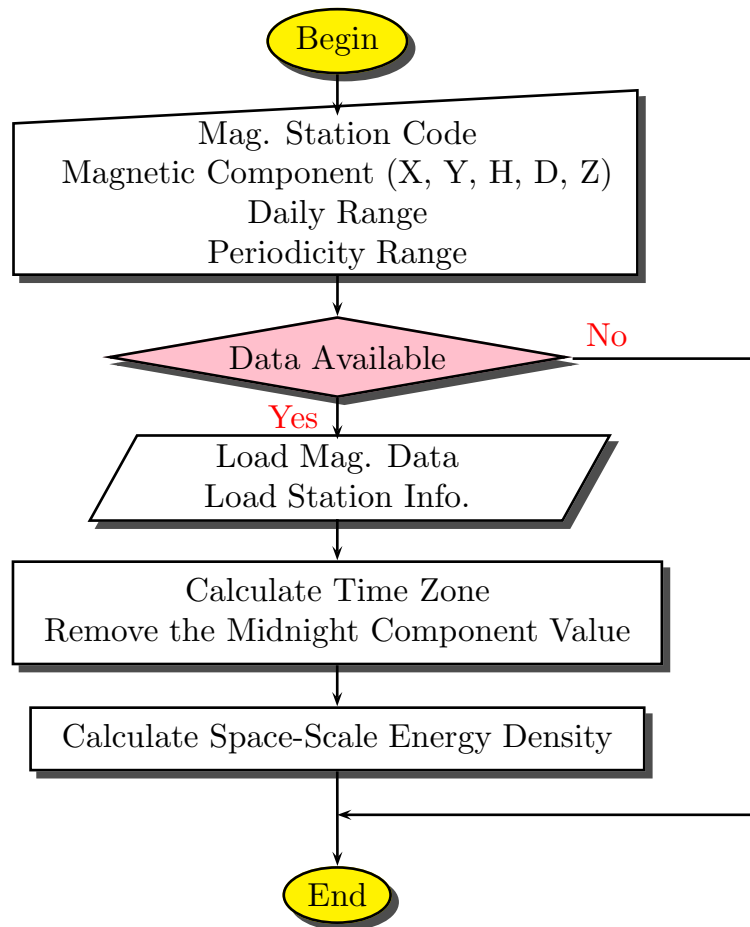


FIGURE 3.8 - Flowchart of the program that calculates the Space-Scale Energy Density using the Morlet Wavelet-Mother from magnetometer data.

- Calculate the Space-Scale Energy Density of the time series (see [subsection 3.4.1](#) for a more comprehensive explanation), plot and save it.

3.3 Magnetic Activity Indices

The geomagnetic activity, including variations caused by solar activity in the magnetic field, is carefully monitored by instruments in the ground or in the space. Using measurements from such instruments, the magnetic activity indices are calculated, which quantifies the geomagnetic conditions, making possible the analysis of quiet and disturbed periods. Among these indices, we present six of them: Kp, Dst, AU, AL, AO and AE.

3.3.1 Kp Index

The K-index is a quasi-logarithmic local index of the 3-hourly range in magnetic activity relative to an assumed quiet-day curve for a single geomagnetic observatory site. The planetary 3-hour-range index Kp is the mean standardized K-index from 13 geomagnetic observatories between 44° and 60° northern or southern geomagnetic latitude. Since it is a 3-hour-range index, a full day has eight Kp values (0-3h, 3-6h, 6-9h, 9-12h, 12-15h, 15-18h, 18-21h, and 21-24h). Kp varies from 0 to 9, subdivided into third levels, resulting in 28 values: 0o, 0+, 1-, 1o, 1+, 2-, 2o, 2+, ..., 8o, 8+, 9-, and 9o. Kp=4o is the reference value that separates quiet conditions (Kp<4o) from the disturbed one (Kp>4o) (ROSTOKER, 1972). The Kp index for October 2003 is presented in Figure 3.9, where it may be noted that around 29 October a magnetic storm starts, lasting approximately 3 days.

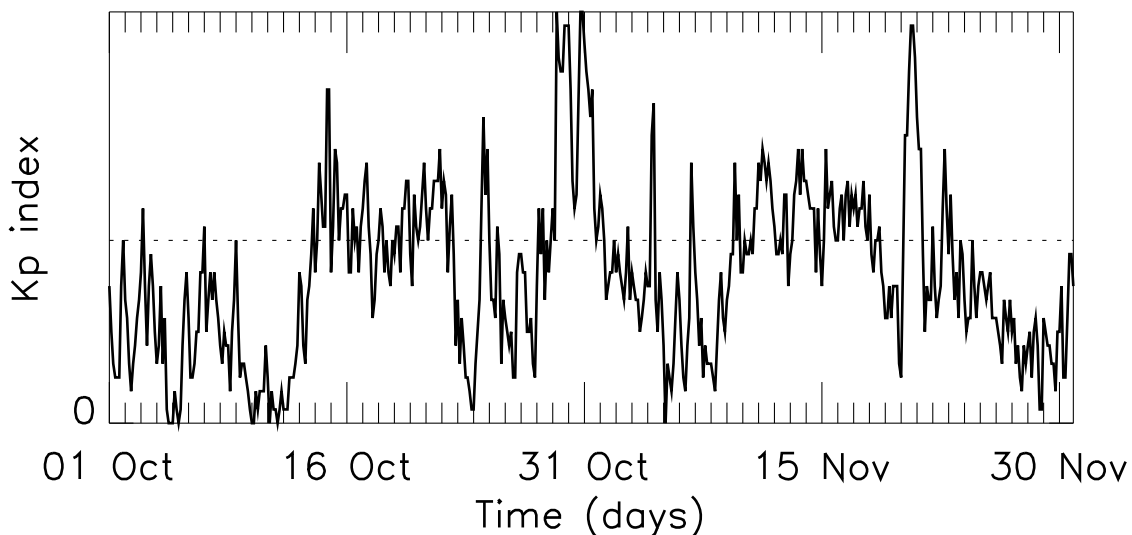


FIGURE 3.9 - Kp index for October 2003.

3.3.2 Dst Index

The Dst index was developed aiming to give an indication of ring current strength. This index, as an indicator of the strength of large-scale current systems, does not describe the level of localized auroral electrojet activity. Thus it can not be used to identify individual substorm events (ROSTOKER, 1972). It is built by averaging the horizontal component of the geomagnetic field from mid-latitude and equatorial

magnetograms from all over the world. According to [Gonzalez et al. \(1999\)](#), the Dst index can be separated in four different levels: Intense ($\text{Dst} < -100 \text{ nT}$), Moderate ($-100 \text{ nT} \leq \text{Dst} < -50 \text{ nT}$), Small ($-50 \text{ nT} \leq \text{Dst} < -30 \text{ nT}$), and Negligible storm activity ($-30 \text{ nT} \leq \text{Dst}$). The different phases of the magnetic storm can be analyzed in the Dst index, as described below (see [Figure 3.10](#)):

- Sudden Commencement (SC) - briefly before a magnetic storm event occurs, the Dst index may present a sudden rise. The SC is not observed at all storms;
- Main Phase - the index intensity shows a sharply decrease; and
- Recovery Phase - after the decaying phase, the index starts to rise up until the quiescent value observed prior to the storm.

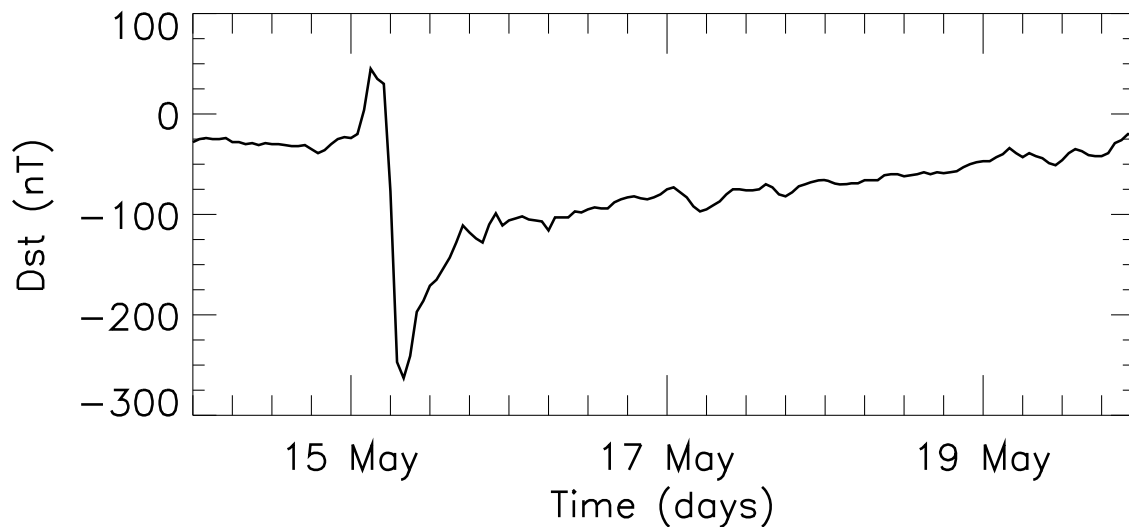


FIGURE 3.10 - Dst index for May 2005.

3.3.3 Auroral Indices

There are four auroral indices: AE, AO, AU, and AL. Auroral electrojet indices are designed to measure the auroral zone magnetic activity produced by enhanced ionospheric currents flowing below and within the auroral ovalis. The AU is defined as the upper magnetic envelope of the superimposed geomagnetic data and gives

a good representation of the maximum magnetic perturbation generated by the eastward electrojet usually found in the afternoon sector. Similarly, AL is defined as the lower envelope and represents the maximum magnetic perturbation generated by the westward electrojet in the morning and midnight sectors (ROSTOKER, 1972). The AE index is mathematically defined as the difference between AU and AL indices (i.e., $AE=AU-AL$). The mean value of the AU and AL (i.e., $(AU+AL)/2$), defines the AO index. Thus, the AE index represents the overall activity of the electrojets, and the AO index provides a measure of the equivalent zonal current. Figure 3.11 shows the auroral indices for October 2003 (the same period provided in Figure 3.9).

3.4 Spectral Analysis Techniques

3.4.1 Continuous Wavelet Transform and the Morlet Wavelet-Mother

The wave-type oscillations were analyzed through spectral analysis of the magnetometer data using the wavelet transform. The wavelet-mother choose for the present work was Morlet, which is a plane wave modulated by a Gaussian envelope of unit width (FARGE, 1992). The continuous wavelet transform (CWT) of a discrete sequence x_n is defined as the convolution of x_n with a scaled and translated version of the wavelet-mother or, alternatively, by the convolution theorem, i.e., the inverse Fourier transform of the product in the frequency domain, as given by (TORRENCE; COMPO, 1998):

$$W_n(s) = \left(\frac{2\pi s}{\delta t} \right) \cdot \sum_{k=0}^{N-1} \hat{x}_k \hat{\psi}_0^*(s\omega_k) \exp(i\omega_k n \delta t), \quad (3.7)$$

where s is the wavelet scale, k is the frequency index, δt is the time resolution, N is the total number of points, \hat{x} is the Fourier transform of the time series, $\hat{\psi}_0^*(s\omega_k)$ is the complex conjugate of the wavelet-mother, and the angular frequency is defined as

$$\omega_k = \begin{cases} +\frac{2\pi k}{N\delta t} & : k \leq N/2 \\ -\frac{2\pi k}{N\delta t} & : k > N/2 \end{cases} . \quad (3.8)$$

The Morlet wavelet-mother is defined as (TORRENCE; COMPO, 1998):

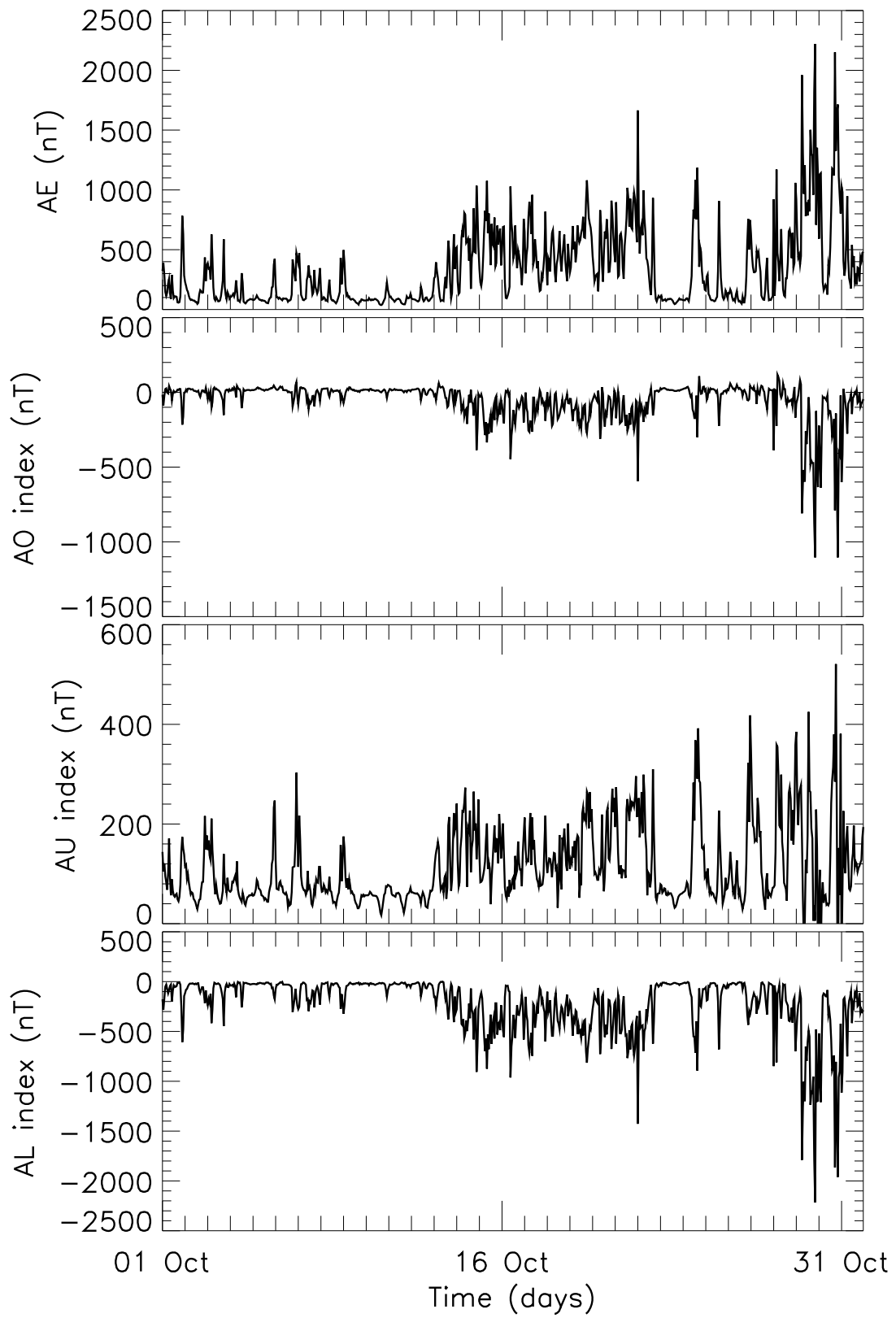


FIGURE 3.11 - Auroral indices for October 2003.

$$\hat{\psi}_0(s\omega_k) = \pi^{-1/4} H(\omega) \exp \left[-\frac{(s\omega - \omega_0)^2}{2} \right], \quad (3.9)$$

where $H(\omega)$ is the Heaviside step function ($H(\omega) = 1$ if $\omega > 0$, $H(\omega) = 0$ otherwise) and ω_0 is the frequency. The total energy is conserved under the wavelet transform, and the space-scale energy density for 1-D time series is defined as (FARGE, 1992):

$$E_n(s) = \frac{|W_n(s)|^2}{s}. \quad (3.10)$$

And the reconstructed time series is just the sum of the real part of the wavelet transform over all scales:

$$x_n = \frac{\delta j \delta t^{1/2}}{C_\delta \psi_0(0)} \sum_{j=0}^J \frac{\{W_n(s_j)\}}{s_j^{1/2}}, \quad (3.11)$$

where C_δ is the reconstruction factor (=0.776 for Morlet). The factor $\psi_0(0)$ removes the energy scaling (= $\pi^{-1/4}$ for Morlet), while the $s_j^{1/2}$ converts the wavelet transform to an energy density.

Finally, attention should be paid to problems related to data gaps and edge effects. These problems are known as cone of influence (COI) effects. The COI is the region of the wavelet spectrum in which edge effects become important and was defined here as the e-folding time for the autocorrelation of wavelet power at each scale. This e-folding time is chosen so that the wavelet power for a discontinuity at the edge drops by a factor e^2 and ensures that the edge effects are negligible beyond this point (TORRENCE; COMPO, 1998).

3.4.2 Lomb-Scargle Periodogram

The Lomb-Scargle is an algorithm used for extracting frequency components of unevenly sampled signals or time series with gaps (LOMB, 1976; SCARGLE, 1982). Let's define a physical variable X measured at a set of times t_i . The resulting time series data, $\{X(t_i), i=1,2,\dots, N_0\}$, are assumed to be the sum of a signal and random observational errors:

$$X_i = X(t_i) = X_S(t_i) + R(t_i). \quad (3.12)$$

Let's assume that the noise at different times are independent; that is, $R(t_i)$ is

statistically independent of $R(t_j)$ for i not equal to j . We also assume that $R(t_i)$ is normally distributed with zero mean and a constant variance, σ_0^2 . A new definition of the periodogram is given by (SCARGLE, 1982):

$$P_X(\omega) = \frac{1}{2} \left\{ \frac{\left[\sum_j X_j \cos \omega(t_j - \tau) \right]^2}{\sum_j \cos^2 \omega(t_j - \tau)} + \frac{\left[\sum_j X_j \sin \omega(t_j - \tau) \right]^2}{\sum_j \sin^2 \omega(t_j - \tau)} \right\}, \quad (3.13)$$

where τ is defined by

$$\tan(2\omega\tau) = \frac{\sum_j \sin 2\omega t_j}{\sum_j \cos 2\omega t_j}. \quad (3.14)$$

Equation 3.13 has a simple statistical behavior, and is equivalent to the reduction of the sum of squares in least-squares fitting of sine waves to the data (SCARGLE, 1982). The threshold level that the power should exceed to be claimed as signal detection is given by:

$$z_0 = -\ln[1 - (1 - p_0)^{1/N_i}], \quad (3.15)$$

where p_0 is the false alarm probability ($0 \leq p_0 \leq 1$), that can be interpreted as the complement of the confidence limit, and N_i is the number of frequencies searched for the maximum, deduced by Horne e Baliunas (1986), as given by:

$$N_i = -6.362 + 1.193N_0 + 0.00098N_0^2, \quad (3.16)$$

Finally, the normalized periodogram is defined as:

$$P_N(\omega) = P_X(\omega)/\sigma_0^2. \quad (3.17)$$

4 CLIMATOLOGY OF GRAVITY WAVES-INDUCED ELECTRIC FIELDS

Equatorial electrojet (EEJ) observations using VHF radars show backscattered echoes from two types of electron density irregularities explained by the modified two-stream (Type I) and the gradient drift (Type II) instabilities. From the Type II irregularity velocities obtained by radar data we have inferred the vertical electric fields (E_z). In addition, the E_z inference uses geomagnetic field and atmospheric models. The harmonic analysis of such fields shows the presence of gravity waves-induced electric fields in the EEJ. We calculated the ratio between GW-related electric fields and the total E_z . This factor is an indicator of the efficiency in the production of an additional electric field due to a gravity wave neutral wind. In the present work we summarize some characteristics of the gravity waves that could modify the equatorial ionospheric electric fields and discuss the methodology of analysis.

4.1 Experimental Description

For such study we have used the RESCO radar set for EEJ soundings. The interpulse period (IPP) of transmission is usually set to 1 ms. The time delay (TD) between transmission and acquisition is set to 620 μ s, which corresponds to the minimum height sampled to be 80.5 km. The observations have been made using a pulse width (PW) of 20 μ s that corresponds to 3 km height resolutions using the vertical beam or 2.6 km when the radar beam is oblique. The radar data acquisition system samples the echoes so that the height coverage is between around 80 and 120 km, divided in 16 range gate samples, that are stored in a sequential binary file. The signals are grouped in sets corresponding to 256 pulses (NP) for each sampled range gate. The data processing consisted in an offline spectral analysis using Fast Fourier Transform (FFT) for each range gate of NP data points which resulted in the spectral distribution of the Doppler frequencies contained in the returned signal for each range gate. For the periods of analysis, the time resolution between each set of NP pulses is 12 s and the aliasing frequency for each spectrum is 500 Hz with ~ 4 Hz (NP=256) of frequency resolution. By integrating incoherently in time 10 subsequent spectra, it was obtained an averaged 2-minute resolution spectrum per range gate.

The Doppler spectrum of the echoes is a composite of both Type I and Type II irregularities present inside the volume sampled by the radar. Therefore, the Gaussian

fit technique mentioned in [subsection 3.1.2](#) was applied to each spectrum. Thus, each Gaussian (related to one specific irregularity type) is characterized by three parameters: center of frequency distribution (corresponding to Doppler shift), spectral power density, and spectral width. After inverting the curves, the six statistical moments (three to each irregularity type) are evaluated. Fitted curves with spectral power smaller than 5% of the maximum spectral power for the whole day are discarded to avoid eventual bad fitting related-problems. Finally, the phase velocity estimates for Type II irregularities (V_{pII}) which was obtained by fitting, is used to calculate the vertical electric field (E_z) by:

$$E_z = V_{pII}(1 + \psi) \cdot \frac{B^2}{H}, \quad (4.1)$$

where H is the horizontal component of the magnetic flux density \mathbf{B} , and B is defined as $|\mathbf{B}|$. Since only waves propagating normal to the field are analyzed, we can simplify ψ (from [Equation 1.10](#)) to:

$$\psi = \frac{\nu_e \cdot \nu_i}{\Omega_e \cdot \Omega_i}. \quad (4.2)$$

In the computation of ψ , we neglected the ion-electron collisions, and the ion-neutral collision frequency were calculated using [Kelley \(1989\)](#):

$$\nu_{in} = (2.6 \times 10^{-9}) \cdot (N_n + N_i) \cdot (A_n + A_i)^{-1/2}, \quad (4.3)$$

where $N_{n,i}$ is the density and $A_{n,i}$ is the average molecular weight, respectively. The subscript n indicates the neutral terms. We neglect the ion terms, so $N_n + N_i \approx N_n$ and $A_n + A_i \approx A_n$. Since the electron-ion collisions are negligible in the lower E-region ([FORBES, 1981](#)), the electron collision frequency is approximated by the electron-neutral collisions, as given by ([KELLEY, 1989](#)):

$$\nu_{en} = (5.4 \times 10^{-10}) \cdot N_n \cdot T_e^{1/2}, \quad (4.4)$$

where T_e is the electron temperature. In the work, we assumed isothermal electron with $T_e=T_n$, but is not necessarily a good assumption ([OYAMA et al., 1980](#)). T_e , basically, should be equal to T_n , however, the few reports of electron temperature observations show that very often T_e is higher than T_n ([OYAMA, 2000](#), and refer-

ences therein). For example, in the equatorial electrojet region, electron temperature measurement were only once reported by [Sampath et al. \(1974\)](#) and showed that T_e would be approximately twice the T_n obtained by models. Based on that, the isothermal electron assumption may lead to an underestimation of the vertical electric field by $\sim 8\%$.

The gyrofrequencies were calculated, given by:

$$\Omega_{e,i} = \frac{q_{e,i} \cdot B}{m_{e,i}}, \quad (4.5)$$

where $m_{e,i}$ is the mass average, and $q_{e,i}$ is the electrical charge. The parameters used to perform the calculations of ψ were obtained from [Banks e Kockarts \(1973\)](#), International Reference Ionosphere (IRI) Model ([BILITZA, 2001](#)), and International Geomagnetic Reference Field (IGRF) Model ([MACMILLAN; MAUS, 2005](#)).

4.2 Efficiency of GW-Induced Electric Fields

The analysis was performed using data collected from the eastward radar beam during some magnetically quiet days ($Kp \leq 3+$) in 2001, 2002, and 2004. Disturbed days were discarded so that amplitude oscillations in electric fields would be mainly caused by atmospheric waves. The steps to calculate the GW-induced electric fields efficiency (R_{GW}) factor using wavelet transform are:

- apply CWT ([Equation 3.7](#)) using the wavelet-mother of Morlet ([Equation 3.9](#)) to vertical electric fields;
- reconstruct the electric fields ([Equation 3.11](#)) over scales in the range from 4- to 30-minutes (short-period gravity waves); and
- calculates the ratio between the total electric fields (original time series) and the reconstructed (sinusoidal waves-) electric fields, i.e., the estimated R_{GW} factor.

The analysis was constrained to the 100-110 km height, where the backscatter EEJ power is stronger. Based on the RESCO radar parameters applied to the EEJ sounding, it resulted in a vertical electric field with 3 points in height with 2-minutes resolution. The height median of the vertical electric field, filtered field, filtered wave

amplitude, and efficiency factor is calculated. An example of these parameters for February 6, 2001 is shown in [Figure 4.1](#).

Further, to examine the seasonal variation of the R factor, the data were grouped into the following Lloyd season classification: (1) D-months consisting of November, December, January and February representing local summer season; (2) E-months consisting of March, April, September and October; and (3) J-months consisting of May and June, July and August months representing local winter season. We have selected 51 days on J-, 50 from E-, and 79 on D-months.

[Figure 4.2](#) shows the statistics of vertical electric field (E_z) binned in 30-min intervals and 0.5 mV/m for (upper panel) solstice D months, (middle panel) equinoctial E months, and (lower panel) solstice J months. The sum of each vertical line gives 100% of occurrences. The continuous line represents the average vertical electric field for each 30-min interval and the vertical line is the standard deviation of E_z . The results shows that the vertical electric fields on D months in general does not grow up to 5 mV/m. The average E_z for D season during diurnal period varies from 3 mV/m (at 8h LT) to 2 mV/m (at 18 h LT). The average vertical electric field for both E and J seasons shows a variation from around 4 mV/m to 3 mV/m. So, it seems that the vertical electric fields are weaker in summer months. In general, E_z in J months is stronger than in the others. The standard deviation shows also that the vertical electric fields presents a major variability in winter than in other seasons.

The vertical electric field perturbations produced by gravity wave winds ($E_{z(GW)}$) is obtained as described before. The statistics of $E_{z(GW)}$ amplitude as function of time for (upper panel) solstice D months, (middle panel) equinoctial E months, and (lower panel) solstice J months, is shown in [Figure 4.3](#). The vertical and horizontal lines have the same meaning as in [Figure 4.2](#), and the bins have the same width. $E_{z(GW)}$ in D months presents a behavior of rising from 8 - 17 h. After that time, it starts to decay. Close to 17 h, it reaches its maximum, around 1.5 mV/m. Also, $E_{z(GW)}$ in this season presents relatively high intensity (>1 mV/m) between 14-17h30. $E_{z(GW)}$ in E months starts with values close to zero and rise until 1.25 mV/m around midday. Indeed, it presents stronger values between ~ 10 h - 14 h. $E_{z(GW)}$ in J months shows large amplitudes during almost all the diurnal period. It presents ~ 1.5 mV/m between 9 h - 17 h 30 min. Therefore, it seems that in the Brazilian sector the GW activity dominates morning period in equinox, close to sunset hours in summer, and

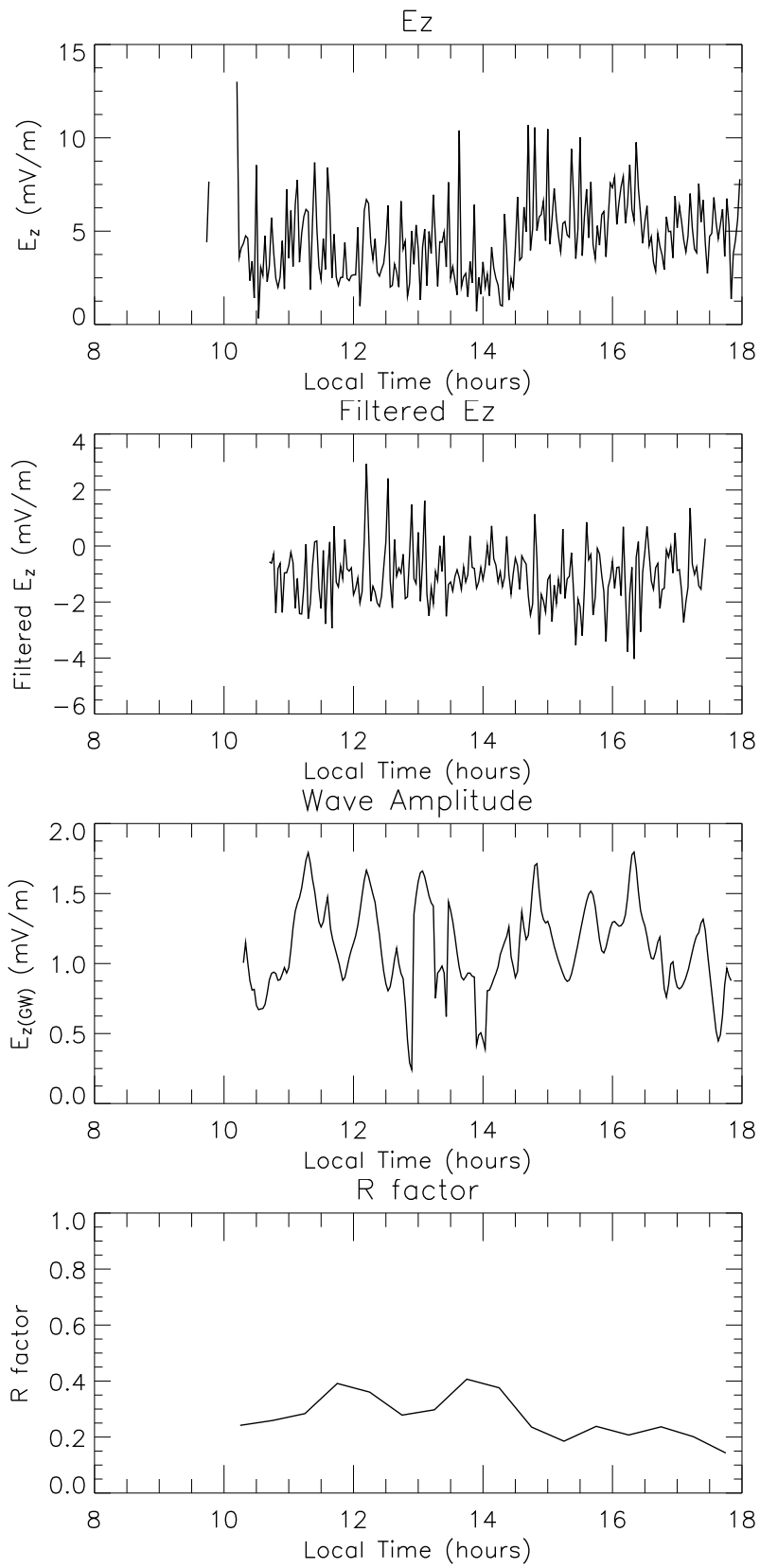


FIGURE 4.1 - Height median of the vertical electric field, filtered field, filtered wave amplitude, and efficiency factor for February 6, 2001.

is highly active during the whole day in winter.

Figure 4.4 shows the statistics of R_{GW} binned in 30-min intervals and 0.05 for (upper panel) solstice D months, (middle panel) equinoctial E months, and (lower panel) solstice J months. The vertical and horizontal lines have the same meaning as in Figure 4.2 and Figure 4.3. The efficiency factor shows very similar features like those described in $E_{z(GW)}$ analysis: strong activity in morning time during equinox, close to sunset hours in summer, and strong activity during the whole day in winter. During summer, close to 17h, the electric fields generated by gravity waves represent 20 % of the total vertical electric field. Indeed, the $E_{z(GW)}$ represents more than 15 % of E_z during the time range between 15 h and 17 h 30 min. During equinox, the disturbed electric fields represents more than 15 % of the total electric fields between 10 h and 14h LT. The maximum GW effect is observed close to 11 h, where the factor reaches up to 17 %. The winter was the season with strongest efficiency for GW activity in electric field, but relatively less frequent than in other seasons, as indicated by the high standard deviations. The disturbed electric fields represent 20 % of the total electric fields almost the whole day. The exception is the first and the last time bin. The maximum appears close to 9 h, where R_{GW} reaches 30 %.

4.3 Period Trends

The GW induced electric fields analysis was performed using Continuous Wavelet Transform (subsection 3.4.1) because only the data with no gaps have been analyzed. For the period trend analysis the Lomb-Scargle Periodogram technique (subsection 3.4.2) has been chosen due to its quality of managing data gaps, since even the data having data gaps were included in the present analysis. The observed period which dominates the spectrum in the range from 4- to 30-min is extracted for each day. The histogram binned in 2-min interval for each season is shown in Figure 4.5. The overall characteristic is that the 4-6 min is the dominant bin, with the 6-8 min bin being the second dominant range period. Indeed, the 4-8 min periodicities concentrate almost 60 % of the occurrences in any season. One remarkable feature is that during summer and equinox the 4-6 min bin is much higher than the others (>20 %). During winter that difference between the 4-6 minutes and 6-8 minutes bins is less than 10 %.

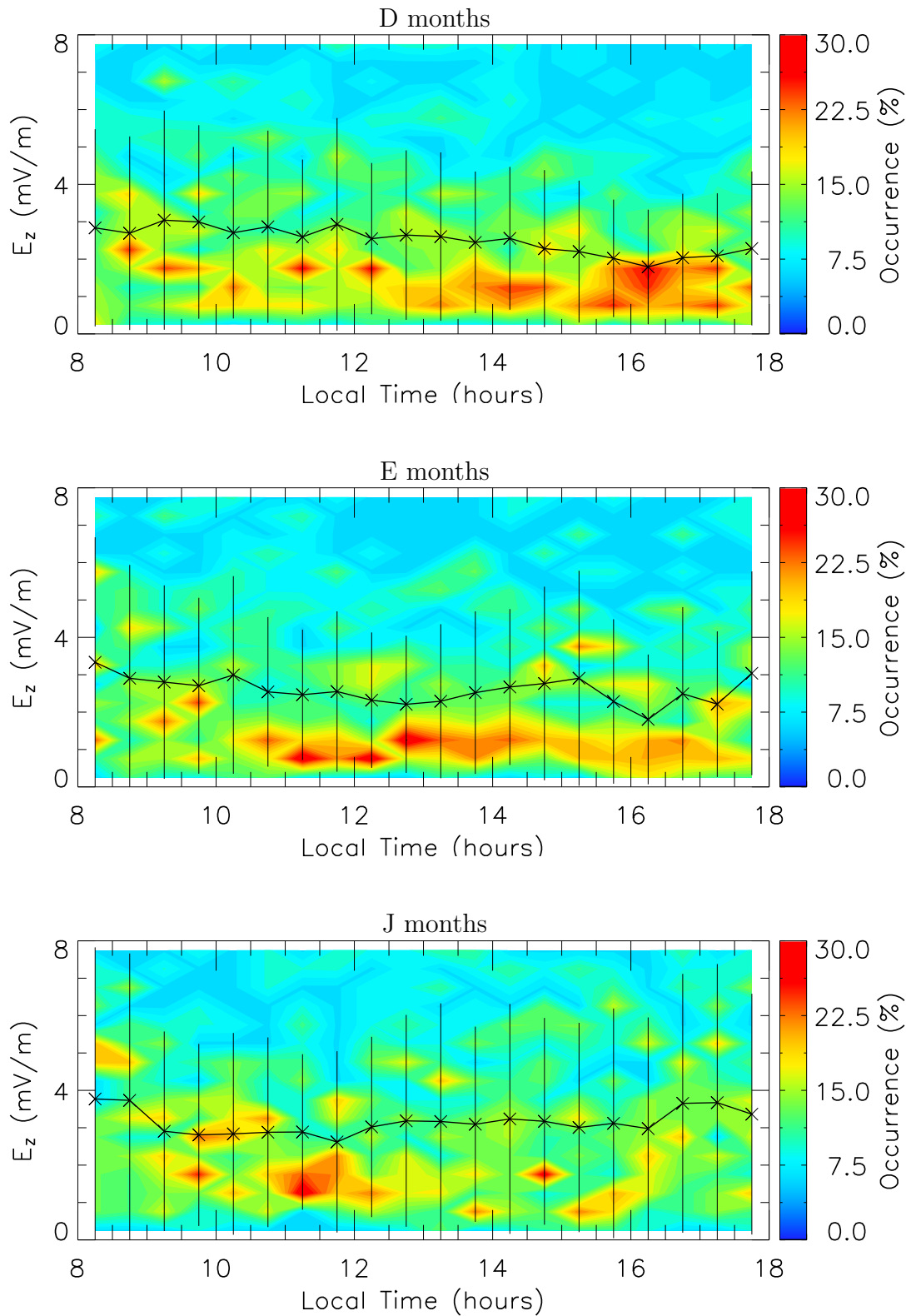


FIGURE 4.2 - Statistics of occurrences of E_z amplitude as function of time for (upper panel) solstice D months, (middle panel) equinoctial E months, and (lower panel) solstice J months. The continuous line represents the average vertical electric field for each 30-min interval and the vertical line is the standard deviation of E_z .

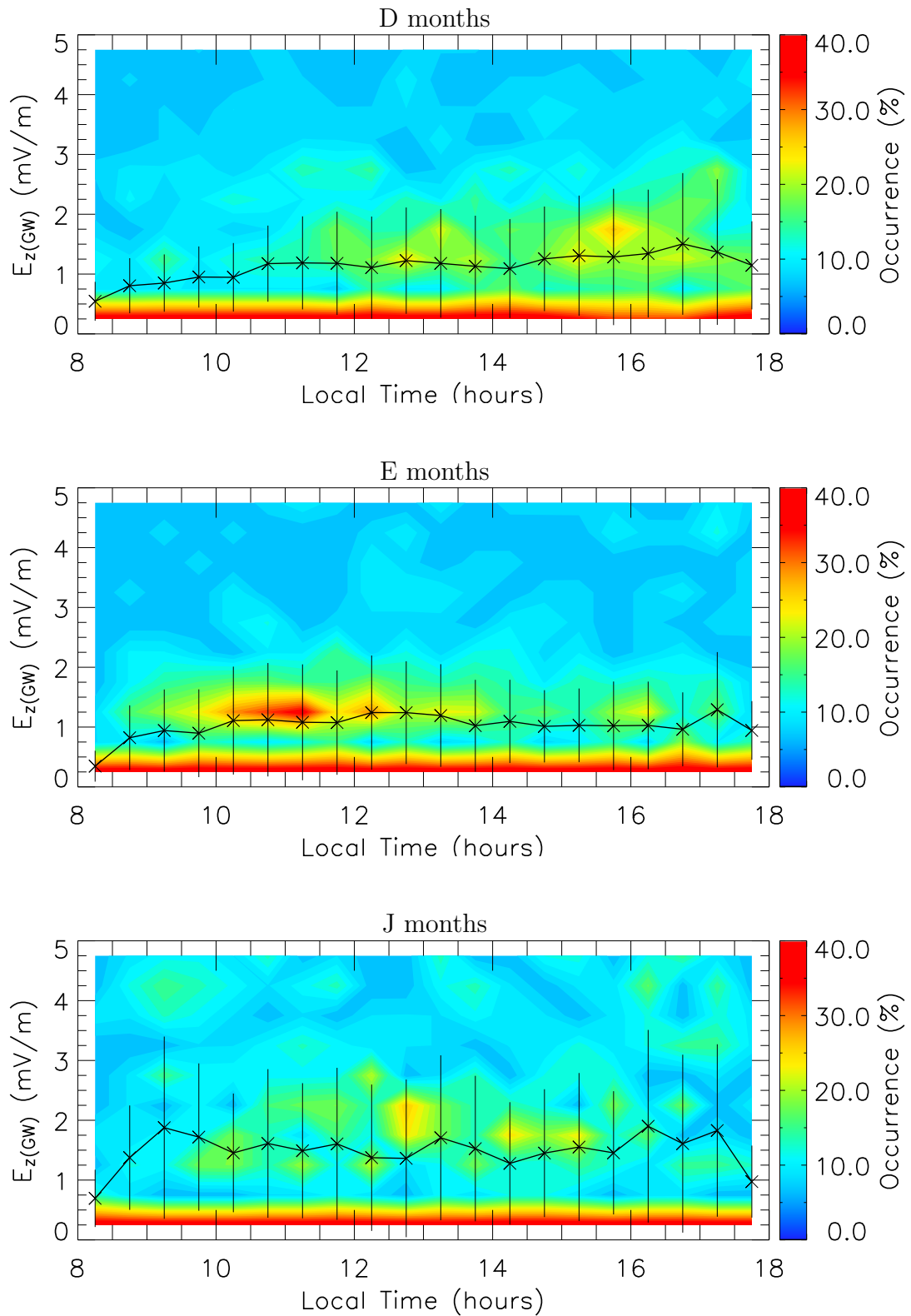


FIGURE 4.3 - Statistics of occurrences of the $E_{z(GW)}$ Amplitude as function of time for (upper panel) solstice D months, (middle panel) equinoctial E months, and (lower panel) solstice J months. The continuous line represents the average disturbed electric field for each 30-min interval and the vertical line is the standard deviation of $E_{z(GW)}$.

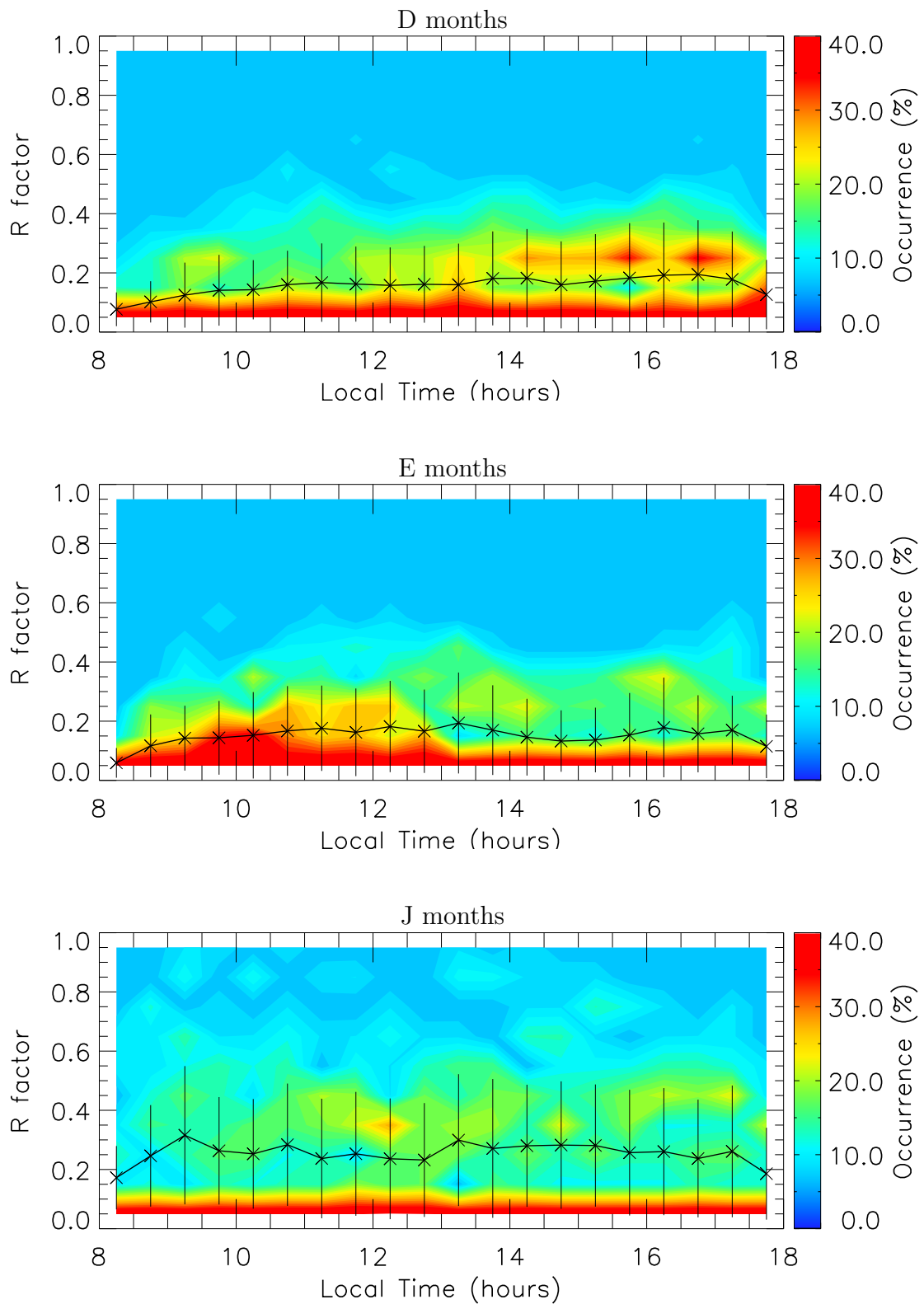


FIGURE 4.4 - Statistics of occurrences of the R_{GW} as function of time for (upper panel) solstice D months, (middle panel) equinoctial E months, and (lower panel) solstice J months. The continuous line represents the average factor for each 30-min interval and the vertical line is the standard deviation of R_{GW} .

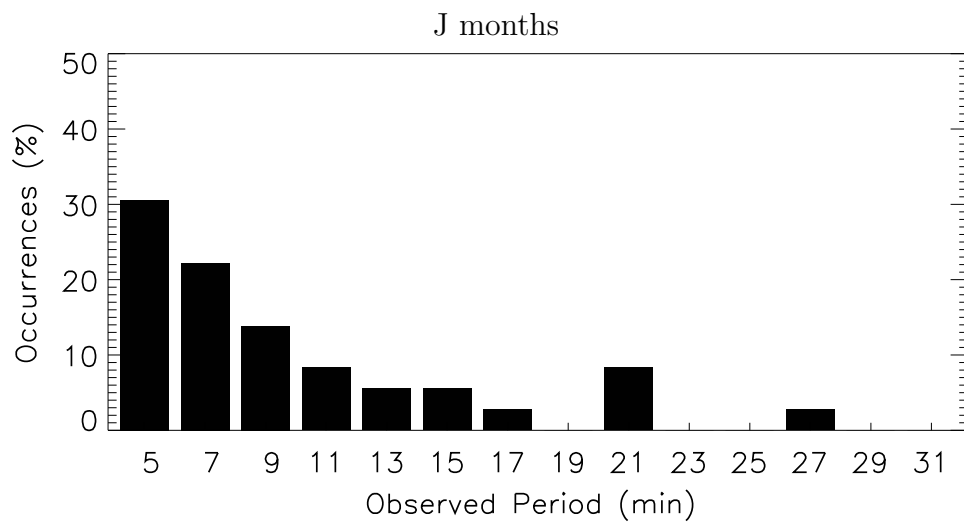
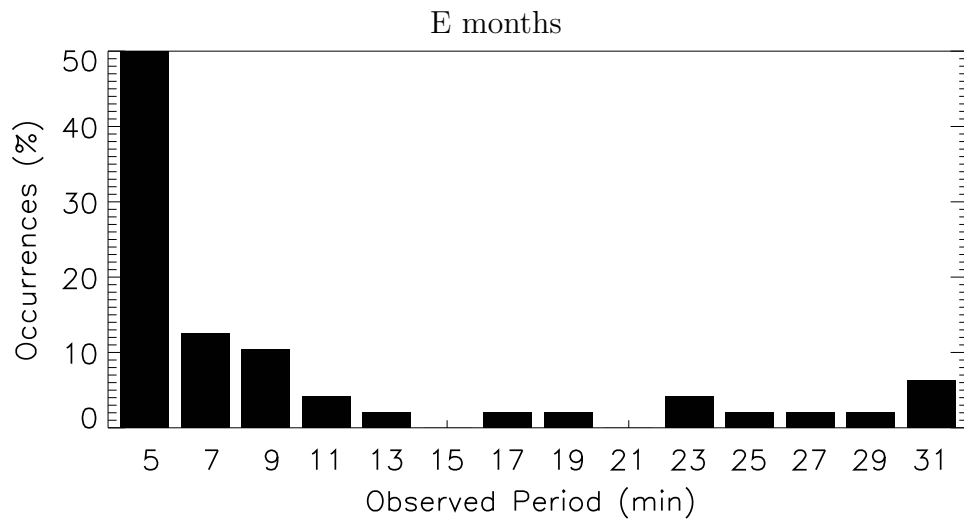
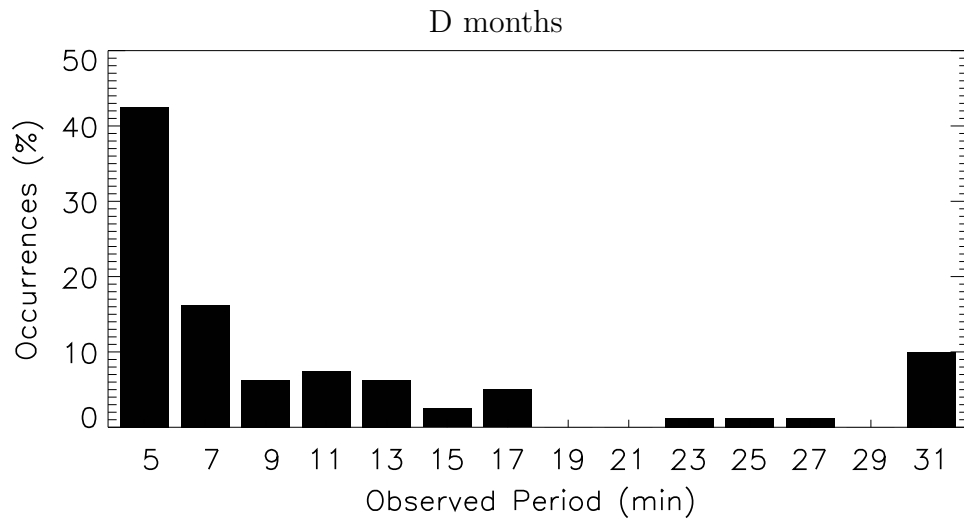


FIGURE 4.5 - Histogram of the observed period binned in 2-minute intervals for (a) D, (b) E, and (c) J seasons.

4.4 Observed Horizontal Phase Velocities

The observed horizontal GW wind velocity was computed through [Equation 1.20](#), but neglecting the curvature of the magnetic field lines and considering that the wind depends only on the altitude. The median of this wind velocity was calculated for each day and its histogram binned in 10 m/s interval for each season, as shown in [Figure 4.6](#). In the upper panel (summer season), the observed horizontal phase velocity concentrates more than 70 % of its occurrences between 20-50 m/s showing no notable variation. The other velocities did not show occurrences higher than 10 %. The middle panel shows the wind velocity statistics for equinoctial months. The remarkable occurrence peak is the 20-30 m/s one, with almost 50 % of the occurrences. The range 40-50 m/s presents almost 20 % of the occurrences and the 10-20 m/s range reaches 10 %. The other velocities seems not to be so observed. The statistics of horizontal GW wind velocities during winter show some similarities with the summer statistics like the range 20-60 m/s concentrating around 75 % of the occurrences. The other ranges seem to be neglectable. The peak of observations is located in the 30-40 m/s range, with ~ 30 % of the occurrences.

4.5 Discussions

4.5.1 Data Reliability

In the present work the oscillations in the range from 4 to 30 min in the vertical electric field of the equatorial electrojet were analyzed. Based on previous theoretical studies by [Kato \(1973\)](#), [Anandarao et al. \(1977\)](#) and on experimental studies by [Reddy e Devasia \(1976\)](#), [Anandarao et al. \(1978\)](#) the assumption that all those short-term fluctuations are caused by gravity waves was taken. Another possible source of short-term variations in the electric fields of the equatorial electrojet are magnetic storms, which has been discarded through the selection of magnetically quiet days only.

It must be remembered that the problems related to COI [subsection 3.4.1](#) were taken into account by removing results having data gaps or close to the edges from the analysis. Therefore, the data reliability is assured. Also, and more important, the results obtained to the range time close to sunset and sunrise (the edges of our data) do not include data having edge effects. However, the number of samples at this range time is reduced compared to other local times considered in the analysis.

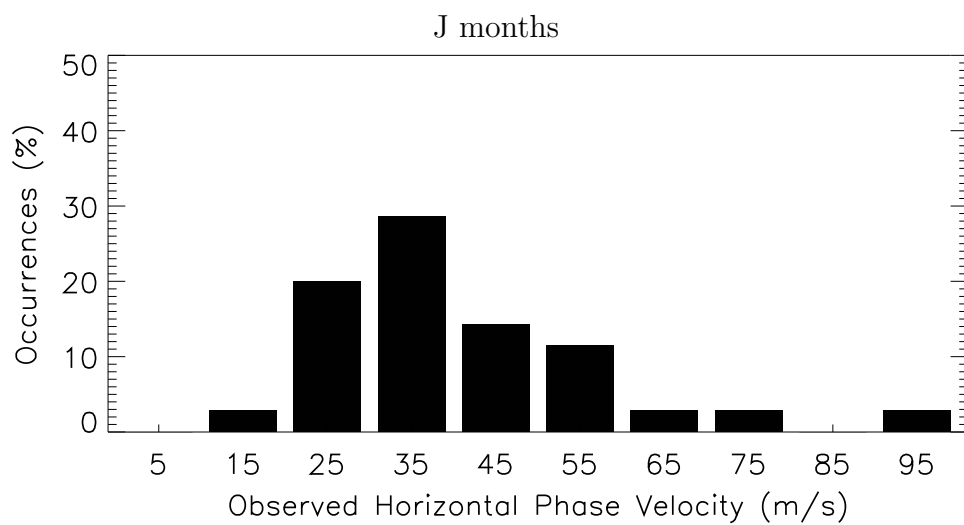
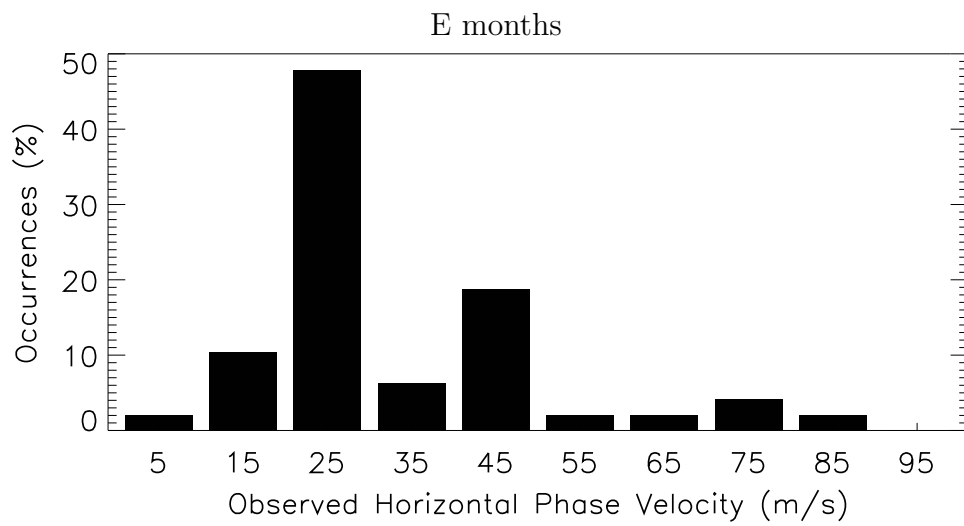
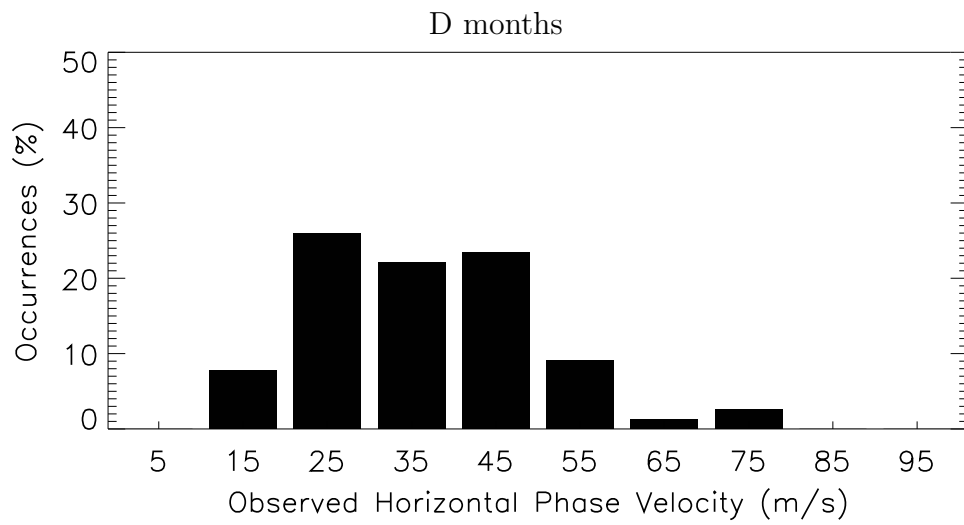


FIGURE 4.6 - Histogram of the observed horizontal wind velocity binned in 10 m/s intervals for (upper panel) D, (middle panel) E, and (lower panel) J seasons.

The observations between 17 h 30 min - 18 h can be affected by the EEJ current reversal. It is caused by the zonal background electric field inversion. At this time the Type II irregularities disappear, so it is not possible to infer gravity wave informations. It means that the GW activity could still be strong after that time (in the first nighttime hours).

4.5.2 Comparison with Airglow Measurements

There are mainly two articles that presents results of gravity wave observations using airglow measurements in the Brazilian equatorial sector at around 90 km heigth (MEDEIROS *et al.*, 2007; TAYLOR *et al.*, 1997). The authors divide the GW observations in two groups: bands - correspond to extensive, freely propagating (or ducted) gravity waves; and ripples - waves of a much smaller scale and transient nature. Since the current data analysis does not discriminate the GW type, the achieved results are a combination of both waves, and it is not able to define the dominant mode. Although, since the bulk observed by the radar beam is large, the radar should observe only the band types.

Taylor *et al.* (1997) carried measurements over Alcantara, Brazil (2.3° S, 44.5° W), during the period August-October 1994 as part of the Guara campaign, a joint cooperation between National Aeronautics and Space Administration (NASA) and Instituto Nacional de Pesquisas Espaciais (INPE). Over 50 wave events were imaged from which a statistical study of the characteristics of equatorial gravity waves has been performed. The larger-scale waves were also found to exhibit strong anisotropy in their propagation directions with the dominant direction of motion toward the \sim NE-ENE suggesting a preponderance for wave generation over the South American continent. Airglow emission measurements from Medeiros *et al.* (2007) were made at São João do Cariri (7° S, 36° W), from October 2000 to December 2004. A large amount of image data, more than 3000 h of observation and around 1000 wave events were analyzed. In most cases band-type waves showed a clear preference for the horizontal propagation direction from the South American continent to the Atlantic Ocean. Ripples have also shown similar features but with different anisotropy.

Combining the whole data set (2001, 2002, and 2004) in one single group and re-analyzing the observed periodicities (similar to what is done in Figure 4.5), the average periodicity for the whole period has been calculated. The same procedure has been performed with the observed phase velocity. A comparison among the

TABLE 4.1 - Gravity wave characteristics from airglow image data compared to the current results

Parameter	Taylor et al. (1997)		Medeiros et al. (2007)		Present study
	Bands	Ripples	Bands	Ripples	General
Observed Mean Period (min)	9.6	5.1	11.1	9.6	10.4
Observed Mean Phase Velocity (m/s)	48	44	36	29	36

present results, the results from Taylor et al. (1997), and the results from Medeiros et al. (2007) are summarized in Table 4.1. As mentioned before, GW type are not discriminated in the present work. However, a vis-à-vis comparison of the wave parameters, like periodicities and phase velocities, reviews no clear difference between achieved results in the present work and the previous ones reported for the Brazilian equatorial sector. Therefore, EEJ Type II velocities seems to be a good tool in GW characteristics identification.

4.5.3 Overall Features and Implications

The statistics of vertical electric field perturbations (related to gravity wave winds) show different behavior for different seasons. D months concentrate most of the GW occurrences in the hours close to sunset, between 15 h and 17 h LT. Most of the occurrences in the morning period are likely to be observed in the E months. Differently of the other two seasons, GW occurrences in J months are spread all over daytime. Despite of this remarkable differences, there is no report of seasonal variation effects in the coupling between the E- and F-regions related to this matter. The results that $E_{z(GW)}$ in summer are more probable to occur close to sunset may have some implications to F-region also. Prakash (1999) shows that perturbations due to GW in the electric fields could seed Spread-F irregularities. And the present results showed that $E_{z(GW)}$ are stronger close to sunset in summer, when Spread-F occurrences in the Brazilian sector are higher. So, it indicates that both events could be related. It needs to be further investigated to identify cause-effect however.

Gravity wave kinetic energy as well as variances in each of the three component wind directions have shown a semiannual variation at these altitudes with maxima

in summer and winter and minima in spring and fall (FRITTS; ALEXANDER, 2003, and references therein). The results of Kovalam et al. (2006) showed strong diurnal modulation of the GW wind velocities with peaks in the mid-morning and close to sunset. Such modulation of the velocities is due to the effect of the diurnal tide, which has non-negligible amplitudes in horizontal winds, even near the equator. Another effect that must be taken into account is the effect of tidal temperature perturbations, which are quite substantial at equatorial latitudes. A well-known effect is the modulation of the Brunt-Vaisalla frequency. Thereafter, changes in the vertical wavelength of gravity waves and hence the saturation conditions can be observed. The overall diurnal variability in the gravity wave winds is therefore a consequence of a complicated interaction between the tidally induced winds and temperature variability itself. So, the seasonal behavior results achieved in the present work seems to be due to a combination of tidal modulation and semiannual variation.

Finally, it should be mentioned that the current presented method has some limitations. It does not provide any information about the vertical or horizontal wavelengths (or wavenumber). Also, polarization field generated by the gravity wave is $\mathbf{U} \times \mathbf{B}$ ($|U| \cdot |B| \cdot \sin \theta$), which means that the electric field oscillations are dependent of the angular relation between the direction of the wave propagation and the Earth's magnetic field lines. If the wave propagates perpendicular to the magnetic field, the effect is maximized. If the declination of the radar site is close to 0° , it may be more suitable to infer features from the zonal component of the gravity wave such as zonal wavelength, zonal wavenumber, and zonal velocity and its variance. Since the study is based on radar data from São Luís Space Observatory (OESLZ), with $\sim 20^\circ$ of declination, the present results may have some small contributions from meridional component of the GW neutral winds. Although, Taylor et al. (1997) show that the dominant direction of GW motion in Alcantara is \sim NE-ENE, which means that the gravity waves propagate almost perpendicular to the Earth's magnetic field ($\theta \cong 0^\circ$) in the São Luís region.

4.6 Conclusions

From the Type II EEJ irregularity velocities obtained by coherent radar data gravity wave characteristics has been inferred and its influence in the vertical ionospheric electric fields have been studied. The comparison between this method and previous reports (based on airglow measurements) of gravity wave parameters (periodicities and phase velocities) obtained in the equatorial South American sector shows good

agreement. The vertical electric field perturbations related to gravity wave winds show a seasonal behavior of their occurrences: D months close to sunset; E months in the morning hours; and J months almost in the whole day. This seasonal behavior seems to be a combination of tidal modulation and semiannual variation. The higher sunset activity of GW in summer, when Spread-F occurrences in the Brazilian sector are higher, may indicate some E- and F-region coupling. However, such effect needs to be further investigated to identify cause-effect relationship.

5 SIGNATURES OF 2-DAY WAVE IN THE E-REGION ELECTRIC FIELDS AND THEIR RELATIONSHIP TO WINDS AND IONOSPHERIC CURRENTS

In the present work the effects of the 2-day wave activity in the EEJ using one coherent radar and eight magnetometer stations located close to the dip equator were analyzed. The wavelet analysis of the magnetometer data reveals a 2-day signature in the semidiurnal geomagnetic tide. The E-region zonal background ionospheric electric field, derived from coherent radar measurements, shows 2-day oscillations in agreement with such oscillations in the magnetometers data. An anticorrelation between the tidal periodicities (diurnal, and semidiurnal) and the 2-day signature is also shown in the electric fields. The results are compared with simultaneous observations of 2-day planetary wave in meridional winds and ionosondes available in the literature. Still, the present results are discussed based on the analysis of the magnetic activity.

5.1 Two-Day Wave in the E-Region Electric Fields

5.1.1 Radar Experimental Description

The basic RESCO radar experimental description and the determination of vertical electric fields (E_z) from the radar data were presented in [section 4.1](#). Afterward, effects of vertical current over the magnetic equator were included by integrating the EEJ electric current equation along the magnetic field lines. This was made based on [Richmond \(1973\)](#) conclusion, which states that EEJ current value should depend on the conductivity integrated along the magnetic field line because the vertical electric field (E_z) driver is mapped along these lines. For this reason ionospheric conductivity model developed by [Denardini \(2007\)](#) was chosen, which calculate the Hall (σ_2) and Pedersen (σ_1) conductivities at each point of the geomagnetic field lines along the magnetic meridian at the radar site with height resolution of 1 km, and integrate them along the geomagnetic field line. Thus, the relation between the equatorial electric fields is given by:

$$E_o = \frac{\int_{-\theta}^{+\theta} \sigma_1 \cdot \mathbf{r} \cdot d\boldsymbol{\theta}}{\int_{-\theta}^{+\theta} \sigma_2 \cdot \mathbf{r} \cdot d\boldsymbol{\theta}} \cdot E_z \Rightarrow E_o = \frac{\Sigma_1}{\Sigma_2} \cdot E_z. \quad (5.1)$$

where E_o is the E-region background electric field, \mathbf{r} is the position vector of the magnetic field line element considering a dipole geometry, θ is the magnetic latitude, $d\theta$ is the differential magnetic latitude element vector and the quantities Σ_2 and Σ_1 are the Hall and Pedersen field-line integrated conductivities, respectively.

5.1.2 Results

In order to obtain information on the periodicity of the background E-region zonal electric fields, a spectral analysis was performed. A period of 10 days in January (20-24 and 27-31) and 10 days in February (17-21 and 24-28) have been chosen for the present analysis. The Lomb-Scargle algorithm (LOMB, 1976; SCARGLE, 1982) described in subsection 3.4.2, was used because the RESCO radar soundings are only carried between 8-18 h LT. Figure 5.1 shows the Lomb-Scargle periodogram calculated for the vertical electric fields for (a) 20-24 January, (b) 27-31 January, (c) 17-21 February, and (d) 24-28 February, in 2003. The horizontal (dash dot) line indicates the level of 99% of confidence ($=9.90 \text{ mV}^2/\text{m}^2$). In general, the periodograms show two remarkable period peaks below 1-day: ~ 0.5 -, and ~ 1.0 -days. Consequently, semidiurnal and diurnal tidal winds play an important role in the dynamo electric field. Signatures of 2-day waves are seen in the period of 27-31 January, anticorrelated to the tidal modes. It is seen as a reduction of the tidal amplitudes when the 2-day wave appears. Also, February electric fields show remarkable periodicities of 1.9 days. Although, they do not show the same anticorrelation observed in the 27-31 January between the 2-day wave and the tidal modes.

5.2 Two-Day Signature in the EEJ currents

5.2.1 Magnetometer Data

Hourly geomagnetic data were obtained for 8 stations close to the magnetic equator (magnetic lat. $< \sim 5^\circ$). The global map station location is seen in Figure 5.2 and informations about them are shown in Table 5.1. From these data, the H-component variation with respect to the midnight base level, (denominated as dH) was calculated. An example of dH time series for HUA station (Huancayo) is shown in Figure 5.3. dH observed at a point on the ground is not only due to the overhead currents, but also due to the currents flowing over a latitudinal extent of a few degrees on either side of the overhead point (VIKRAMKUMAR et al., 1987). Also, the observed dH variations at ground levels consists of two contributions: one due to

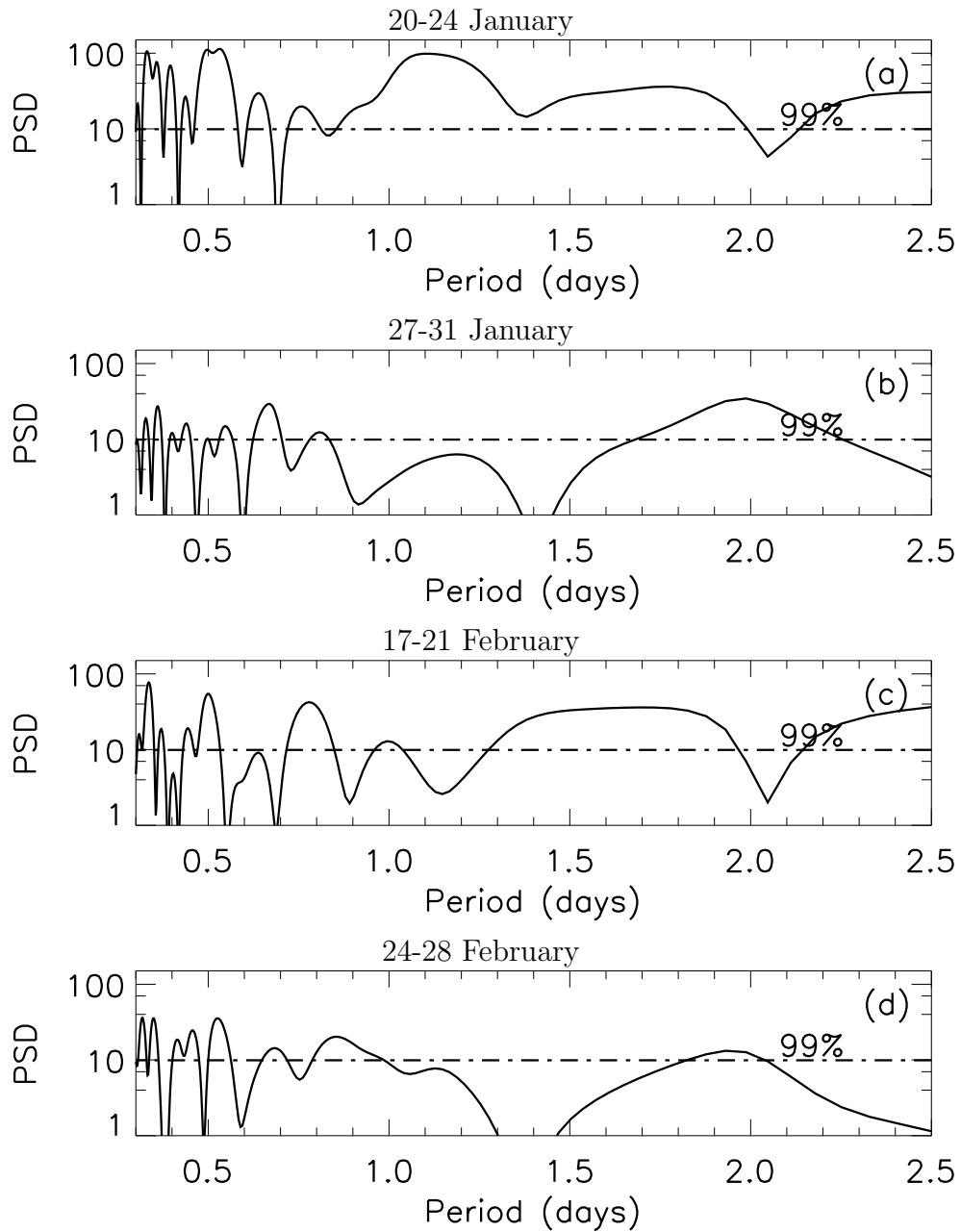


FIGURE 5.1 - Lomb-Scargle periodogram calculated to the zonal electric field for (a) 20-24 January, (b) 27-31 January, (c) 17-21 February, and (d) 24-28 February, in 2003. The horizontal (dash dot) line indicates the level of 99% of confidence ($=9.90 \text{ mV}^2/\text{m}^2$).

currents in the EEJ itself (dH_{ext}), and other due to currents induced by the electrojet in the earth (dH_{int}).

External current systems, the equatorial electrojet in that case, induce secondary currents in the Earth's mantle; and their magnetic field is observed at the Earth's

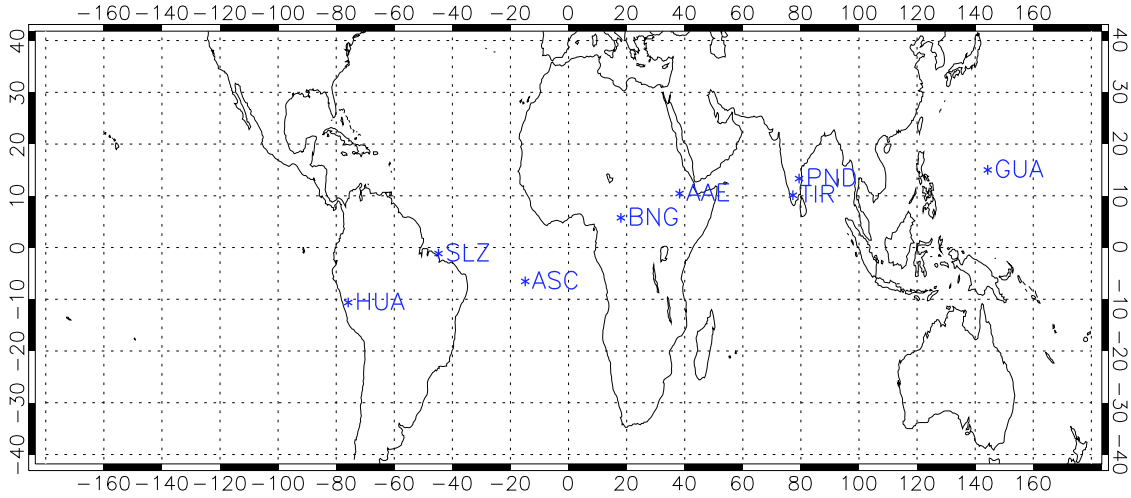


FIGURE 5.2 - Magnetometer stations locations.

TABLE 5.1 - Magnetic Latitude of the Magnetometer Stations and their Geographic Coordinates

Station Code	Dip. Lat.	Latitude	Longitude
ASC	-2.36	-7.95	-14.38
SLZ	-2.25	-2.58	-44.23
HUA	-1.80	-12.04	-75.32
TIR	-0.17	8.70	77.80
PND	2.85	11.92	79.92
BNG	4.20	4.33	18.57
GUA	5.30	13.59	144.87
AAE	5.32	9.03	38.77

surface as internal contributions (OLSEN, 1997). Since the latter is the effect and the former the cause, the corresponding geoelectric currents are well correlated with the magnetic variations of ionospheric origin. Many studies related to H_{int}/H_{ext} have estimated that the ratio vary between 0.39-0.70 for different longitude zones (VIKRAMKUMAR et al., 1987, and references therein). Sampath e Sastry (1979), based on their rocket-borne observations of the electrojet current near Thumba, showed that the induced current is only 39% of the jet current. This is almost equal to the globally averaged value of 40% obtained by Duhau e Osella (1982). Also, Vikramkumar et al. (1987) apply an approximation of $\Delta H_{ext}=0.72 \times \Delta H$ to compare observed ΔH values with those estimated from measured electric fields. Based on that, the

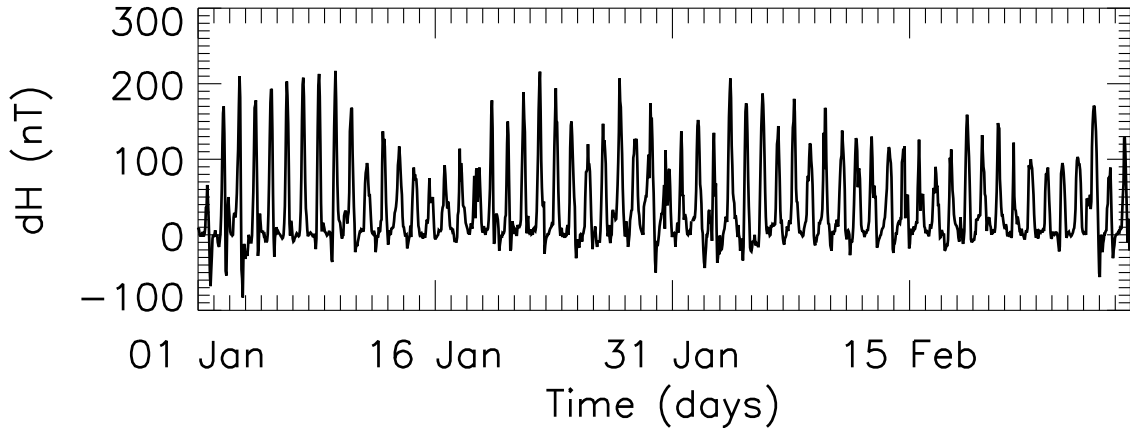


FIGURE 5.3 - H-component variation with respect to the midnight base level (dH) for HUA station during Jan-Feb 2003.

$dH \approx dH_{ext}$ assumption (neglecting the internal effects) may lead to an overestimation of the magnetic field variations due to EEJ currents. Still, the analysis was restricted to magnetometer stations close to the magnetic equator (magnetic lat. $< \sim 5^\circ$), dH is supposed to contain mainly the EEJ influence. Another sources that may have some influence in dH data (e.g., from magnetospheric sources) are discussed in [section 5.4](#).

5.2.2 Results

[Figure 5.4](#) shows the wavelet analysis of dH , performed using 1 hour of time resolution, and 0.125 of scale resolution, to the 8 selected magnetic stations for periodicities in the range 0.25-4.0-days in January-February 2003. The figures are arranged by dip latitude. If they would be arranged by magnetic latitude, stations closer to equator would show the larger amplitudes. As a general result, it is clear that the diurnal and semidiurnal tides are higher than the 2-day wave modulation in dH almost all the time. Stations close to dip equator show strong tidal modulation in dH . The only exception is the AAE station which is located in 5.32° of magnetic latitude. Two-day wave modulation of dH is observed in all stations: ASC for 26-31 Jan; HUA for 1-10 Feb, TIR for 30 Jan-7 Feb, SLZ for 1-8 Feb, PND for 30 Jan-10 Feb, BNG for 27 Jan-1 Feb, GUA for 31 Jan-8 Feb, and AAE for 27 Jan-13 Feb. These are the most remarkable periods with 2-day modulation, but there are other dates where it can be observed also, like during 18-23 Feb in HUA.

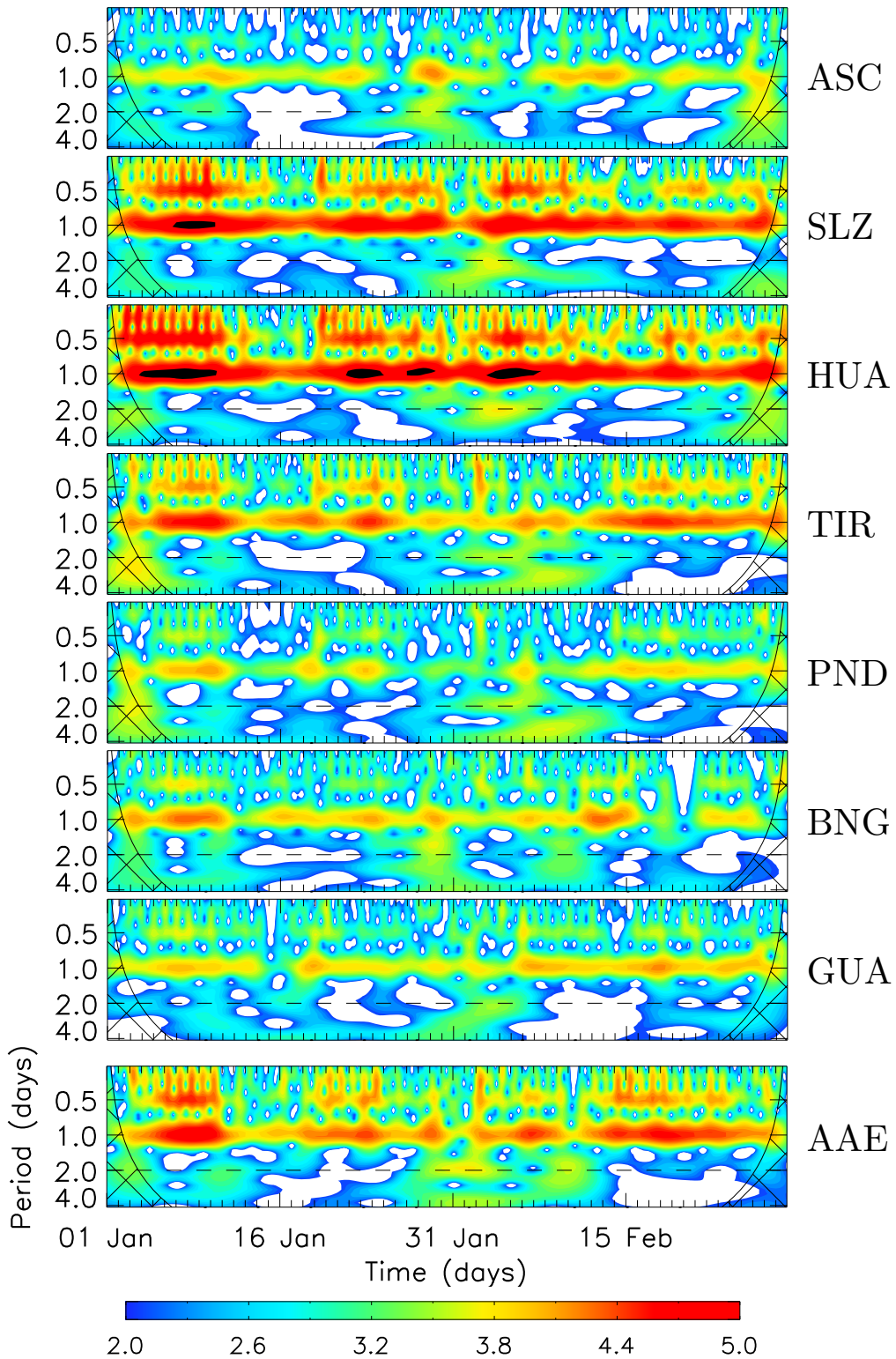


FIGURE 5.4 - Space-scale energy density in log-scale of dH in January-February 2003 for the eight magnetic stations (from top to bottom): ASC, SLZ, HUA, TIR, PND, BNG, GUA, and AAE.

Figure 5.5 presents the wavelet analysis of the amplitude of the diurnal tide in dH for the same magnetic stations and period as in Figure 5.4. Two-day modulation of diurnal tide is not observed. Indeed, the dominant periodicities lies in the range from 4-8 days. Occurrences of quasi-2-day periodicities after 28 January for stations closer to dip equator were also observed.

Figure 5.6 presents the wavelet analysis of the amplitude of the semidiurnal tide in dH . Two-day modulation of semidiurnal tide is clearly observed in almost all magnetometer stations, together with other remarkable periodicities. The 2-day modulation of the semidiurnal tide seems to appear between 10 January - 10 February. The events are not continuous during all the period, they appear as burst-like occurrences with 5-10 days persistence. Another interesting feature is the fact that the 2-day wave signature is sometimes seen in the semidiurnal mode of dH , but it is not observed in the amplitude of dH , as previous reported.

5.3 Previous Reports of 2-Day Waves Observations in January-February 2003

Pancheva et al. (2006) analyzed the 2-day wave coupling of the low-latitude atmosphere-ionosphere system in the neutral winds by radar measurements located at four tropical stations, in the ionospheric electron density by seven ionosonde stations, and in the ionospheric electric currents by twenty-three magnetometer stations, during the period between 1 December 2002 and 28 February 2003. The results of Pancheva et al. (2006) are summarized as follow:

- a burst-like 2-day wave activity prevailed in the tropical mesosphere/lower thermosphere (MLT) region having the following features: (a) the 2-day wave appeared in late December (around 25 December), peaked at most of the stations between 10 and 25 January, and persisted until early February; (b) westward propagation of the 2-day wave, but with no single wave number found; (c) vertical wavelengths were quite similar for all stations, ~ 50 to 65 km; and (d) the 2-day wave appeared to penetrate into the dynamo region for part of the time (predominantly after 20 January); and
- simultaneous magnetometer data from a large number of stations in the tropical zone revealed the 2-day variability in the geomagnetic components appeared as modulations of the quiet-day Sq diurnal cycle, and ionosonde

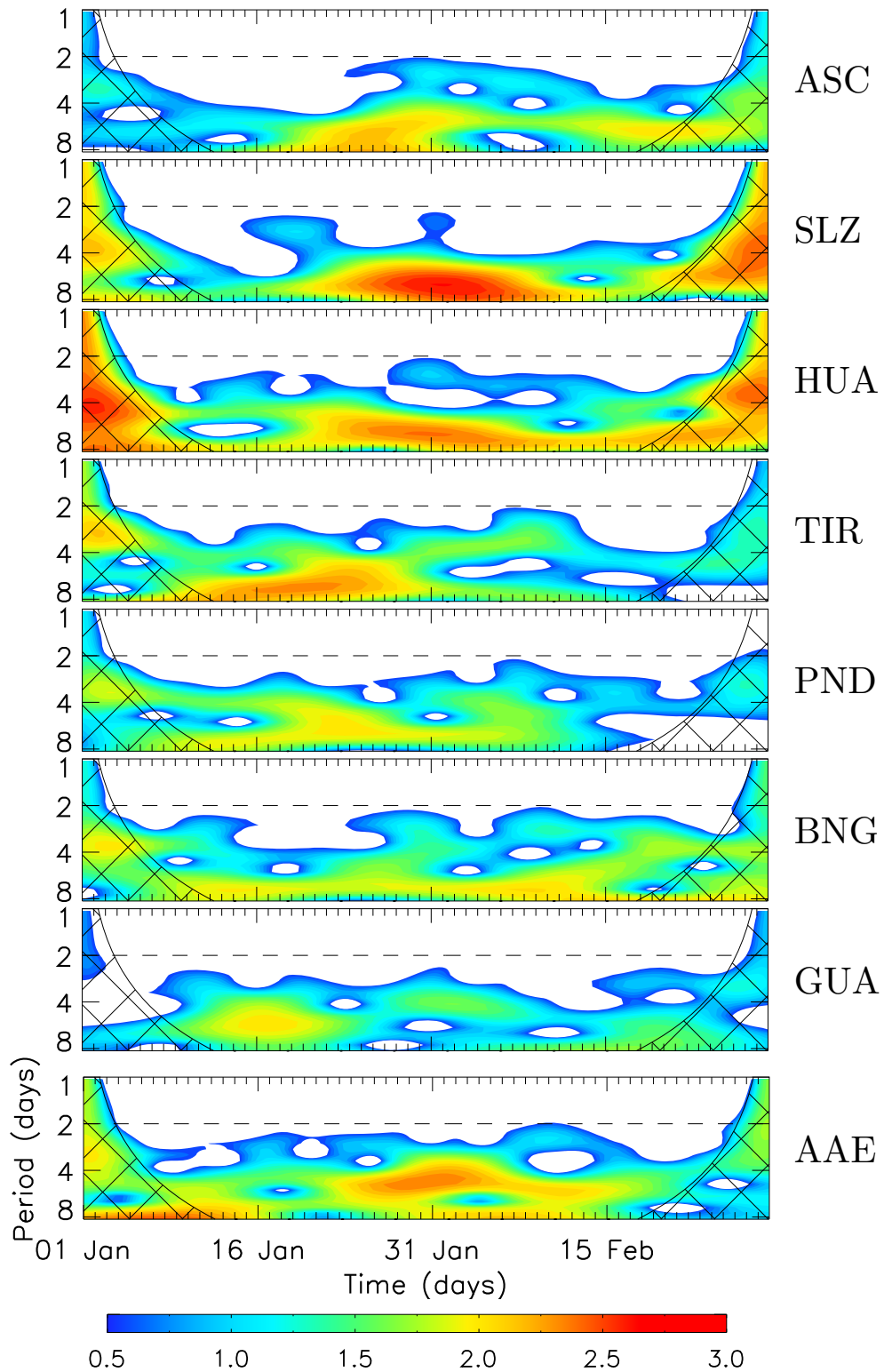


FIGURE 5.5 - Space-scale energy density in log-scale of the amplitude of the diurnal tide (0.90-1.15 days) in January-February 2003 for the eight magnetic stations (from top to bottom): ASC, SLZ, HUA, TIR, PND, BNG, GUA, and AAE.

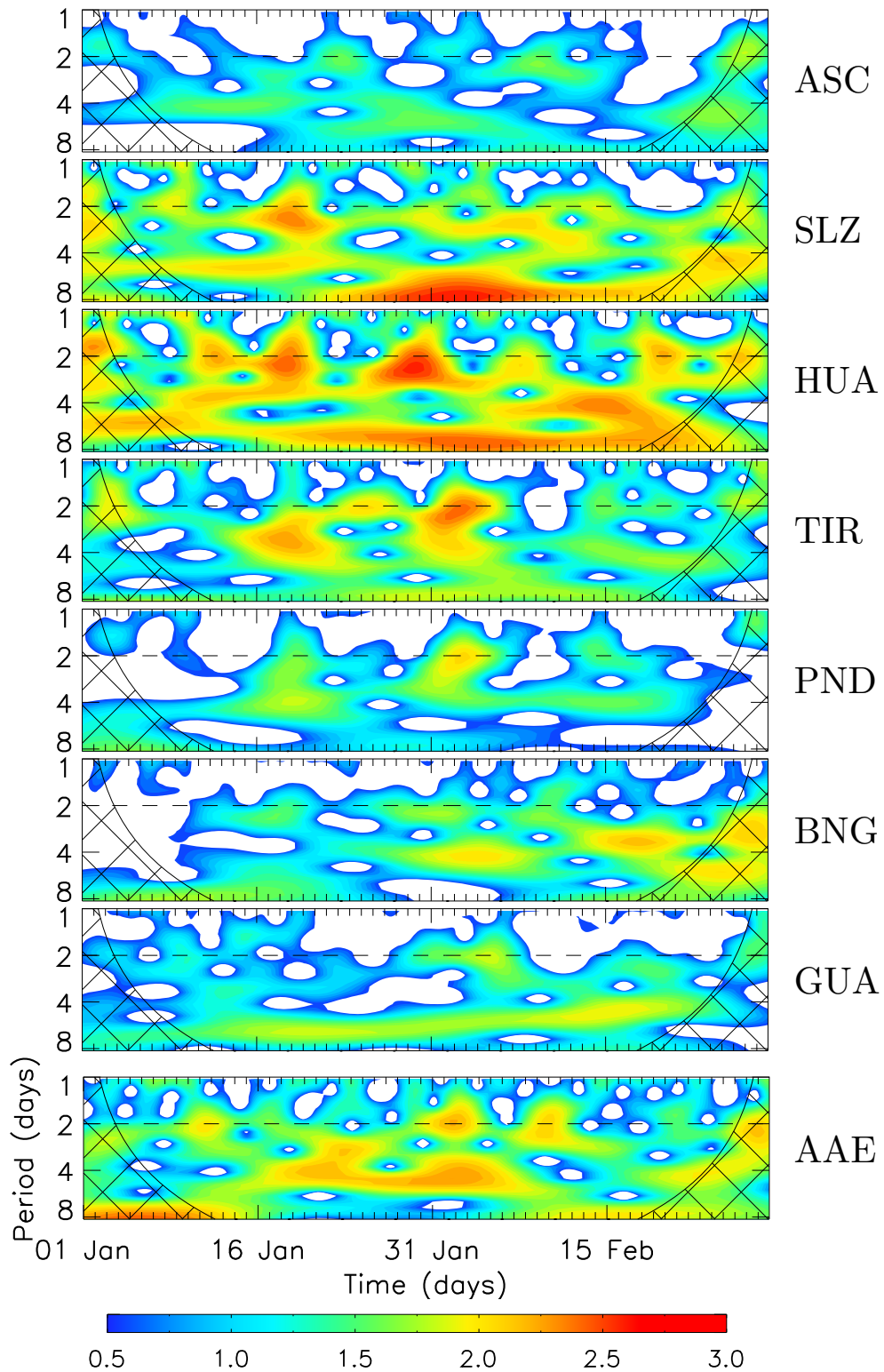


FIGURE 5.6 - Space-scale energy density in log-scale of the amplitude of the semidiurnal tide (0.40-0.60 days) in January-February 2003 for the eight magnetic stations (from top to bottom): ASC, SLZ, HUA, TIR, PND, BNG, GUA, and AAE.

data from seven tropical stations indicated the same periodicity in foF2.

The 2-day modulation of the 24-hour tidal amplitude at the initial and final stages of the 2-day wave activity is probably due to the observed anticorrelation between the 2-day wave activity and the diurnal tide (PANCHEVA *et al.*, 2006, and references therein). They concluded that the main forcing agent in this atmosphere-ionosphere coupling seems to be the modulated tides, particularly the semidiurnal tide. The parameter that appears to be affected, and thus drives the observed 2-day wave response of the ionosphere, is the dynamo electric field (PANCHEVA *et al.*, 2006). They still suggest that 2-day wave response in the geomagnetic components does not appear to require the direct involvement of the 2-day wave in the vertical coupling (or at least not during the entire period).

5.4 Discussions

The indirect evidence of the presence of 2-day planetary wave oscillations in the EEJ was analyzed based on data from a VHF coherent radar and eight magnetometer stations located close to the dip equator and the results are summarized as follow:

- a) E-region background zonal electric field: (a) E_o shows a remarkable 2-day signature in the period 27-31 January; and (b) a anticorrelation between 2-day activity and the tidal modes (0.5-, and 1.0-days) is observed in the same period.
- b) equatorial electrojet current: (a) the EEJ currents are clearly affected by the 2-day planetary wave; (b) 24-hour tidal amplitude in ionospheric currents are not modulated by the 2-day wave. Indeed, the tide that is modulated is the 12-hour, i.e., the semidiurnal mode; and (c) the detection of the 2-day is better observed in the wavelet analysis of the semidiurnal tidal amplitude, rather than in the diurnal tidal amplitude and the H-component variations.

The inferred zonal electric fields are dependent of the collision frequencies and, according to Pancheva *et al.* (2006), the planetary waves may affect the collision frequencies through composition changes in the turbopause. However, the direct effect on the dynamo electric field is far more important. Still, the zonal current

density in the EEJ (J_o , which mainly cause the dH variation) is related to the E_o through

$$J_o = \left(\sigma_1 + \frac{\sigma_2^2}{\sigma_1} \right) \cdot E_o. \quad (5.2)$$

Therefore, the present results show good agreement between the observations of currents and electric fields. Also, despite of the fact that the tidal wind systems were related as the main source of currents and electric fields, two other physical processes can affect it:

- disturbance dynamo (BLANC; RICHMOND, 1980) - a current system driven by winds generated by external sources usually attributed to particle heating and Joule heating in the auroral zone; and
- direct penetration of electric fields from high-latitude to low latitudes (SPIRO et al., 1988) - the high-latitude ionospheric convection electric is not completely shielded from low and middle latitudes due to abnormal drift times of particles in the ring current.

The short-term disturbances in the equatorial ionosphere may be caused by solar ionizing flux variations, and geomagnetic storms. Parish et al. (1994), for instance, point out that a 13.5- and a 27-day oscillation in the EUV fluxes may affect the ΔH variations through their influence on the E-region conductivity. Hence, the geomagnetic activity based on the Dst and AE indices were analyzed in order to distinguish periodicities caused by magnetic storms and substorms to those caused by “meteorological” sources. The Dst provide a good indication of the magnetic disturbance over low latitude, while the auroral indices in general would represent the degree of variability in the magnetospheric source of the disturbance electric field that penetrate to the equatorial latitudes. Figure 5.7 shows the magnetic indices and Figure 5.8 presents the space-scale energy density of the indices. It can be seen that there are several small storms ($-50 \text{ nT} \leq \text{Dst} < -30 \text{ nT}$) and two moderate storms ($-100 \text{ nT} \leq \text{Dst} < -50 \text{ nT}$) in the periods 1-6 and 26-28 February. The space-scale energy density points out a remarkable period with 2-day modulation of the indices from 1-6 February. It means that the 2-day signatures in the zonal electric fields and ionospheric currents observed in late January were possibly caused by ionospheric dynamo-planetary waves interaction, and not by magnetospheric disturbances. The results of Pancheva et al. (2006) support the present analysis in the same way, since

a 2-day wave activity is observed in the tropical MLT region with a remarkable 2-day modulation of the diurnal and semidiurnal tidal amplitudes at 27-31 January (simultaneously with the present results).

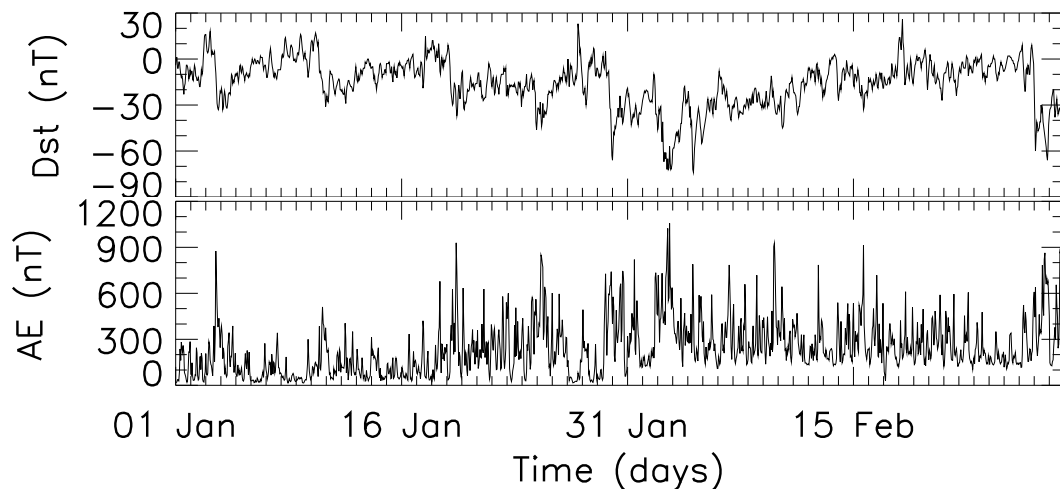


FIGURE 5.7 - Dst and AE indices for January-February 2003.

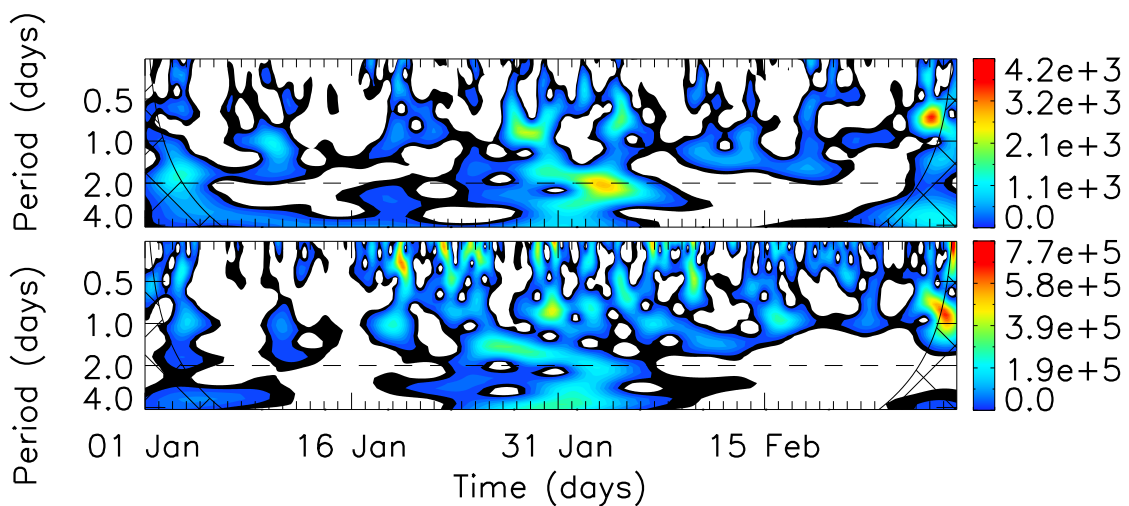


FIGURE 5.8 - Space-scale energy density of the Dst and AE indices for January-February 2003.

5.5 Conclusions

This work intends to be the first attempt to demonstrate the signature of 2-day planetary wave in the dynamo electric field, based on E-region zonal electric fields inferred by a VHF coherent radar. A good agreement was found between the current observations in the electric fields and ionospheric currents, and the meridional winds. An anticorrelation between the tidal periodicities (diurnal and semidiurnal) and the 2-day signature is shown in the electric fields. The 24-hour tidal amplitude in ionospheric currents seem to be not modulated by the 2-day wave. The detection of the 2-day is better observed in the wavelet analysis of the semidiurnal tidal amplitude, rather than in the diurnal tidal amplitude and the H-component variations. Finally, it must be stressed that additional coordinated campaigns should be organized aiming further informations of the neutral atmosphere-ionosphere interactions.

6 CONCLUSIONS AND FUTURE WORKS

The present results are inserted in the context of ionosphere-neutral atmosphere coupling studies in the E-region based on VHF radar measurements. The main contributions of the current studies about electric and magnetic signatures of gravity waves and 2-day planetary waves in the equatorial E-region are:

- development of algorithms and program codes for helping the data analysis of gravity waves in the vertical electric fields, planetary waves in the ionospheric currents, and wave-type oscillations in the magnetic indices. Such codes include wavelet transform and Lomb-Scargle periodogram;
- organization of a magnetic indices and a worldwide magnetometer database (based on WDC - Kyoto and Brazilian data) for future data processing, as well as programs for their loading and processing; and
- development of a new methodology for gravity wave detection and characteristics analysis, validated by airglow measurements.

Specifically, in relation to the study *CLIMATOLOGY OF GRAVITY WAVES-INDUCED ELECTRIC FIELDS*, the conclusions are:

- from the Type II EEJ irregularity velocities obtained by coherent radar data gravity wave characteristics has been inferred and its influence in the vertical ionospheric electric fields have been studied;
- the comparison between this method and previous reports (based on airglow measurements) of gravity wave parameters (periodicities and horizontal phase velocities) obtained in the equatorial South American sector shows good agreement;
- the vertical electric field perturbations related to gravity wave winds show a seasonal behavior of their occurrences: D months close to sunset; E months in the morning hours; and J months almost in the whole day;
- this seasonal behavior seems to be a combination of tidal modulation and semiannual variation; and

- the higher sunset activity of GW in summer, when Spread-F occurrences in the Brazilian sector are higher, may indicate some E- and F-region coupling.

In relation to the study SIGNATURES OF 2-DAY WAVE IN THE E-REGION ELECTRIC FIELDS AND THEIR RELATIONSHIP TO WINDS AND IONOSPHERIC CURRENTS, it was concluded that:

- it was the first attempting to demonstrate the signature of 2-day planetary wave in the dynamo electric field, based on E-region zonal electric fields inferred by a VHF coherent radar;
- it was found a good agreement between the current observations in the electric fields and ionospheric currents, and the meridional winds;
- an anticorrelation between the tidal periodicities (diurnal and semidiurnal) and the 2-day signature was shown in the electric fields;
- the 24-hour tidal amplitude in ionospheric currents seem to be not modulated by the 2-day wave; and
- the detection of the 2-day is better observed in the wavelet analysis of the semidiurnal tidal amplitude, rather than in the diurnal tidal amplitude and the H-component variations.

Finally, it is important to mention that besides the important conclusions, some future works can be suggested:

- investigation of the correlation between GW activity in vertical electric fields and Spread-F occurrence during summer days to confirm the hypothesis of event connection; and
- study of other planetary wave periodicities (different from 2-day wave) in the dynamo electric field and equatorial electrojet currents also including other techniques, e.g., ionosondes and radio occultation.

REFERENCES

ABDU, M. A.; DENARDINI, C. M.; SOBRAL, J. H. A.; BATISTA, I. S.; MURALIKRISHNA, P.; PAULA, E. R. de. Equatorial electrojet irregularities investigations using a 50 MHz back-scatter radar and digisonde at São Luís: some initial results. **Journal of Atmospheric and Solar-Terrestrial Physics**, v. 64, n. 12-14, p. 1425–1434, 2002. [44](#), [57](#)

ABDU, M. A.; DENARDINI, C. M.; SOBRAL, J. H. A.; BATISTA, I. S.; MURALIKRISHNA, P.; IYER, K. N.; VELIZ, O.; PAULA, E. R. de. Equatorial electrojet 3 m irregularity dynamics during magnetic disturbances over Brazil: results from the new VHF radar at São Luís. **Journal of Atmospheric and Solar-Terrestrial Physics**, v. 65, n. 14-15, p. 1293–1308, 2003. [38](#)

ABDU, M. A.; RAMKUMAR, T. K.; BATISTA, I. S.; BRUM, C. G. M.; TAKAHASHI, H.; REINISCH, B. W.; SOBRAL, J. H. A. Planetary wave signatures in the equatorial atmosphere-ionosphere system. **Journal of Atmospheric and Solar-Terrestrial Physics**, v. 68, n. 3-5, p. 509–522, 2006. [50](#), [52](#)

ANANDARAO, B. G. Effects of gravity wave winds and wind shears on equatorial electrojet. **Geophysical Research Letters**, v. 3, n. 9, p. 545–548, 1976. [45](#), [46](#)

ANANDARAO, B. G.; RAGHAVARAO, R.; DESAI, J. N.; HAERENDEL, G. Vertical winds and turbulence over Thumba. **Journal of Atmospheric and Terrestrial Physics**, v. 40, p. 157–163, 1978. [43](#), [85](#)

ANANDARAO, B. G.; RAGHAVARAO, R.; REDDY, C. R. Electric fields by gravity wave winds in the equatorial ionosphere. **Journal of Geophysical Research**, v. 82, p. 1510–1512, 1977. [47](#), [48](#), [49](#), [85](#)

ANDREWS, D. G.; HOLTON, J. R.; LEOVY, C. B. **Middle atmosphere dynamics**. New York: Academic Press, 1987. 489 p. [48](#)

BALSLEY, B. B. Some characteristics of non-two-stream irregularities in the equatorial electrojet. **Journal of Geophysical Research**, v. 74, p. 2333–2347, 1969. [38](#)

BANKS, P. M.; KOCKARTS, G. **Aeronomy - Part B**. London: Academic Press, 1973. 355 p. [30](#), [77](#)

BARD, Y. **Nonlinear parameter estimation**. New York: Academic Press, 1974. 341 p. ISBN 978-0120782505. [62](#)

BILITZA, D. International Reference Ionosphere 2000. **Radio Science**, v. 36, n. 2, p. 261–275, 2001. [77](#)

BLANC, M.; RICHMOND, A. D. The ionospheric disturbance dynamo. **Journal of Geophysical Research**, v. 85, n. A4, p. 1669–1686, 1980. [101](#)

BRASSEUR, G. P.; SOLOMON, S. **Aeronomy of the middle atmosphere - chemistry and physics of the stratosphere and mesosphere**. Dordrecht: Springer, 2005. 651 p. ISBN 978-1-4020-3824-1. [29](#), [30](#), [31](#), [43](#), [51](#)

BROCHET, P.; CROCHET, M.; GAGNEPAIN, J. Neutral winds and phase velocity of the instabilities in the equatorial electrojet. **Journal of Geophysical Research**, v. 83, p. 1145–1146, 1978. [36](#), [39](#), [40](#), [41](#)

BUNEMAN, O. Excitation of field aligned sound waves by electron streams. **Physical Review Letters**, v. 10, n. 7, p. 285–287, 1963. [36](#)

CAMPBELL, W. H. **Introduction to geomagnetic fields**. Cambridge: Cambridge University Press, 1997. 303 p. [65](#), [66](#)

CHEN, P. R. Two-day oscillations of the equatorial ionization anomaly. **Journal of Geophysical Research**, v. 979, n. A5, p. 6343–6357, 1992. [49](#)

COHEN, R. Phase velocities of irregularities in the equatorial electrojet. **Journal of Geophysical Research**, v. 78, n. 13, p. 2222–2231, 1973. [62](#)

COHEN, R.; BOWLES, K. L. Secondary irregularities in the equatorial electrojet. **Journal of Geophysical Research**, v. 72, p. 885–894, 1967. [38](#)

CRUZ, J. C.; TRUJILLO, H. Design of a fourth harmonic fluxgate magnetometer. **Sensors and Actuators**, v. 78, p. 71–73, 1999. [66](#)

DENARDINI, C. M. **Desenvolvimento de um sistema de correção de fase para o radar ionosférico de São Luís do Maranhão**. 137 p. Dissertação (Mestrado) — Instituto Nacional de Pesquisas Espaciais, São José dos Campos, 1999-03-12 1999. Disponível em: <http://urlib.net/sid.inpe.br/deise/1999/09.09.16.34>>. [38](#), [60](#), [61](#)

DENARDINI, C. M. **Estudo da eletrodinâmica da ionosfera equatorial durante o período de máxima atividade solar (1999–2002)**. 282 p. Tese (Doutorado) — Instituto Nacional de Pesquisas Espaciais, São José dos Campos, 2003–10–22 2003. Disponível em: <<http://urlib.net/sid.inpe.br/jeferson/2003/12.09.11.16>>. 32, 35, 36, 44, 45, 57

DENARDINI, C. M. A conductivity model for the Brazilian equatorial E-region: initial results. **Brazilian Journal of Geophysics**, v. 25, n. 2, p. 87–94, 2007. 91

DUHAU, S.; OSELLA, A. M. A correlation between measured E-region current and geomagnetic daily variation at equatorial latitudes. **Journal of Geomagnetism and Geoelectricity**, v. 34, p. 213–224, 1982. 94

FARGE, M. Wavelet transforms and their applications to turbulence. **Annual Review of Fluid Mechanics**, v. 24, n. 3, p. 395–457, 1992. 71, 73

FARLEY, D. T. A plasma instability resulting in field aligned irregularities in the ionosphere. **Journal of Geophysical Research**, v. 68, n. A22, p. 6083–6097, 1963. 36

FEJER, B. G.; KELLEY, M. C. Ionospheric irregularities. **Reviews of Geophysics and Space Physics**, v. 18, n. 2, p. 401–454, 1980. 38, 39

FORBES, J. M. The equatorial electrojet. **Reviews of Geophysics and Space Physics**, v. 19, n. 3, p. 469–504, 1981. 36, 43, 76

_____. Tidal and planetary waves. In: JOHNSON, R. M.; KILLEEN, T. L. (Ed.). **The upper mesosphere and lower thermosphere: a review of experiment and theory**. Washington DC: American Geophysical Union, 1995. p. 67–87. 50

_____. Planetary waves in the thermosphere-ionosphere system. **Journal of Geomagnetism and Geoelectricity**, v. 48, p. 91–98, 1996. 52, 55

_____. Wave coupling between the lower and upper atmosphere: case study of an ultra-fast Kelvin wave. **Journal of Atmospheric and Solar-Terrestrial Physics**, v. 62, p. 1603–1621, 2000. 51

FORBES, J. M.; HAGAN, M. E.; MIYAHARA, S.; VIAL, F.; MANSON, A. H.; MEEK, C. E.; PORTNYAGIN, Y. Quasi-16-day oscillation in the mesosphere and

lower thermosphere. **Journal of Geophysical Research**, v. 100, p. 9149–9161, 1995. [49](#)

FORBES, J. M.; LEVERONI, S. Quasi-16-day oscillation in the ionosphere. **Geophysical Research Letters**, v. 19, p. 981–984, 1992. [49](#)

FRITTS, D. C.; ALEXANDER, M. J. Gravity wave dynamics and effects in the middle atmosphere. **Reviews of Geophysics**, v. 41, n. 1, p. 1003, 2003. Doi:10.1029/2001RG000106. [43](#), [89](#)

GONZALEZ, W. D.; TSURUTANI, B. T.; GONZALEZ, A. L. C. de. Interplanetary origin of geomagnetic storms. **Space Science Reviews**, v. 88, p. 529–562, 1999. [70](#)

GURUBARAN, S.; RAMKUMAR, T. K.; SRIDHARAN, S.; RAJARAM, R. Signatures of quasi-2-day planetary waves in the equatorial electrojet: results from simultaneous observations of mesospheric winds and geomagnetic field variations at low latitudes. **Journal of Atmospheric and Solar-Terrestrial Physics**, v. 63, p. 813–821, 2001. [50](#)

HAGAN, M. E.; FORBES, J. M.; VIAL, F. Numerical investigation of the propagation of the quasi-two-day wave into the lower thermosphere. **Journal of Geophysical Research**, v. 98, n. D12, p. 23193–23205, 1993. [49](#)

HARGREAVES, J. K. **The solar-terrestrial environment**. Cambridge: Cambridge University Press, 1992. 434 p. ISBN 978-0521427371. [30](#), [37](#), [38](#)

HEELIS, R. A. Electrodynamics in the low and middle latitude ionosphere: a tutorial. **Journal of Atmospheric and Solar-Terrestrial Physics**, v. 66, p. 825–838, 2004. [32](#), [33](#)

HOLTON, J. R. Waves in the equatorial stratosphere generated by tropospheric heat sources. **Journal of Atmospheric Science**, v. 29, n. 2, p. 368–375, 2004. [48](#)

HORNE, J. H.; BALIUNAS, S. L. A prescription for period analysis of unevenly sampled time series. **The Astrophysical Journal**, v. 302, p. 757–763, 1986. [74](#)

JANARDHANAN, K. V. **A coherent VHF backscatter radar for INPE**. São José dos Campos: Instituto Nacional de Pesquisas Espaciais, 1983. 58 p. Disponível em: <<http://urlib.net/sid.inpe.br/iris@1905/2005/07.27.21.03.26>>. [58](#), [116](#)

- KATO, S. Electric field and wind motion at the magnetic equator. **Journal of Geophysical Research**, v. 78, p. 757–762, 1973. [47](#), [85](#)
- KELLEY, M. C. **The Earth's ionosphere - plasma physics and electrodynamics**. San Diego: Academic Press, 1989. 434 p. [76](#)
- KIVELSON, M. G.; RUSSEL, C. T. **Introduction to space physics**. Cambridge: Cambridge University Press, 1995. 568 p. [31](#)
- KOVALAM, S.; VINCENT, R. A.; LOVE, P. Gravity waves in the equatorial MLT region. **Journal of Atmospheric and Solar-Terrestrial Physics**, v. 68, p. 266–282, 2006. [89](#)
- LEVANON, N.; MOZESON, E. **Radar signals**. New Jersey: John Wiley & Sons, 2004. 427 p. [118](#), [119](#)
- LOMB, N. R. Least-squares frequency analysis of unequally spaced data. **Astrophysics and Space Science**, v. 39, p. 447–462, 1976. [73](#), [92](#)
- MACMILLAN, S.; MAUS, S. International Geomagnetic Reference Field: the tenth generation. **Earth Planets Space**, v. 57, n. 12, p. 1135–1140, 2005. [77](#)
- MAHAFZA, B. R. **Radar systems analysis and design using MatLab**. Boca Raton: CRC Press, 2000. 533 p. [119](#)
- MAHAFZA, B. R.; ELSHERBENI, Z. **MatLab simulations for radar systems design**. Boca Raton: CRC Press, 2004. 676 p. [117](#), [118](#)
- MEDEIROS, A. F.; TAKAHASHI, H.; BURITI, R. A.; FECHINE, J.; WRASSE, C. M.; GOBBI, D. MLT gravity wave climatology in the South America equatorial region observed by airglow imager. **Annales Geophysicae**, v. 25, p. 399–406, 2007. [87](#), [88](#)
- OLSEN, N. Geomagnetic tides and related phenomena. In: WILHELM, H.; ZURN, W.; WENZEL, H.-G. (Ed.). **Tidal phenomena**. [S.l.: s.n.], 1997. p. 261–274. [94](#)
- OYAMA, K. I. In situ measurements of Te in the lower ionosphere - a review. **Advances in Space Research**, v. 26, n. 8, p. 1231–1240, 2000. [76](#)
- OYAMA, K. I.; HIRAO, K.; BANKS, P. M.; WILLIAMSON, P. R. Is Te equal to Tn at the heights of 100 to 120 km? **Planetary Space Science**, v. 28, n. 3, p. 207–211, 1980. [76](#)

PANCHEVA, D. V.; MUKHTAROV, P. J.; MITCHELL, N. J.; FRITTS, D. C.; RIGGIN, D. M.; TAKAHASHI, H.; BATISTA, P. P.; CLEMESHA, B. R.; GURUBARAN, S.; RAMKUMAR, G. Planetary wave coupling (5-6-day waves) in the low latitude atmosphere-ionosphere system. **Journal of Atmospheric and Solar-Terrestrial Physics**, v. 70, p. 101–122, 2008. [48](#), [49](#)

PANCHEVA, D. V.; MUKHTAROV, P. J.; SHEPHERD, P. J.; MITCHELL, N. J.; FRITTS, D. C.; RIGGIN, D. M.; FRANKE, S. J.; BATISTA, P. P.; ABDU, M. A.; BATISTA, I. S.; CLEMESHA, B. R.; KIKUCHI, T. Two-day wave coupling of the low-latitude atmosphere-ionosphere system. **Journal of Geophysical Research**, v. 111, n. A7313, p. 101–122, 2006. [97](#), [100](#), [101](#)

PARISH, H. F.; FORBES, J. M.; KAMALABADI, F. Planetary waves and solar emission signals in the equatorial electrojet. **Journal of Geophysical Research**, v. 99, p. 355–368, 1994. [50](#), [53](#), [101](#)

PRAKASH, S. Production of electric field perturbations by gravity wave winds in the E region suitable for initiating equatorial spread F. **Journal of Geophysical Research**, v. 104, n. A5, p. 10051–10069, 1999. [88](#)

PRESS, W. H.; TEUKOLSKY, S. A.; VETTERLING, W. T.; FLANNERY, B. P. **Numerical recipes in C: the art of scientific computing**. Cambridge: Cambridge University Press, 1992. 994 p. [62](#)

REDDY, C. A. The equatorial electrojet: a review of the ionospheric and geomagnetic aspects. **Journal of Atmospheric and Terrestrial Physics**, v. 43, n. 5-6, p. 557–571, 1981. [43](#), [44](#)

REDDY, C. A.; DEVASIA, C. V. Short period fluctuations of the equatorial electrojet. **Nature**, v. 261, p. 396–397, 1976. [43](#), [85](#)

_____. Height and latitude structure of the electric fields and currents due to east-west winds in the equatorial electrojet. **Journal of Geophysical Research**, v. 86, n. A7, p. 5751–5767, 1981. [46](#)

RICHMOND, A. D. Equatorial electrojet I - development of a model including winds and instabilities. **Journal of Atmospheric and Terrestrial Physics**, v. 35, n. 6, p. 1083–1103, 1973. [40](#), [91](#)

RISHBETH, H. The ionospheric E-layer and F-layer dynamos - a tutorial review. **Journal of Atmospheric and Solar-Terrestrial Physics**, v. 59, p. 1873–1880, 1997. [33](#)

ROGISTER, A.; D'ANGELO, N. Type II irregularities in the equatorial electrojet. **Journal of Geophysical Research**, v. 75, p. 3879–3887, 1970. [36](#), [39](#)

ROSTOKER, G. Geomagnetic indices. **Reviews of Geophysics and Space Physics**, v. 10, p. 935–950, 1972. [69](#), [71](#)

SAMPATH, S.; SASTRY, T. S. G. Results from in situ measurements of ionospheric currents in the equatorial region. **Journal of Geomagnetism and Geoelectricity**, v. 31, p. 373–379, 1979. [94](#)

SAMPATH, S.; SASTRY, T. S. G.; OYAMA, K.; HIRAO, K. Joule heating due to the equatorial electrojet as observed by rocket-borne probes. **Space Research**, v. 14, p. 253–258, 1974. [77](#)

SATO, T. Neutral winds and electrojet irregularities. **Journal of Geophysical Research**, v. 80, n. 19, p. 2835–2838, 1975. [39](#), [41](#)

SCARGLE, J. D. Studies in astronomical time series analysis. II. Statistical aspects of spectral analysis of unevenly spaced data. **The Astrophysical Journal**, v. 263, p. 835–853, 1982. [73](#), [74](#), [92](#)

SCHLEGEL, K. Coherent backscatter from ionospheric E-region plasma irregularities. **Journal of Atmospheric and Terrestrial Physics**, v. 58, n. 8-9, p. 933–941, 1996. [37](#), [115](#), [116](#)

SKOLNIK, M. I. **Introduction to radar systems**. Singapore: McGraw-Hill Book Co., 1981. 581 p. [115](#), [119](#)

SPIRO, R. W.; WOLF, R. A.; FEJER, B. G. Penetration of high-latitude electric field effects to low latitudes during SUNDIAL 1984. **Annales Geophysicae**, v. 6, p. 39–50, 1988. [101](#)

TAKAHASHI, H.; WRASSE, C. M.; FECHINE, J.; PANCHEVA, D. V.; ABDU, M. A.; BATISTA, I. S.; LIMA, L. M.; BATISTA, P. P.; CLEMESHA, B. R.; SCHUCH, N. J.; SHIOKAWA, K.; GOBBI, D.; MLYNCZAK, M. G.; RUSSEL, J. M. Signatures of ultra fast Kelvin waves in the equatorial middle atmosphere and ionosphere. **Geophysical Research Letters**, v. 34, p. 11108, 2007. [51](#), [54](#)

TAKAHASHI, H.; WRASSE, C. M.; PANCHEVA, D. V.; ABDU, M. A.; BATISTA, I. S.; LIMA, L. M.; BATISTA, P. P.; CLEMESHA, B. R.; SHIOKAWA, K. Signatures of 3-6-day planetary waves in the equatorial mesosphere and ionosphere. **Annales Geophysicae**, v. 24, p. 3343–3350, 2006. [50](#)

TAYLOR, M. J.; JR., W. R. P.; CLARK, S.; TAKAHASHI, H.; GOBBI, D.; GOLDBERG, R. A. Image measurements of short-period gravity waves at equatorial latitudes. **Journal of Geophysical Research**, v. 102, n. D22, p. 26283–26299, 1997. [87](#), [88](#), [89](#)

TORRENCE, C.; COMPO, G. A practical guide to wavelet analysis. **Bulletin of the American Meteorological Society**, v. 79, p. 61–78, 1998. [71](#), [73](#)

VIKRAMKUMAR, B. T.; RAO, P. B.; VISWANATHAN, K. S.; REDDY, C. A. Electric fields and currents in the equatorial electrojet deduced from VHF radar observations - III. Comparison of observed ΔH values with those estimated from measured electric fields. **Journal of Atmospheric and Terrestrial Physics**, v. 49, n. 2, p. 201–207, 1987. [67](#), [92](#), [94](#)

A APPENDIX A - PRINCIPLES OF COHERENT BACKSCATTER RADARS

A.1 Radar Parameters

A.1.1 Radar Frequency

From the moment conservation of the incident wavevector \mathbf{k}_i , the scattered wavevector \mathbf{k}_s and the wavevector of the medium \mathbf{k}_{med}

$$\mathbf{k}_s = \mathbf{k}_i + \mathbf{k}_{med} \quad (\text{A.1})$$

follows the Bragg condition

$$\lambda_{Radar} = 2\lambda_{irr} \sin(\theta/2) \quad (\text{A.2})$$

if $|\mathbf{k}_i|=|\mathbf{k}_s|=2\pi/\lambda_{Radar}$, $|\mathbf{k}_{med}|=2\pi/\lambda_{irr}$ and θ is the scattering angle. For an ensemble of many scatterers with scale length λ (Figure A.1) this condition means a constructive interference leading to a maximal backscatter amplitude (SCHLEGEL, 1996). For monostatic backscatter radar ($\theta=180^\circ$), the radar wavelength λ_{Radar} is related to the scale size of the observed backscatterers by

$$\lambda_{irr} = \lambda_{Radar}/2. \quad (\text{A.3})$$

It means that a 50 MHz radar, which has $\lambda_{Radar} = 6$ m, observes 3-m scale irregularities.

The E-region plasma irregularities are generally elongated along the geomagnetic field \mathbf{B} , because of the much higher mobility of the electrons along B than in the other directions. It leads to the so-called aspect angle condition in the backscatter (SCHLEGEL, 1996): the radar line of sight has to be close to a direction normal to the field line. The deviation from perpendicularity is called the aspect angle α .

A.1.2 Pulse Width and Height Resolution

In a simple pulsed radar system, the signal-to-noise ratio of the reflected echo is proportional to the radar average power (SKOLNIK, 1981). The average power increases with the pulse width and with pulse repetition frequency for a given peak power. However, the pulse repetition frequency is limited, thus avoiding ambiguities of the

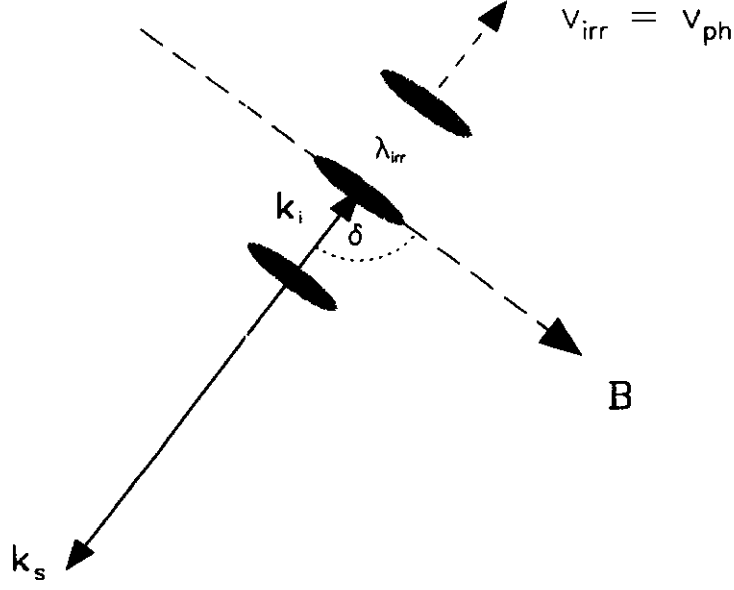


FIGURE A.1 - Sketch describing the radar backscatter from field-aligned plasma density irregularities (for a monostatic system), k_i and k_s denote the incident and scattered radar wave-vector, $\delta = 90 \pm \alpha$, where α is the aspect angle. λ_{irr} is the scale size of the irregularities.

SOURCE: [Schlegel \(1996\)](#).

measured height. Increasing the pulse width, the height resolution is worsened. In the case of oblique pointing beam, the height resolution shall be corrected by the beam elevating angle in relation to the zenith. In this way, the height resolution dh is given by ([JANARDHANAN, 1983](#)):

$$dh = \sin \theta \cdot \frac{c\tau}{2} + \frac{h}{\tan \theta} \cdot d\theta, \quad (\text{A.4})$$

where c is the speed of light (m/s), τ is the pulse width, θ is the elevation angle of the antenna beam axis, h is the height, and $d\theta$ is the antenna beamwidth. Generally, the second term of the equation, related to beamwidth problems, is neglected when calculating the height resolution.

A.1.3 Pulse Repetition Frequency and Range

The target's height, h , is computed by measuring the time delay, Δt , it takes a pulse to travel the two-way path between the radar and the target as given by

$$h = \frac{c\Delta t}{2} \cdot \sin \theta. \quad (\text{A.5})$$

In general, a pulsed radar transmits and receives a train of pulses, as illustrated by [Figure A.2](#). The Inter Pulse Period (*IPP*), often referred to as the Pulse Repetition Interval (*PRI*) is the inverse of the Pulse Repetition Frequency (*PRF*), which is denoted by f_r .

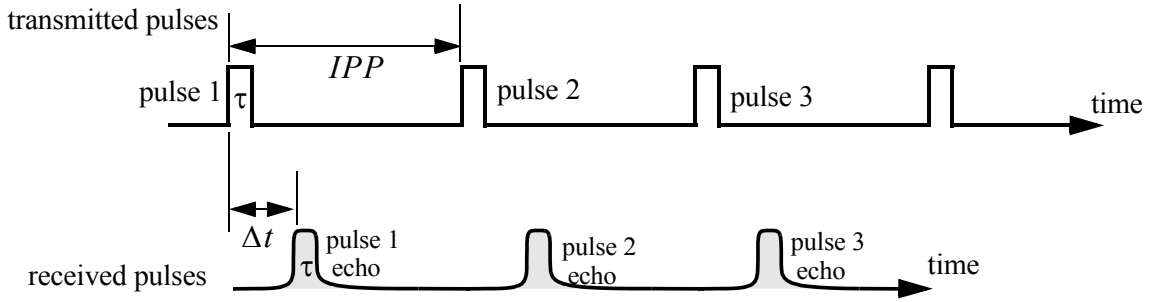


FIGURE A.2 - Train of transmitted and received pulses.

SOURCE: [Mahafza e Elsherbeni \(2004\)](#).

The range corresponding to the two-way time delay *IPP*, known as the radar unambiguous range, R_u , is given by:

$$R_u = \frac{c \cdot IPP}{2}. \quad (\text{A.6})$$

In [Figure A.3](#), echo 1 represents the radar return from a target at range $R_1 = c\delta/2$ due to pulse 1. Echo 2 could be identified as an return from pulse 1 or pulse 2. In this case ([MAHAFZA; ELSHERBENI, 2004](#)),

$$R_2 = \frac{c\Delta t}{2} \text{ or } R_2 = \frac{c(IPP + \Delta t)}{2}. \quad (\text{A.7})$$

A.2 Coherent Detection and Doppler Effect

Coherent radars are based on the concept of coherent detection. A stable frequency synthesizer provides the transmitter angular frequency ω_0 as well as reference signal for the receiver. The received signal can be expressed as

$$s(t) = g(t) \cdot \cos(\omega_0 t + \phi(t)) \quad (\text{A.8})$$

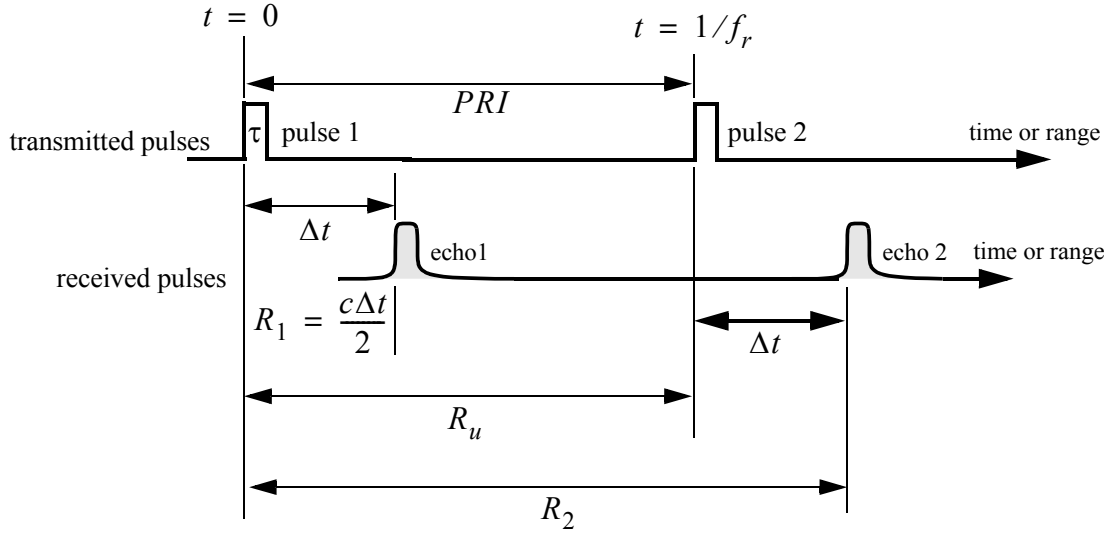


FIGURE A.3 - Illustrating range ambiguity.

SOURCE: [Mahafza e Elsherbeni \(2004\)](#).

where $g(t)$ is the natural envelope of $s(t)$ and $\phi(t)$ is the instantaneous phase. Another representation may be given by ([LEVANON; MOZESON, 2004](#))

$$s(t) = g_c \cdot \cos(\omega_0 t) - g_s \cdot \sin(\omega_0 t), \quad (\text{A.9})$$

where $g_c(t)$ and $g_s(t)$ are the *in-phase I* and *quadrature components Q* are given by

$$\begin{aligned} g_c(t) &= g(t) \cos \phi(t) \\ g_s(t) &= g(t) \sin \phi(t). \end{aligned} \quad (\text{A.10})$$

The signal $s(t)$ is divided in two parts and they are passed individually through a mixer and a low-pass filter (LPF). The output of the coherent detector, $g_s(t)$ and $g_c(t)$, that is the complex envelope of the signal $s(t)$, is defined as

$$u(t) = g_c(t) + jg_s(t) = g(t) \exp^{-j\phi(t)} \quad (\text{A.11})$$

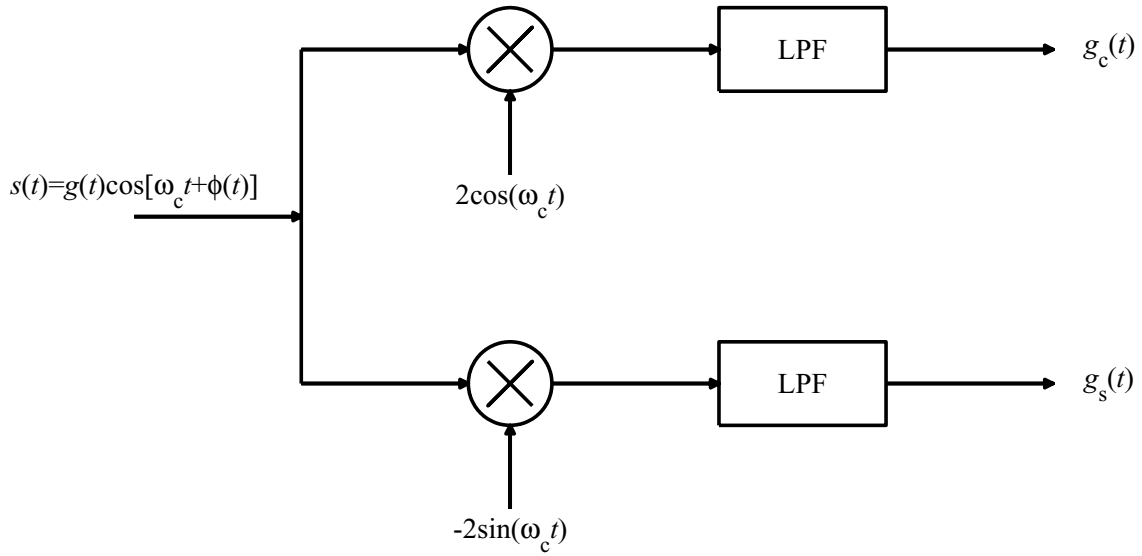


FIGURE A.4 - Coherent detector.

SOURCE: [Levanon e Mozeson \(2004\)](#).

The Doppler frequency shift is given by ([SKOLNIK, 1981](#))

$$f_d = \frac{2v_r}{\lambda_{\text{Radar}}} = \frac{2v_r f_0}{c}, \quad (\text{A.12})$$

where v_r is the relative (or radial) velocity of target with respect to radar, and f_0 is the radar transmitter frequency. Since $\phi(t)$ is given by

$$\phi(t) = 2\pi f_d t, \quad (\text{A.13})$$

then obtaining $\phi(t)$, the velocity of target can be determined. More precisely, the instantaneous Doppler frequency, f_{di} , is given by ([MAHAFZA, 2000](#))

$$f_{di} = \frac{1}{2\pi} \frac{d\phi(t)}{dt}. \quad (\text{A.14})$$

B APPENDIX B - CODES FOR WAVELET ANALYSIS OF MAGNETOMETER DATA (FOR WDC FOR GEOMAGNETISM - KYOTO DATA)

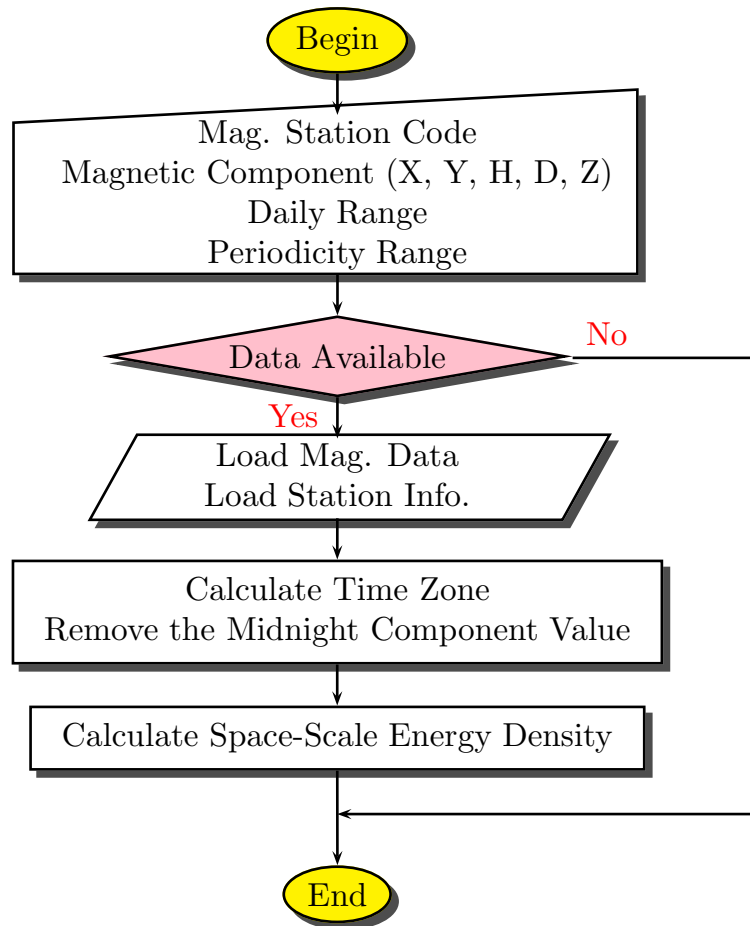


FIGURE B.1 - Flowchart of the program that calculates the Space-Scale Energy Density using the Morlet Wavelet-Mother from magnetometer data.

Code list:

- [PLANETARY WAVES_KYOTO_AMP_PS](#)
- [READ_MAGS_KYOTO](#)
- [MAG_KYOTO_CALIBRATION_EFFECT](#)
- [TIMEZONE](#)

```

PRO PLANETARY WAVES_KYOTO_AMP_PS,Txt_Data2Anal=Txt_Data2Anal, $
  IniPriod=IniPriod, EndPriod=EndPriod, AnalOptn=AnalOptn
;----- ABSTRACT
; This function calculates the Continuous Wavelet Tranform using
; Morlet Wavelet-Mother from magnetic data and plots the Space-Scale
; Energy Density to identify planetary waves signatures in the EEJ
; in .EPS file.
;----- CAPTION
;-----
; By:          Henrique C. Aveiro - aveiro@dae.inpe.br
; Date:        April 15, 2008
; Modification :
;-----

; Declares the constants and for the procedure ----- strings variables
;-----
IF (N_ELEMENTS(Txt_DrvLetter) EQ 0) THEN Txt_DrvLetter = 'E:\'
IF (N_ELEMENTS(Txt_IYYYYMMDD) EQ 0) THEN Txt_IYYYYMMDD = '20030101'
IF (N_ELEMENTS(Txt_EYYYYMMDD) EQ 0) THEN Txt_EYYYYMMDD = '20030228'
IF (N_ELEMENTS(Txt_GrapTitle) EQ 0) THEN Txt_GrapTitle = 'MAGNETOMETER DATA ANALYSIS'
IF (N_ELEMENTS(Txt_Data2Anal) EQ 0) THEN Txt_Data2Anal = 'AAE';'ASC';'PND';'TIR';'GUA';'BNG';
;----- control flags (0: OFF | 1: ON)
IF (N_ELEMENTS(Yes_SaveGraph) EQ 0) THEN Yes_SaveGraph = 0 ; save wavelet analysis to BMP
IF (N_ELEMENTS(Yes_Sav2ASCII) EQ 0) THEN Yes_Sav2ASCII = 0 ; save wavelet analysis to ASCII
IF (N_ELEMENTS(Yes_UsePaddng) EQ 0) THEN Yes_UsePaddng = 1 ; allow padding to wavelet analysis
IF (N_ELEMENTS(Yes_UseLogOpt) EQ 0) THEN Yes_UseLogOpt = 0 ; plot z-axis in log scale
IF (N_ELEMENTS(RmvMissingDat) EQ 0) THEN RmvMissingDat = 3 ; missing data to NAN (1), to Zero (2) or
IF (N_ELEMENTS(AnalOptn) EQ 0) THEN AnalOptn = 1 ; 0: analyse the amplitude; 1: analyse dh
;----- System variables (0: OFF | 1: ON)
IF (N_ELEMENTS(IniPriod) EQ 0) THEN IniPriod = 0.4;0.90;
IF (N_ELEMENTS(EndPriod) EQ 0) THEN EndPriod = 0.6;1.15;

; Create paths strings to the header, binary, images and parameters -----
Txt_PathToMag = Txt_DrvLetter+'\Magnetometer\Kyoto\Raw Data\'+'Txt_Data2Anal+'_98-07'
Txt_PathToImg = Txt_DrvLetter+'\Magnetometer\Kyoto\Images\'+'Txt_Data2Anal
Txt_PathToPar = Txt_DrvLetter+'\Magnetometer\Kyoto\Parameters\'+'Txt_Data2Anal

; Open the file and load the matrix -----
MONTH = FIX([STRMID(Txt_IYYYYMMDD, 4, 2), STRMID(Txt_EYYYYMMDD, 4, 2)])
DAY = FIX([STRMID(Txt_IYYYYMMDD, 6, 2), STRMID(Txt_EYYYYMMDD, 6, 2)])
YEAR = FIX([STRMID(Txt_IYYYYMMDD, 0, 4), STRMID(Txt_EYYYYMMDD, 0, 4)])

DummyOpn = Read_Mags_Kyoto(Txt_PathToMag+'.dat', $
  I_JulDay=JULDAY(MONTH[0],DAY[0], YEAR[0],0.), $
  E_JulDay=JULDAY(MONTH[1],DAY[1]+1,YEAR[1],0.), $
  Flag=0, RmvClbtnEffct=1)

TimSerie = SQRT(FLOAT(DummyOpn.X)^2+FLOAT(DummyOpn.Y)^2)
Axistime = DummyOpn.DATE
Delta_dt = 1./24
NRawFile = N_ELEMENTS(TimSerie)

; Eliminates missing data to avoid errors in Wavelet Transform -----
IF KEYWORD_SET(RmvMissingDat) THEN BEGIN
  Positions = WHERE((TimSerie EQ 9999) OR (FINITE(TimSerie) EQ 0))
  IF (Positions[0] NE -1) THEN $
    CASE RmvMissingDat OF
      1: TimSerie[Positions] = !VALUES.F_NAN
      2: TimSerie[Positions] = 0.
      3: FOR II=0, N_ELEMENTS(Positions)-1 DO $
          TimSerie[Positions[II]] = TimSerie[Positions[II]-1]
    ENDCASE
  ENDDIF

ENDIF

; Set the wavelet variables -----
Scale_s0 = 0.500000/2 ;=2 * Delta_dt(general) ; the initial scale (=s0)
Delta_dj = 0.125000 ; this will do 8 sub-octaves per octave (=dj)
J_Powers = 4./Delta_dj ; this says do 4 powers-of-two with dj sub-octaves each (jl)
WavMothr = 'Morlet' ; choose Morlet as wavelet-mother

; Redo the analysis -----
AGAIN:

; Normalize by standard deviation, save an extra copy of the -----
; original series and determine if the data quality is good -----
NorSerie = (TimSerie - TOTAL(TimSerie,/NAN)/NRawFile)
ReconSer = NorSerie

; Wavelet transform -----
WaveAnal = WAVELET(ReconSer,Delta_dt,PERIOD=WavPriod,SCALE=WavScale,S0=Scale_s0, $
  PAD=Yes_UsePaddng,COI=Cone_Inf,DJ=Delta_dj,J=J_Powers,MOTHER=WavMothr)

WaveSpec = (ABS(WaveAnal))^2 ; compute wavelet power spectrum
J_Scales = N_ELEMENTS(WavScale) - 1
ScaleAvg = REBIN(TRANPOSE(WavScale),NRawFile,J_Scales+1) ; expand scale-->(J+1)x(NRawFile) array

```

```

Pow_Norm = WaveSpec/ScaleAvg
C_delta = 0.776 ; reconstruction factor
GlobalWS = TOTAL(Pow_Norm,1)/NRawFile ; global wavelet spectrum (GWS)

IF (AnalOptn EQ 0) THEN BEGIN
  Psi0 = (!DPI)^(-0.25)
  ScaleRng = WHERE((WavPriod GE IniPriod) AND (WavPriod LE EndPriod))
  TimSerie = SQRT(Delta dj*Delta dt/C delta*TOTAL(Pow_Norm(*,ScaleRng),2)) ; Average Scale Varia
  ;TimSerie = Delta dj*SQRT(Delta dt)/(C delta*Psi0)*(FLOAT(WaveAnal[*],ScaleRng]) # (1./SQRT(WavSca
  Scale_s0 = 1.000000 ;=2 * Delta_dt(general) ; the initial scale (=s0)
  Delta_dj = 0.125000 ; this will do 8 sub-octaves per octave (=dj)
  J_Powers = 3./Delta_dj ; this says do 4 powers-of-two with dj sub-octaves each (j1)
  AnalOptn = 1
  GOTO, Again
ENDIF

; This part sets the device to plot in PS format -----
P_S_F_Name = Txt_PathToImg+'_dH.EPS' ; sets Post Script file name

XTickLen = 0.100
YTickLen = 0.025
Txt_Size = 1.000
Txt_Thick = 2.500
Trc_Thick = 2.500

V_PageSize = 04.0 ; sets vertical page size [cm]
H_PageSize = 12.0 ; sets horizontal page size [cm]
VPagOffset = 02.0 ; sets vertical page offset [cm]
HPagOffset = 02.0 ; sets horizontal page offset [cm]
Resolution = 08.0 ; image resolution [Bits per Pixel]
LetterSize = 12.0 ; size of the fonts

SET_PLOT, 'PS' ; set device to Post Script
DEVICE, XSIZE=H_PageSize, YSIZE=V_PageSize, XOFFSET=HPagOffset, YOFFSET=VPagOffset, $
BITS_PER_PIXEL=Resolution, /COLOR, SET_FONT='Helvetica', /TT_FONT, FONT_SIZE=LetterSize, $
FILENAME=P_S_F_Name ,ENCAPSULATED=1

; Set graphics variables and plot the graph -----
Dummy = LABEL_DATE (DATE_FORMAT='%D %M') ; set time label format
My_Color_Table_PS ; uses my color table
PositVct = [0.10,0.40,0.87,0.90]

WvPriod2 = FIX(ALOG(WavPriod)/ALOG(2)) ; integer powers of 2 in period
YPlotRng = [MAX(WavPriod),MIN(WavPriod)] ; sets the x axis plot range
Y_Tick_V = 2.^(WvPriod2(UNIQU(WvPriod2))) ; unique powers of 2

Pow_Norm = ALOG10(Pow_Norm)
Zmin = 2.;0.5;0
Zmax = 5.;3.0;4;MAX(Pow_Norm,/NAN);

ColorVct = (255./30)*FINDGEN(30)
ColorVct[0] = 255
ColorVct[29] = 0

NBarTick = 5. ; tick in the bar
CBarTick = STRING(Zmin + (FINDGEN(NBarTick+1)/NBarTick)*(Zmax-Zmin), FORMAT='(e8.1)')

FOR JJ=0, NBarTick DO BEGIN
  A = CBarTick[JJ]
  IF (STRPOS(A, "+000") GE 0) THEN $
    STRPUT, A, " +0", (STRPOS(A, "+000"))
  IF (STRPOS(A, "+00") GE 0) THEN $
    STRPUT, A, " +", (STRPOS(A, "+00"))
  IF (STRPOS(A, "+0") GE 0) THEN $
    STRPUT, A, " +", (STRPOS(A, "+0"))
  IF (STRPOS(A, "-000") GE 0) THEN $
    STRPUT, A, " -0", (STRPOS(A, "-000"))
  IF (STRPOS(A, "-00") GE 0) THEN $
    STRPUT, A, " -", (STRPOS(A, "-00"))
  IF (STRPOS(A, "-0") GE 0) THEN $
    STRPUT, A, " -", (STRPOS(A, "-0"))
  CBarTick[JJ]=STRCOMPRESS(A,/REMOVE_ALL)
ENDFOR

CONTOUR, Pow_Norm, Axistime, WavPriod, $
NLEVEL=30,/FILL, C_COLORS = ColorVct, $
YMINOR=1,XTICKINTERVAL=15,XMINOR=15, $
XTITLE='Time (days)',YTITLE='Period (days)', $
XTICKUNITS='Days', XTICKFORMAT='LABEL_DATE', $
YTICKS=N_ELEMENTS(Y_Tick_V)-1,YTICKV=Y_Tick_V, $
YRANGE=YPlotRng,/YTYPE, CHARTHICK=Txt_Thick, $ ;POSITION=PositVct,
XSTYLE=1, CHARSIZE=Txt_Size, ZRANGE=[Zmin,Zmax],$
XTICKLEN=XTickLen, YTICKLEN=YTickLen

PLOTS, Axistime, (Axistime*0+2.),LINESTYLE=2, /NOCLIP

```

```

COI_XPos = [Axistime(0),Axistime,MAX(Axistime)]
COI_YPos = [MAX(WavPriod),Cone_Inf,MAX(WavPriod)]
POLYFILL,COI_XPos,COI_YPos,ORIEN=+45,SPACING=0.5,NOCLIP=0,THICK=1
POLYFILL,COI_XPos,COI_YPos,ORIEN=-45,SPACING=0.5,NOCLIP=0,THICK=1
PLOTS,Axistime,Cone_Inf,NOCLIP=0,THICK=1

;BarPosit = [PositVct[2]+0.01,PositVct[1],PositVct[2]+0.03,PositVct[3]]
;COLORBAR, DIVISIONS=NBarTick, charsize=Txt_Size,$
;TITLE=ClrBrTit,/vertical,/right,POSITION=BarPosit,TICKNAMES=CBarTick

DEVICE, /CLOSE_FILE
SET_PLOT, 'WIN'
!P.MULTI=0

END

```

```

FUNCTION Read_Mags_Kyoto, Path, I_JulDay=I_JulDay, E_JulDay=E_JulDay, $
    Flag=Flag, RmvClbtnEffect=RmvClbtnEffect
;----- ABSTRACT
; This function opens and loads the magnetic data. It returns one
; structure having the time of acquisition and the desired magnetic
; components according the Flag option.
;----- CAPTION
; Path          complete path to the magnetic data file
; I_JulDay      initial julian day to process
; E_JulDay      final julian day to process
; Flag          desired magnetic component [0:All, 1:X, 2:Y, 3:Z]
; RmvClbtnEffect remove the local midnight value of the data set
;-----
; By:           Henrique C. Aveiro - aveiro@dae.inpe.br
; Date:         March 20, 2008
; Modification :
;-----

; Verifie constants and flags needed for this routine -----
IF (N_ELEMENTS(Path) EQ 0) THEN STOP ; complete path
IF (N_ELEMENTS(I_JulDay) EQ 0) THEN STOP ; initial day
IF (N_ELEMENTS(E_JulDay) EQ 0) THEN STOP ; final day
IF (N_ELEMENTS(Flag) EQ 0) THEN Flag = 0 ; [0:All, 1:X, 2:Y, 3:Z]
IF ((Flag LT 0) OR (Flag GT 3)) THEN Flag = 0 ; constraint flag
IF (N_ELEMENTS(RmvClbtnEffect) EQ 0) THEN RmvClbtnEffect = 1 ; remove midnight value

; load the templates to open the files-----

VERSION = 1.00000
DATASTART = LONG(0)
DELIMITER = BYTE(0)
MISSINGVALUE = FIX(9999)
COMMENTSymbOL = ''
FIELDSCOUNT = LONG(32)
FIELDTYPES = INTARR(32) ; 7 -> STRING ... 3 -> INTEGER
    FIELDTYPES[0] = 7 ; Observatory 3-letter code
    FIELDTYPES[1] = 3 ; Year (last 2 digits, 82 = 1982)
    FIELDTYPES[2] = 3 ; Month (01-12)
    FIELDTYPES[3] = 7 ; Element (D, H, X, Y, Z or F)
    FIELDTYPES[4] = 3 ; Day of Month (01-31)
    FIELDTYPES[5] = 7 ; Blanks, Arbitrary, International Quiet
    ; or Disturbed Days, and Blank
    FIELDTYPES[6] = 3 ; Tabular base in degrees for D and I,
    ; hundreds of nanoTeslas for the intensity
    ; elements
    FIELDTYPES[7:31] = 3 ; From TAB_BASE to DAYLY_MEAN

FIELDNAMES = ['OBS', 'YEAR', 'MONTH', 'COMP', 'DAY', 'BLANKS', 'TAB_BASE', $
    'H00', 'H01', 'H02', 'H03', 'H04', 'H05', 'H06', 'H07', 'H08', 'H09', 'H10', 'H11', $
    'H12', 'H13', 'H14', 'H15', 'H16', 'H17', 'H18', 'H19', 'H20', 'H21', 'H22', 'H23', $
    'DAYLY_MEAN']

FIELDLOCATIONS = LONG([0,3,5,7,8,10,16,20,24,28,32,36,40,44,48,52,56,60,64, $
    68,72,76,80,84,88,92,96,100,104,108,112,116])
FIELDGROUPS = INDGEN(32)

MyTemplate={VERSION:VERSION,DATASTART:DATASTART,DELIMITER:DELIMITER,$
    MISSINGVALUE:MISSINGVALUE,COMMENTSymbOL:COMMENTSymbOL, $
    FIELDSCOUNT:FIELDSCOUNT,FIELDTYPES:FIELDTYPES,FIELDNAMES:FIELDNAMES, $
    FIELDLOCATIONS:FIELDLOCATIONS,FIELDGROUPS:FIELDGROUPS}

; Load using template and transfer parameters to the appropriated vector --
Reader = READ_ASCII(Path, TEMPLATE=MyTemplate)
ArrSize = N_ELEMENTS(Reader.OBS)

H_Count = 0
D_Count = 0
Z_Count = 0
X_Count = 0
Y_Count = 0

FOR II=0L, ArrSize-1, 1 DO BEGIN

    Data_Tmp = [Reader.H00[II], Reader.H01[II], Reader.H02[II], $
        Reader.H03[II], Reader.H04[II], Reader.H05[II], $
        Reader.H06[II], Reader.H07[II], Reader.H08[II], $
        Reader.H09[II], Reader.H10[II], Reader.H11[II], $
        Reader.H12[II], Reader.H13[II], Reader.H14[II], $
        Reader.H15[II], Reader.H16[II], Reader.H17[II], $
        Reader.H18[II], Reader.H19[II], Reader.H20[II], $
        Reader.H21[II], Reader.H22[II], Reader.H23[II]]

    Data_Tmp = FLOAT(Data_Tmp)
    Idx2Chng = WHERE(Data_Tmp EQ 9999.) ; eliminates missing data
    IF (Idx2Chng[0] NE -1) THEN Data_Tmp[Idx2Chng] = !VALUES.F_NAN

```

```

CASE (STRUPCASE(Reader.COMP[II])) OF
'H': BEGIN
    H_Tmp = FLOAT(Reader.TAB_BASE[II]*100+Data_Tmp)
    H     = (H_Count EQ 0) ? H_Tmp : [H, H_Tmp]
    H_Count++
    END
'D': BEGIN
    D_Tmp = !DTOR*(FLOAT(Reader.TAB_BASE[II]) + Data_Tmp/600.)
    D     = (D_Count EQ 0) ? D_Tmp : [D, D_Tmp]
    D_Count++
    END
'Z': BEGIN
    Z_Tmp = FLOAT(Reader.TAB_BASE[II]*100+Data_Tmp)
    Z     = (Z_Count EQ 0) ? Z_Tmp : [Z, Z_Tmp]

    ; Saves the time in julian format -----
    Year_Crct = (Reader.YEAR[II] LT 20) ? Reader.YEAR[II]+2000 : Reader.YEAR[II]+1900
    Date_Tmp = JULDAY(Reader.MONTH[II],Reader.DAY[II],Year_Crct,INDGEN(24))
    Date     = (Z_Count EQ 0) ? Date_Tmp : [Date, Date_Tmp]

    Z_Count++
    END
'X': BEGIN
    X_Tmp = FLOAT(Reader.TAB_BASE[II]*100+Data_Tmp)
    X     = (X_Count EQ 0) ? X_Tmp : [X, X_Tmp]
    X_Count++
    END
'Y': BEGIN
    Y_Tmp = FLOAT(Reader.TAB_BASE[II]*100+Data_Tmp)
    Y     = (Y_Count EQ 0) ? Y_Tmp : [Y, Y_Tmp]
    Y_Count++
    END
ELSE: BEGIN PRINT, 'DATA IS NOT IN HDZ OR XYZ FORMAT' & STOP & END
ENDCASE
ENDFOR
; Constraint data vector according user definition -----
IdxBHs = WHERE(Date GE I_JulDay) ; get superior indices
IF (IdxBHs[0] NE -1) THEN BEGIN ; constraint to them
    Date = Date[IdxBHs]
    Z     = Z[IdxBHs]
    IF (H_Count NE 0) THEN BEGIN
        H = H[IdxBHs]
        D = D[IdxBHs]
    ENDIF ELSE BEGIN
        X = X[IdxBHs]
        Y = Y[IdxBHs]
    ENDELSE
ENDIF
IdxEHs = WHERE(Date LT E_JulDay) ; get inferior indices
IF (IdxEHs[0] NE -1) THEN BEGIN ; constraint to them
    Date = Date[IdxEHs]
    Z     = Z[IdxEHs]
    IF (H_Count NE 0) THEN BEGIN
        H = H[IdxEHs]
        D = D[IdxEHs]
    ENDIF ELSE BEGIN
        X = X[IdxEHs]
        Y = Y[IdxEHs]
    ENDELSE
ENDIF
ENDIF

; Converts the data set to HDZ floating-point format and -----
; --- removes the calibration effect (if selected) -----
IF (RmvClbtnEffect) THEN BEGIN
    Txt_FileName = STRMID(Path,0,2)+'\Magnetometer\Kyoto\Informations\Stations_List'
    LOAD_STATION_INFORMATIONS,  Filename = Txt_FileName, $
    SttnCode = StTxtCod, SttnLong = StFltLon, $
    ASCIIIOpt = 0, Yes_Save_List=0
    NrOfSttn = N_ELEMENTS(StFltLon)
    ObsLngtd = StFltLon(WHERE(STRMATCH(StTxtCod, Reader.OBS[0],/FOLD_CASE) EQ 1))
    TimZonFl = TIMEZONE(ObsLngtd)
    Z         = MAG_KYOTO_CALIBRATION_EFFECT(Date, Z, TimZonFl[0])
    IF (H_Count EQ 0) THEN BEGIN
        X     = MAG_KYOTO_CALIBRATION_EFFECT(Date, X, TimZonFl[0])
        Y     = MAG_KYOTO_CALIBRATION_EFFECT(Date, Y, TimZonFl[0])
    ENDIF ELSE BEGIN
        X     = MAG_KYOTO_CALIBRATION_EFFECT(Date, H*COS(D), TimZonFl[0])
        Y     = MAG_KYOTO_CALIBRATION_EFFECT(Date, H*SIN(D), TimZonFl[0])
    ENDELSE
ENDIF ELSE BEGIN
    X     = H*COS(D)
    Y     = H*SIN(D)
ENDELSE

; D-Component -> radians
; H-Component -> hundreds of nT

```



```

; X-Component -> hundreds of nT
; Y-Component -> hundreds of nT
; Z-Component -> hundreds of nT

; Select the data to be returned according the Flag option -----
CASE (Flag) OF
  0: RetVct = {Date:Date, X:X, Y:Y, Z:Z}      ; select the components
                                           ; picks all up
  1: RetVct = {Date:Date, X:X}              ; picks date and X up
  2: RetVct = {Date:Date, Y:Y}              ; picks date and Y up
  3: RetVct = {Date:Date, Z:Z}              ; picks date and Z up
ENDCASE

; -----
Return, RetVct                               ; returns data
END                                           ; end of procedure

```

```

FUNCTION MAG_Kyoto_Calibration_Effect, TimeVec, DataVec, TimZone
;----- ABSTRACT
;   This function cuts off the effects of calibration in the
; magnetometers and returns this new values.
;----- CAPTION
; TimeVec      universal time of data acquisition [Julian Days]
; DataVec      original data vector to remove calibrations [nT]
; TimZone      time zone of the observatory that acquired the data set [h]
;-----
; By:          Henrique C. Aveiro - aveiro@dae.inpe.br
; Date:        March 28, 2008
; Modification :
;-----

; Verifie constants and flags needed for this routine -----
IF (N_ELEMENTS(TimeVec) EQ 0) THEN STOP           ; time vector
IF (N_ELEMENTS(DataVec) EQ 0) THEN STOP           ; data vector
IF (N_ELEMENTS(TimZone) EQ 0) THEN STOP           ; method choosen

; Set time axis to gregorian calendar -----
CALDAT, TimeVec, Month, Day, Year, Hour           ; Julian to Gregorian

LMdNight = (TimZone[0] LE 0) ? (-TimZone[0]) : (24-TimZone[0])

; Cut off the calibration effect -----
ZHIndex = WHERE(Hour EQ LMdNight)                 ; midnight @ GMT TimZone
LastVal = DataVec[MAX(ZHIndex)]                   ; store the last midnight

FOR II=0L, N_ELEMENTS(ZHIndex)-1 DO BEGIN         ; suppress from each day
  Pos2Crct = -INDGEN(24)+ZHIndex[II]
  Pos2Crct = Pos2Crct(WHERE(Pos2Crct GE 0))
  DataVec[Pos2Crct] = DataVec[Pos2Crct]-DataVec[ZHIndex[II]];supress
ENDFOR

; Cut off the calibration effect of the last values -----
ResidIdx = N_ELEMENTS(DataVec) - MAX(ZHIndex) - 1
IF (ResidIdx GT 0) THEN BEGIN
  Pos2Crct2 = INDGEN(ResidIdx) + MAX(ZHIndex) + 1
  DataVec[Pos2Crct2] = DataVec[Pos2Crct2]-LastVal ; supress
ENDIF

; -----
Return, DataVec                                  ; returns vector
END                                               ; end of function

```

```

FUNCTION TimeZone, Latitude
;----- ABSTRACT
;       This function returns the time zone of a given latitude.
;----- CAPTION
; Latitude      latitude of the observatory
;-----
; By:           Henrique C. Aveiro - aveiro@dae.inpe.br
; Date:         March 27, 2008
; Modification: DATA (E-MAIL -> WHAT CHANGED)
;-----

; Check variable and initial definition -----
IF (N_ELEMENTS(Latitude) EQ 0) THEN STOP      ; check latitude presence

; TZ -> LATITUDE RANGE -----
;
;-11 -> [-172.5,-157.5]
;-10 -> [-157.5,-142.5]
;-09 -> [-142.5,-127.5]
;-08 -> [-127.5,-112.5]
;-07 -> [-112.5,-097.5]
;-06 -> [-097.5,-082.5]
;-05 -> [-082.5,-067.5]
;-04 -> [-067.5,-052.5]
;-03 -> [-052.5,-037.5]
;-02 -> [-037.5,-022.5]
;-01 -> [-022.5,-007.5]
;+00 -> [-007.5,+007.5]
;+01 -> [+007.5,+022.5]
;+02 -> [+022.5,+037.5]
;+03 -> [+037.5,+052.5]
;+04 -> [+052.5,+067.5]
;+05 -> [+067.5,+082.5]
;+06 -> [+082.5,+097.5]
;+07 -> [+097.5,+112.5]
;+08 -> [+112.5,+127.5]
;+09 -> [+127.5,+142.5]
;+10 -> [+142.5,+157.5]
;+11 -> [+157.5,+172.5]
;+12 -> [+172.5,+180.0] OR [-180.0,-172.5]
;-----

IF ((Latitude GE 172.5) OR (Latitude LE -172.5)) THEN BEGIN TimZonVl=+12
ENDIF ELSE BEGIN      TimZonVl = FIX((-7.5+Latitude)/15.)
                     IF (Latitude GE 7.5) THEN TimZonVl++
ENDELSE
;-----
RETURN, TimZonVl      ; return time zone
END                  ; end of function

```


C APPENDIX C - CODES FOR WAVELET ANALYSIS OF MAGNETIC INDICES

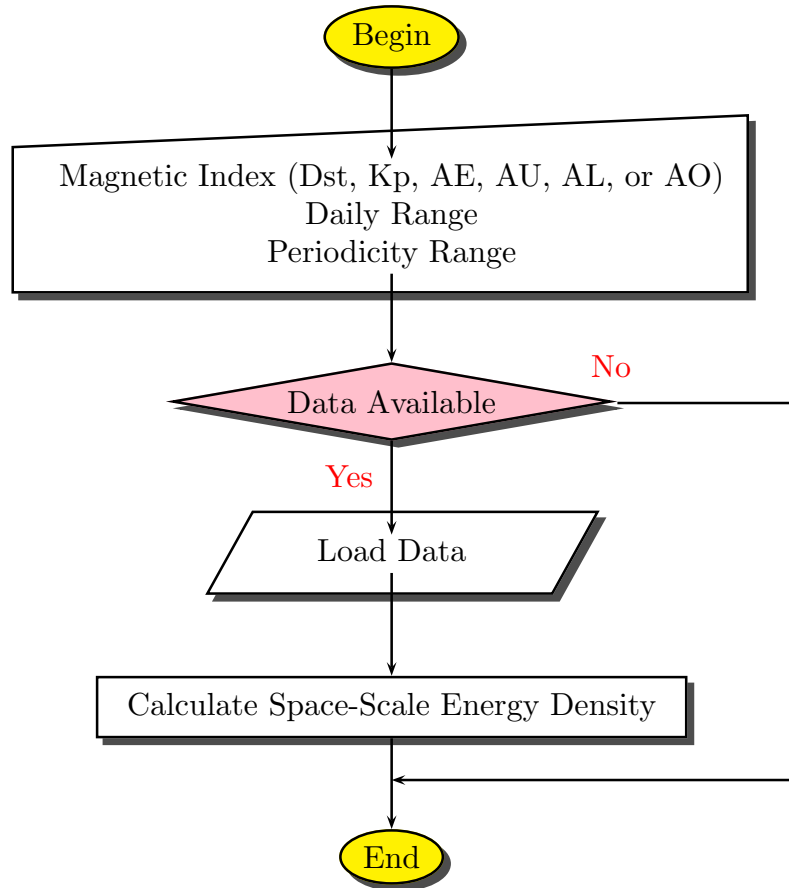


FIGURE C.1 - Flowchart of the program that calculates the Space-Scale Energy Density using the Morlet Wavelet-Mother from Magnetic Indices.

Code list:

- [MAGNETIC_INDICES_ANALYSIS_PS](#)
- [AURORAL_INDEX](#)
- [DST_INDEX](#)
- [KP_INDEX](#)
- [WVLT_MAGNETIC_IDX](#)

```

PRO Magnetic_Indices_Analysis_PS
;----- ABSTRACT
; This procedure is a routine that open, wavelet analyze and
; plot magnetic indices: Dst, Kp, AE, AU and AL.
;----- CAPTION
;
;-----
; By: Henrique C. Aveiro - aveiro@dae.inpe.br
; Date: July 22, 2008
; Modification :
;-----

; Declares the constants and for the procedure -----
;----- strings variables
IF (N_ELEMENTS(Txt_DrvLetter) EQ 0) THEN Txt_DrvLetter = 'D:'
IF (N_ELEMENTS(Txt_Year2Proc) EQ 0) THEN Txt_Year2Proc = '2003'
IF (N_ELEMENTS(Txt_Month_Ini) EQ 0) THEN Txt_Month_Ini = '10'
IF (N_ELEMENTS(Txt_Month_End) EQ 0) THEN Txt_Month_End = '10'
;----- indices control flags (0: OFF | 1: ON)
IF (N_ELEMENTS(Ds_Slct) EQ 0) THEN Ds_Slct = 0
IF (N_ELEMENTS(Kp_Slct) EQ 0) THEN Kp_Slct = 0
IF (N_ELEMENTS(AE_Slct) EQ 0) THEN AE_Slct = 0
IF (N_ELEMENTS(AU_Slct) EQ 0) THEN AU_Slct = 0
IF (N_ELEMENTS(AL_Slct) EQ 0) THEN AL_Slct = 0
IF (N_ELEMENTS(AO_Slct) EQ 0) THEN AO_Slct = 1
IF (N_ELEMENTS(PltType) EQ 0) THEN PltType = 0 ;0-Time Series, 1-Scalogram, 2-Avg Scale
IF (N_ELEMENTS(IniPriod) EQ 0) THEN IniPriod = 1.80
IF (N_ELEMENTS(EndPriod) EQ 0) THEN EndPriod = 2.20
;-----

; the program starts here -----

DayIni = JULIAN_DAY(FIX(Txt_Year2Proc), FIX(Txt_Month_Ini), 1)
DayEnd = JULIAN_DAY(FIX(Txt_Year2Proc), FIX(Txt_Month_End)+1, 1)-1
Axistime = JULDAY(FIX(Txt_Month_Ini), 1, FIX(Txt_Year2Proc), FINDGEN(24*(DayEnd-DayIni+1)), 0, 0)
AxsTimKp = JULDAY(FIX(Txt_Month_Ini), 1, FIX(Txt_Year2Proc), 3*FINDGEN(8*(DayEnd-DayIni+1)), 0, 0)

IF (Ds_Slct) THEN Dst_Data = Dst_Index_New(Txt_DrvLetter,Txt_Year2Proc,Txt_Month_Ini,Txt_Month_End)
IF (Kp_Slct) THEN Kp_Data = Kp_Index_New(Txt_DrvLetter,Txt_Year2Proc,Txt_Month_Ini,Txt_Month_End)
IF ((AE_Slct+AU_Slct+AL_Slct+AO_Slct) GT 0) THEN $
    Aur_Data = Auroral_Index_New(Txt_DrvLetter,Txt_Year2Proc,Txt_Month_Ini,Txt_Month_End)

; This part sets the device to plot in PS format -----
CASE PltType OF
    0: Txt_Plot_Typ = 'TmSr'
    1: Txt_Plot_Typ = 'Wvlt'
    2: Txt_Plot_Typ = 'AvgV'
ENDCASE

P_S_F_Name = Txt_DrvLetter+'\Dados Geofisicos\Magnetic Indices\Images\'+$
            Txt_Plot_Typ+Txt_Year2Proc + '+'Txt_Month_Ini+'-'+Txt_Month_End+'.EPS' ; sets Post Script file n.
My_Color_Table_PS ; uses my color table

XTickLen = 0.100
YTickLen = 0.025
Txt_Size = 1.000
Txt_Thick = 2.500
Trc_Thick = 2.500

V_PageSize = 06.0 ;04 for articles ; sets vertical page size [cm]
H_PageSize = 12.0 ; sets horizontal page size [cm]
VPagOffset = 02.0 ; sets vertical page offset [cm]
HPagOffset = 02.0 ; sets horizontal page offset [cm]
Resolution = 08.0 ; image resolution [Bits per Pixel]
LetterSize = 12.0 ; size of the fonts

SET_PLOT, 'PS' ; set device to Post Script
DEVICE, XSIZE=H_PageSize, YSIZE=V_PageSize, XOFFSET=HPagOffset, YOFFSET=VPagOffset, $
        BITS_PER_PIXEL=Resolution, /COLOR, SET_FONT='Helvetica', /TT_FONT, FONT_SIZE=LetterSize, $
        FILENAME=P_S_F_Name ,ENCAPSULATED=1

; Set graphics variables and plot the graph -----
IdxSlc = [Ds_Slct,Kp_Slct,AE_Slct,AU_Slct,AL_Slct,AO_Slct]
IF (TOTAL(IdxSlc) NE 1) THEN STOP
Dummy = LABEL_DATE(DATE_FORMAT='%D %M') ; set time label format

FOR II=0, 5 DO $
    IF (IdxSlc[II] EQ 1) THEN BEGIN
        VertStyl = 0
        ActPstn = (TOTAL(IdxSlc[0:II])-1)
        CASE II OF
            0: BEGIN
                Idx_Time = Axistime
                Idx_Data = Dst_Data
                Idx_Name = 'Dst (nT)'
                Idx_Rnge = [MIN(Dst_Data),MAX(Dst_Data)]

```

```

        Idx_dt = 1./24
    END
1: BEGIN
    Idx_Time = AxsTimKp
    Idx_Data = Kp_Data
    Idx_Name = 'Kp index'
    Idx_Rnge = [0,9]
    VertStyl = 1
    Idx_dt = 3./24
    END
2: BEGIN
    Idx_Time = Axistime
    Idx_Data = REFORM(Aur_Data[2,*])
    Idx_Name = 'AE (nT)'
    Idx_Rnge = [MIN(Idx_Data),MAX(Idx_Data)]
    Idx_dt = 1./24
    END
3: BEGIN
    Idx_Time = Axistime
    Idx_Data = REFORM(Aur_Data[0,*])
    Idx_Name = 'AU index (nT)'
    ;Idx_Rnge = [MIN(Idx_Data),MAX(Idx_Data)]
    Idx_Rnge = [0,MAX(Idx_Data)]
    Idx_dt = 1./24
    END
4: BEGIN
    Idx_Time = Axistime
    Idx_Data = REFORM(Aur_Data[1,*])
    Idx_Name = 'AL index (nT)'
    Idx_Rnge = [MIN(Idx_Data),MAX(Idx_Data)]
    Idx_Rnge = [MIN(Idx_Data),10]
    Idx_dt = 1./24
    END
5: BEGIN
    Idx_Time = Axistime
    Idx_Data = REFORM(Aur_Data[3,*])
    Idx_Name = 'AO index (nT)'
    Idx_Rnge = [MIN(Idx_Data),MAX(Idx_Data)]
    Idx_dt = 1./24
    END
ENDCASE

CASE PltType OF
0: BEGIN
;       VctPos = WHERE((Idx Time GE JULDAY(FIX(Txt Month Ini), 14, FIX(Txt Year2Proc), 0),
;       (Idx_Time LT JULDAY(FIX(Txt_Month_Ini), 20, FIX(Txt_Year2Proc), 0, 0)))
;       Idx_Time = Idx_Time[VctPos] & Idx_Data = Idx_Data[VctPos]
    PLOT,Idx_Time,Idx_Data, THICK=Trc_Thick,$
        XTITLE='Time (days)',YTITLE=Idx_Name, $
        XTICKUNITS='Days', XTICKFORMAT='LABEL_DATE', $
        YMINOR=5,XTICKINTERVAL=15,XMINOR=15, CHARSIZE=Txt_Size, $
        XSTYLE=1,XTICKLEN=XTickLen, YTICKLEN=YTickLen, YSTYLE=VertStyl, $
        YRANGE=Idx_Rnge, YTICKINTERVAL=500, CHARTHICK=Txt_Thick
; ORIGINAL -> YMINOR=3,XTICKINTERVAL=15,XMINOR=15, YTICKINTERVAL=3
; IF (VertStyl) THEN OPLOTT,AxsTimKp,FLTARR(N_ELEMENTS(Kp_Data))+4.,LINESTYLE=1
; ONLY USED FOR PAPERS
; XYOUTS, 1000, 1800, Idx_Name, ORIENTATION=90, CHARSIZE=Txt_Size, $
;     CHARTHICK=Txt_Thick, ALIGN=0.5, /DEVICE
    END
1: BEGIN
    Wvlt_Magnetic_Idx, Idx_Time, Idx_Data, Idx_dt, $
    GlobalWS=GlobWS, Pow_Norm=PowNrm, Cone_Inf=ConInf,$
    WavPrd=WavPrd

    WvPrd2 = FIX(ALOG(WavPrd)/ALOG(2))           ; integer powers of 2 in period
    YPlotRng = [MAX(WavPrd),MIN(WavPrd)]       ; sets the x axis plot range
    Y_Tick_V = 2.^(WvPrd2/UNIQ(WvPrd2))        ; unique powers of 2

    Zmin = 0;MIN(PowNrm,/NAN)
    Zmax = MAX(PowNrm,/NAN)

    NBarTick = 4.                               ; tick in the bar
    CBarTick = STRING(Zmin + (FINDGEN(NBarTick+1)/NBarTick)*(Zmax-Zmin), FORMAT='(e8.

    FOR JJ=0, NBarTick DO BEGIN
        A = CBarTick[JJ]
        IF (STRPOS(A, "+000") GE 0) THEN $
            STRPUT, A, " +0", (STRPOS(A, "+000"))
        IF (STRPOS(A, "+00") GE 0) THEN $
            STRPUT, A, " +", (STRPOS(A, "+00"))
        IF (STRPOS(A, "+0") GE 0) THEN $
            STRPUT, A, " +", (STRPOS(A, "+0"))
        IF (STRPOS(A, "-000") GE 0) THEN $
            STRPUT, A, " -0", (STRPOS(A, "-000"))
        IF (STRPOS(A, "-00") GE 0) THEN $

```

```

        STRPUT, A, " -", (STRPOS(A, "-00"))
    IF (STRPOS(A, "-0") GE 0) THEN $
        STRPUT, A, " -", (STRPOS(A, "-0"))
    CBarTick[JJ]=STRCOMPRESS(A,/REMOVE_ALL)
ENDFOR

CONTOUR, PowNrm, Idx_Time, WavPrd, $
    NLEVEL=30,/FILL, $
    YMINOR=1,XTICKINTERVAL=15,XMINOR=15, $
    XTITLE='Time (days)',$,YTITLE='Period (days)', $
    XTICKUNITS='Days', XTICKFORMAT='LABEL_DATE', $
    YTICKS=N_ELEMENTS(Y_Tick_V)-1,YTICKV=Y_Tick_V, $
    YRANGE=YPlotRng,/YTYPE, CHARTHICK=Txt_Thick, $ ;POSITION=PositVct,
    XSTYLE=1, CHARSIZE=Txt_Size, ZRANGE=[Zmin,Zmax], $
    XTICKLEN=XTickLen, YTICKLEN=YTickLen

; ONLY USED FOR PAPERS
cbartick[0]='0.0'
XYOUTS, 1000, 2600, 'Period (days)', ORIENTATION=90, CHARSIZE=Txt_Size, $
    CHARTHICK=Txt_Thick, ALIGN=0.5, /DEVICE

PLOTS, Idx_Time, (Idx_Time*0+2.),LINESTYLE=2, /NOCLIP

COI_XPos = [Idx_Time(0),Idx_Time,MAX(Idx_Time)]
COI_YPos = [MAX(WavPrd),ConInf,MAX(WavPrd)]
POLYFILL,COI_XPos,COI_YPos,ORIEN=+45,SPACING=0.5,NOCLIP=0,THICK=1
POLYFILL,COI_XPos,COI_YPos,ORIEN=-45,SPACING=0.5,NOCLIP=0,THICK=1
PLOTS,Idx_Time,ConInf,NOCLIP=0,THICK=1

;
BarPosit = [PositVct[ActPstn,2]+0.01,PositVct[ActPstn,1],PositVct[ActPstn,2]+0.03]
BarPosit = [0.35, 0.96, 0.825, 0.98]
COLORBAR, DIVISIONS=NBarTick, CHARSIZE=Txt_Size, CHARTHICK=Txt_Thick, $
    TITLE=ClrBrTit,/VERTICAL,/RIGHT,POSITION=BarPosit,TICKNAMES=CBarTick

END
2: BEGIN
    Wvlt_Magnetic_Idx, Idx_Time, Idx_Data, Idx_dt, $
    Pow_Norm=PowNrm, SclAvgTs=SclAvgTs, $
    IniPriod=IniPriod, EndPriod=EndPriod
    PLOT,Idx_Time,SclAvgTs, THICK=ThickTrc,$
    XTITLE='Time (days)',YTITLE=Idx_Name, $
    XTICKUNITS='Days', XTICKFORMAT='LABEL_DATE', $
    XTICKINTERVAL=9, CHARSIZE=Txt_Size, XSTYLE=1,$
    XTICKLEN=XTickLen, YTICKLEN=YTickLen, $
    POSITION=PositVct[ActPstn,*]+[0.1,0,0.1,0]

END
ENDCASE
ENDIF

DEVICE, /CLOSE_FILE
SET_PLOT, 'WIN'
!P.MULTI=0

END

```



```

FUNCTION Auroral_Index_New, Txt_DrvLetter, Txt_Year2Proc, $
    Txt_Month_Ini, Txt_Month_End
;----- ABSTRACT
;   This procedure is a routine that open and read the auroral indices.
;----- CAPTION
;-----
; By:      Henrique C. Aveiro - aveiro@dae.inpe.br
; Date:    July 22, 2008
; Modification :
;-----

; Declares the constants and for the procedure ----- strings variables
;-----
IF (N_ELEMENTS(Txt_DrvLetter) EQ 0) THEN Txt_DrvLetter = 'D:'
IF (N_ELEMENTS(Txt_Year2Proc) EQ 0) THEN Txt_Year2Proc = '2003'
IF (N_ELEMENTS(Txt_Month_Ini) EQ 0) THEN Txt_Month_Ini = '01'
IF (N_ELEMENTS(Txt_Month_End) EQ 0) THEN Txt_Month_End = '02'

; generate the template and open the files -----
VERSION          = 1.00000
DATASTART        = 0 & DATASTART=LONG(DATASTART)
DELIMITER        = 0 & DELIMITER=BYTE(DELIMITER)
MISSINGVALUE     = !VALUES.F_NAN
COMMENTSYMBOL    = ''
FIELDCCOUNT      = 29 & FIELDCCOUNT=LONG(FIELDCCOUNT)
FIELDTYPES       = INTARR(29)
FIELDTYPES[0:2] = 7
FIELDTYPES[3:28] = 3
FIELDNAMES       = STRARR(29)
FIELDNAMES       = ['IDX', 'INF', 'YEAR', 'TAB_BASE', 'H00', 'H01', 'H02', 'H03', $
    'H04', 'H05', 'H06', 'H07', 'H08', 'H09', 'H10', 'H11', 'H12', 'H13', $
    'H14', 'H15', 'H16', 'H17', 'H18', 'H19', 'H20', 'H21', 'H22', 'H23', 'DAILY_MEAN']
FIELDLOCATIONS  = [0, 2, 10, 16, 20+FINDBGEN(25)*4]
FIELDLOCATIONS  = LONG(FIELDLOCATIONS)
FIELDGROUPS     = INDGEN(29)

MyTemplate={VERSION:VERSION,DATASTART:DATASTART,DELIMITER:DELIMITER, $
    MISSINGVALUE:MISSINGVALUE,COMMENTSYMBOL:COMMENTSYMBOL,$
    FIELDCCOUNT:FIELDCCOUNT,FIELDTYPES:FIELDTYPES,FIELDNAMES:FIELDNAMES,$
    FIELDLOCATIONS:FIELDLOCATIONS,FIELDGROUPS:FIELDGROUPS}

Reader = READ_ASCII(Txt_DrvLetter+'\Dados Geofísicos\Magnetic Indices\AE\AE'+Txt_Year2Proc+'.txt', $
    TEMPLATE=MyTemplate) ; load the data from the file Dir_Main

ArrSize = N_ELEMENTS(Reader.H00)
AU_Count = 0
AL_Count = 0
AE_Count = 0
AO_Count = 0

FOR II=0L, ArrSize-1, 1 DO BEGIN

    Data_Tmp = [Reader.H00[II], Reader.H01[II], Reader.H02[II], $
        Reader.H03[II], Reader.H04[II], Reader.H05[II], $
        Reader.H06[II], Reader.H07[II], Reader.H08[II], $
        Reader.H09[II], Reader.H10[II], Reader.H11[II], $
        Reader.H12[II], Reader.H13[II], Reader.H14[II], $
        Reader.H15[II], Reader.H16[II], Reader.H17[II], $
        Reader.H18[II], Reader.H19[II], Reader.H20[II], $
        Reader.H21[II], Reader.H22[II], Reader.H23[II]]

    Data_Tmp = Data_Tmp
    Idx2Chng = WHERE(Data_Tmp EQ 9999) ; eliminates missing data
    IF (Idx2Chng[0] NE -1) THEN Data_Tmp[Idx2Chng] = !VALUES.F_NAN

    CASE (STRUPCASE(Reader.IDX[II])) OF
        'AU': BEGIN
            AU_Tmp = Reader.TAB_BASE[II]*100+Data_Tmp
            AU_Data = (AU_Count EQ 0) ? AU_Tmp : [AU_Data, AU_Tmp]
            AU_Count++
        END
        'AL': BEGIN
            AL_Tmp = Reader.TAB_BASE[II]*100+Data_Tmp
            AL_Data = (AL_Count EQ 0) ? AL_Tmp : [AL_Data, AL_Tmp]
            AL_Count++
        END
        'AE': BEGIN
            AE_Tmp = Reader.TAB_BASE[II]*100+Data_Tmp
            AE_Data = (AE_Count EQ 0) ? AE_Tmp : [AE_Data, AE_Tmp]
            AE_Count++
        END
        'AO': BEGIN
            AO_Tmp = Reader.TAB_BASE[II]*100+Data_Tmp
            AO_Data = (AO_Count EQ 0) ? AO_Tmp : [AO_Data, AO_Tmp]
            AO_Count++
    END
END

```

```

                END
            ELSE: BEGIN PRINT, 'ERROR -> Auroral_Index.NEW.pro' & STOP & END
        ENDCASE
    ENDFOR

    DayIni = JULIAN_DAY(FIX(Txt_Year2Proc), FIX(Txt_Month_Ini), 1)
    DayEnd = JULIAN_DAY(FIX(Txt_Year2Proc), FIX(Txt_Month_End)+1, 1)-1
    Aur_Data = INTARR(4, 24*(DayEnd-DayIni+1))
    Aur_Data[0,*] = AU_Data[(DayIni-1)*24:DayEnd*24-1]
    Aur_Data[1,*] = AL_Data[(DayIni-1)*24:DayEnd*24-1]
    Aur_Data[2,*] = AE_Data[(DayIni-1)*24:DayEnd*24-1]
    Aur_Data[3,*] = AO_Data[(DayIni-1)*24:DayEnd*24-1]

    RETURN, Aur_Data ;0-AU,1-AL,2-AE,3-AO
    END

```

```

FUNCTION Dst_Index_New, Txt_DrvLetter, Txt_Year2Proc, $
          Txt_Month_Ini, Txt_Month_End
;----- ABSTRACT
; This procedure is a routine that open and read the Dst index.
;----- CAPTION
;-----
; By:          Henrique C. Aveiro - aveiro@dae.inpe.br
; Date:        July 22, 2008
; Modification :
;-----

; Declares the constants and for the procedure -----
;----- strings variables
IF (N_ELEMENTS(Txt_DrvLetter) EQ 0) THEN Txt_DrvLetter = 'D:'
IF (N_ELEMENTS(Txt_Year2Proc) EQ 0) THEN Txt_Year2Proc = '2003'
IF (N_ELEMENTS(Txt_Month_Ini) EQ 0) THEN Txt_Month_Ini = '01'
IF (N_ELEMENTS(Txt_Month_End) EQ 0) THEN Txt_Month_End = '02'

; generate the template and open the files -----
VERSION          = 1.00000
DATASTART        = 0 & DATASTART=LONG(DATASTART)
DELIMITER        = 0 & DELIMITER=BYTE(DELIMITER)
MISSINGVALUE     = 'VALUES.F_NAN'
COMMENTSYMBOL   = ''
FIELDCCOUNT      = 28 & FIELDCCOUNT=LONG(FIELDCCOUNT)
FIELDTYPES       = INTARR(28)
FIELDTYPES[0:1]=7
FIELDTYPES[2:27]=3
FIELDNAMES       = STRARR(28)
FIELDNAMES       = ['IDX', 'YEAR', 'TAB_BASE', 'H00', 'H01', 'H02', 'H03', $
                   'H04', 'H05', 'H06', 'H07', 'H08', 'H09', 'H10', 'H11', 'H12', 'H13', $
                   'H14', 'H15', 'H16', 'H17', 'H18', 'H19', 'H20', 'H21', 'H22', 'H23', 'DAILY_MEAN']
FIELDLOCATIONS  = [0,10,16,20+INDGEN(25)*4]
FIELDLOCATIONS=LONG(FIELDLOCATIONS)
FIELDGROUPS     = INDGEN(28)

MyTemplate={VERSION:VERSION,DATASTART:DATASTART,DELIMITER:DELIMITER, $
            MISSINGVALUE:MISSINGVALUE,COMMENTSYMBOL:COMMENTSYMBOL,$
            FIELDCCOUNT:FIELDCCOUNT,FIELDTYPES:FIELDTYPES,FIELDNAMES:FIELDNAMES,$
            FIELDLOCATIONS:FIELDLOCATIONS,FIELDGROUPS:FIELDGROUPS}

Reader = READ_ASCII(Txt_DrvLetter+'\Dados Geofísicos\Magnetic Indices\Dst\Dst'+Txt_Year2Proc+'.txt', $
                   TEMPLATE=MyTemplate) ; load the data from the file Dir_Main

DayIni = JULIAN_DAY(FIX(Txt_Year2Proc), FIX(Txt_Month_Ini), 1)
DayEnd = JULIAN_DAY(FIX(Txt_Year2Proc), FIX(Txt_Month_End)+1, 1)-1
Dst_Data = INTARR(24*(DayEnd-DayIni+1))

FOR II=DayIni, DayEnd, 1 DO BEGIN
  Dst_Data[(II-DayIni)*24:(II-DayIni)*24+23] = Reader.TAB_BASE[II-1]*100+$
    [Reader.H00[II-1], Reader.H01[II-1], Reader.H02[II-1], $
    Reader.H03[II-1], Reader.H04[II-1], Reader.H05[II-1], $
    Reader.H06[II-1], Reader.H07[II-1], Reader.H08[II-1], $
    Reader.H09[II-1], Reader.H10[II-1], Reader.H11[II-1], $
    Reader.H12[II-1], Reader.H13[II-1], Reader.H14[II-1], $
    Reader.H15[II-1], Reader.H16[II-1], Reader.H17[II-1], $
    Reader.H18[II-1], Reader.H19[II-1], Reader.H20[II-1], $
    Reader.H21[II-1], Reader.H22[II-1], Reader.H23[II-1]]
ENDFOR

RETURN, Dst_Data
END

```

```

FUNCTION Kp_Index_New, Txt_DrvLetter, Txt_Year2Proc, $
          Txt_Month_Ini, Txt_Month_End
;----- ABSTRACT
; This procedure is a routine that open and read the Kp index.
;----- CAPTION
;
;-----
; By:          Henrique C. Aveiro - aveiro@dae.inpe.br
; Date:        July 22, 2008
; Modification :
;-----

; Declares the constants and for the procedure -----
;----- strings variables
IF (N_ELEMENTS(Txt_DrvLetter) EQ 0) THEN Txt_DrvLetter = 'D:'
IF (N_ELEMENTS(Txt_Year2Proc) EQ 0) THEN Txt_Year2Proc = '2003'
IF (N_ELEMENTS(Txt_Month_Ini) EQ 0) THEN Txt_Month_Ini = '01'
IF (N_ELEMENTS(Txt_Month_End) EQ 0) THEN Txt_Month_End = '02'

; generate the template and open the files -----
VERSION          = 1.00000
DATASTART        = 0 & DATASTART=LONG(DATASTART)
DELIMITER        = 0 & DELIMITER=BYTE(DELIMITER)
MISSINGVALUE     = !VALUES.F_NAN
COMMENTSYMBOL    = ''
FIELDLCOUNT      = 26 & FIELDLCOUNT=LONG(FIELDLCOUNT)
FIELDTYPES       = INTARR(26)
FIELDTYPES[0:25] = 3
FIELDTYPES[ 21 ] = 4
FIELDTYPES[ 24 ] = 4
FIELDNAMES       = STRARR(26)
FOR I=0,25 DO BEGIN
  IF (I LT 9) THEN BEGIN FIELDNAMES[I] = 'field0'+STRING(I+1,FORMAT='(I1)')
  ENDIF ELSE FIELDNAMES[I] = 'field'+ STRING(I+1,FORMAT='(I2)')
ENDFOR
FIELDLOCATIONS  = [0,6,10,12,14,16,18,20,22,24,26,28,31,34,37,40,43,46,49,52,55,58,61,62,65,70]
FIELDLOCATIONS=LONG(FIELDLOCATIONS)
FIELDGROUPS     = INDGEN(26)

MYTEMPLATE={VERSION:VERSION,DATASTART:DATASTART,DELIMITER:DELIMITER,MISSINGVALUE:MISSINGVALUE,COMMENT:
Reader = READ_ASCII(Txt_DrvLetter+'\Dados Geofísicos\Magnetic Indices\kp\kp'+Txt_Year2Proc+'.txt', $
  TEMPLATE=MyTemplate) ; load the data from the file Dir_Main

DayIni = JULIAN_DAY(FIX(Txt_Year2Proc), FIX(Txt_Month_Ini), 1)
DayEnd = JULIAN_DAY(FIX(Txt_Year2Proc), FIX(Txt_Month_End)+1, 1)-1
Kp_Data = FLTARR(8*(DayEnd-DayIni+1))

FOR II=DayIni, DayEnd, 1 DO $
  Kp_Data[(II-DayIni)*8:(II-DayIni)*8+7] = 0.1*[Reader.Field04[II-1], $
    Reader.Field05[II-1], Reader.Field06[II-1], Reader.Field07[II-1], $
    Reader.Field08[II-1], Reader.Field09[II-1], Reader.Field10[II-1], $
    Reader.Field11[II-1]]

RETURN, Kp_Data
END

```

```

PRO WVLMT_MAGNETIC_IDX, Axistime, TimSerie, Delta_dt, $
  GlobalWS=GlobalWS, Pow_Norm=Pow_Norm, Cone_Inf=Cone_Inf, $
  WavPriod=WavPriod, IniPriod=IniPriod, EndPriod=EndPriod, $
  SclAvgTS=SclAvgTS
;----- ABSTRACT
;   This function calculates the scalogram using the Morlet
; wavelet-mother to identify periodicities in the magnetic indices.
;----- CAPTION
;
;-----
; By:           Henrique C. Aveiro - aveiro@dae.inpe.br
; Date:         July 28, 2008
; Modification :
;-----

; Declares the constants and for the procedure -----
NRawFile = N_ELEMENTS(TimSerie)
Scale_s0 = 0.500000/2      ;=2 * Delta_dt(general)      ; the initial scale (=s0)
Delta_dj = 0.125000      ; this will do 8 sub-octaves per octave (=dj)
J_Powers = 4./Delta_dj   ; this says do 4 powers-of-two with dj sub-octaves each (jl)
WavMothr = 'Morlet'      ; choose Morlet as wavelet-mother

; Normalize by standard deviation, save an extra copy of the -----
; original series and determine if the data quality is good -----
NorSerie = (TimSerie - TOTAL(TimSerie,/NAN)/NRawFile)
ReconSer = NorSerie

; Wavelet transform -----
WaveAnal = WAVELET(ReconSer,Delta_dt,PERIOD=WavPriod,SCALE=WavScale,S0=Scale_s0, $
  PAD=1,COI=Cone_Inf,DJ=Delta_dj,J=J_Powers,MOTHER=WavMothr)

WaveSpec = (ABS(WaveAnal))^2      ; compute wavelet power spectrum
J_Scales = N_ELEMENTS(WavScale) - 1
ScaleAvg = REBIN(TRANPOSE(WavScale),NRawFile,J_Scales+1) ; expand scale-->(J+1)x(NRawFile) array
Pow_Norm = WaveSpec/ScaleAvg
C_delta = 0.776                  ; reconstruction factor
GlobalWS = TOTAL(Pow_Norm,1)/NRawFile ; global wavelet spectrum (GWS)

; Scale-average between periods of IniPriod-EndPriod days -----
IF (N_ELEMENTS(IniPriod) NE 0) THEN BEGIN
  ScaleAvg = WHERE((WavPriod GE IniPriod) AND (WavPriod LT EndPriod))
  SclAvgTS = Delta_dj*Delta_dt/C_delta*TOTAL(Pow_Norm(*,ScaleAvg),2) ; [Eqn(24)]
ENDIF
END
END

```


PUBLICAÇÕES TÉCNICO-CIENTÍFICAS EDITADAS PELO INPE

Teses e Dissertações (TDI)

Teses e Dissertações apresentadas nos Cursos de Pós-Graduação do INPE.

Manuais Técnicos (MAN)

São publicações de caráter técnico que incluem normas, procedimentos, instruções e orientações.

Notas Técnico-Científicas (NTC)

Incluem resultados preliminares de pesquisa, descrição de equipamentos, descrição e ou documentação de programas de computador, descrição de sistemas e experimentos, apresentação de testes, dados, atlas, e documentação de projetos de engenharia.

Relatórios de Pesquisa (RPQ)

Reportam resultados ou progressos de pesquisas tanto de natureza técnica quanto científica, cujo nível seja compatível com o de uma publicação em periódico nacional ou internacional.

Propostas e Relatórios de Projetos (PRP)

São propostas de projetos técnico-científicos e relatórios de acompanhamento de projetos, atividades e convênios.

Publicações Didáticas (PUD)

Incluem apostilas, notas de aula e manuais didáticos.

Publicações Seriadas

São os seriados técnico-científicos: boletins, periódicos, anuários e anais de eventos (simpósios e congressos). Constam destas publicações o Internacional Standard Serial Number (ISSN), que é um código único e definitivo para identificação de títulos de seriados.

Programas de Computador (PDC)

São a seqüência de instruções ou códigos, expressos em uma linguagem de programação compilada ou interpretada, a ser executada por um computador para alcançar um determinado objetivo. Aceitam-se tanto programas fonte quanto os executáveis.

Pré-publicações (PRE)

Todos os artigos publicados em periódicos, anais e como capítulos de livros.